이학박사 학위논문

Numerical study on evolution of the Yellow Sea Warm Current and its contribution to nitrate flux

겨울철 황해 난류 형성 및 난류를 통한 황해 내 질산염 유입에 관한 수치 실험 연구

2020 년 2 월

서울대학교 대학원

지구환경과학부

탁 용 진

Abstract

The Yellow Sea (YS) is a shallow, semi-enclosed marginal sea surrounded by China and the Korean Peninsula. A deep trough is located in the central YS. The northwesterly wind drives the Yellow Sea Warm Current (YSWC) flows into the YS along the deep trough and two southward coastal currents occurs along the Chinese and Korean coasts in winter.

Previous observations have shown that the path of the YSWC has shifted to the west from the deep trough one or two days after northerly wind bursts. However, exact evolution process of the YSWC remains unclear. Model results in this study suggested that the YSWC occurs along the deep trough one day after the wind burst. It shifts to the west of the trough two days later, which phenomenon is generally referred to as the westward shift of the YSWC.

Previous studies have proposed a possibility that the westward shift can be driven by continental shelf waves (CSWs). Idealized models were performed to figure out the relationship between CSWs and the westward shift, and generation mechanism of the CSWs driving the shift. The westward shift appeared from the north to south with the propagation of sea surface height at a speed of 3

m/s that was consistent with the phase speed of the first mode CSW. CSWs driving the westward shift were generated on the northern slope primarily by scattering of barotropic Kelvin waves that developed due to northerly wind and propagated poleward into the YS along the eastern boundary off Korea.

The YSWC plays an important role in the ecosystem of the YS, because it provides an external water mass in winter. A physical–biogeochemical coupled model and several sensitivity experiments were performed to reveal the role of the YSWC in nitrate (NO3) budget of the YS and quantify contributions of external sources and biological process to NO3 in the YS. Multiple sensitivity experiments revealed quantitative contribution of NO3 from the Changjiang River, Kuroshio Current (KC), run–off in the YS, and Taiwan Warm Current (TWC). 51 percent of total NO3 in the YS was estimated from the Changjiang River and 25 percent from the KC and rivers in the YS, respectively. The TWC contributed 8 percent. Change by nitrification process due to the biological activity was estimated less than 1 percent of the total NO3 in the YS. The estimation of NO3 flux into the YS suggested that 20 percent of total mass NO3 in the YS was supplied by the YSWC during winter. Relative NO3 contributions of the Changjiang River, KC, and TWC through the YSWC to the total inflow to the YS were

64, 29, and 10 percent, respectively.

Keyword : Yellow Sea Warm Current, Westward shift, Continental Shelf Waves, Nitrate flux, ROMS
Student Number : 2012-23084

Table of Contents

List of Figures

List of Tables

1. General Introduction

The Yellow Sea (YS) between China and the Korean Peninsula is a shallow, semi-enclosed marginal sea (Figure 1.1). A deep trough with a maximum depth of more than 80 m is located in the central area of the YS. In winter, the Yellow Sea Warm Current (YSWC) with a warm and salty water mass flows into the YS along the west flank of the trough (Lin et al., 2011; Lin and Yang, 2011; Lü et al., 2015). It has been widely recognized that the YSWC is an upwind flow driven by the northwesterly wind in winter (Park, 1986; Hsueh, 1987; Lin and Yang, 2011). The wind fields in the YS show strong seasonality owing to the East Asian monsoon. The northwesterly wind is dominant in winter (Figure 1.2).

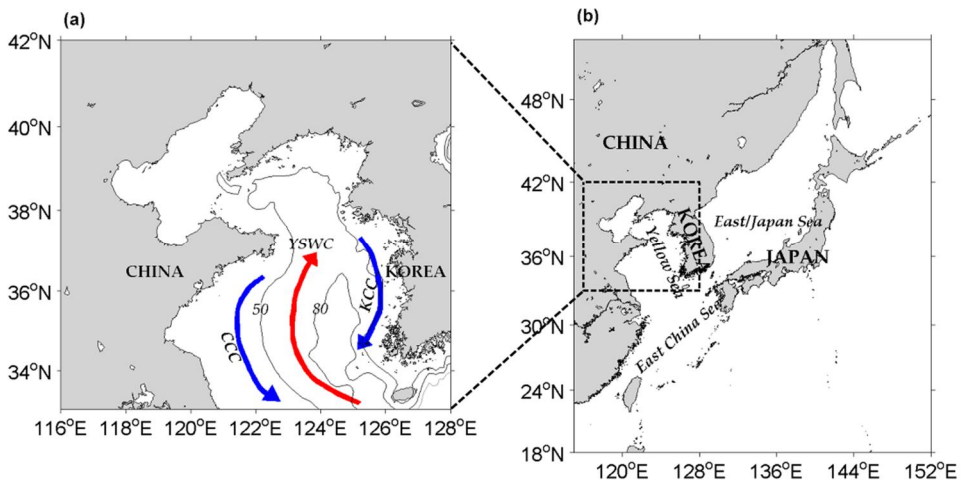

Figure 1. 1 (a) Schematic diagram of Yellow Sea circulation during winter. (b) The model domain. YSWC, CCC and KCC stand for the Yellow Sea Warm Current, Chinese Coastal Current and Korean

Coastal Current, respectively. The contour lines in (a) indicate isobaths with a unit of meters.

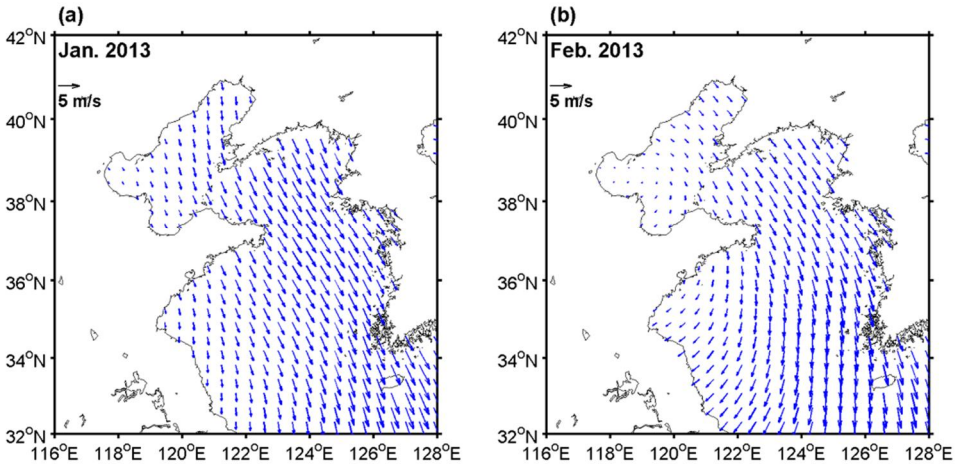

Figure 1. 2 The monthly mean surface wind vectors in (a) January and (b) February of 2013, obtained from the European Centre for Medium-Range Weather Forecasts (ECMWF).

The existence of the YSWC was first proposed by Uda (1934); since then, it has been considered as a continuous flow that supplies heat and salt along the trough to the YS. However, early studies using observations failed to show concrete evidence for the existence of a permanent northward flow along the trough. Instead, the possibility of episodic flows in response to strong northwesterly winds was raised (Hsueh, 1987; Beardsley et al., 1992; Teague and Jacobs, 2000; Lie et al., 2001). However, recent studies have suggested that the YSWC persists to the west of the trough throughout winter (Moon et al., 2009; Lin et al., 2011). The controversy over the persistence of the YSWC might result from

differences in observation locations. For example, observation data reported by Lin et al. (2011) was obtained in the western slope of the trough, whereas other data were obtained along the trough of the YS.

The generation mechanism for wind-driven flows including the YSWC has been widely studied (Park, 1986; Hsueh and Pang, 1989; Hsueh and Yuan, 1997; Isobe, 2008; Lin and Yang, 2011). During winter, the northwesterly wind drags water from north to south in the upper part of the YS so that downwind flows occur along the Korean and Chinese coasts. These flows, known as the Korean Coastal Current (KCC) and Chinese Coastal Current (CCC), respectively (Figure 1.1a), cause a pressure gradient to the north that generates an upwind flow called the YSWC in the central deep region (Park, 1986; Lin and Yang, 2011).

The path of the YSWC has widely been investigated through the observation, satellite, and model. In a general double slope region like the YS, the upwind flow appears along a deep trough because the frictional response to surface wind stress is strong at the shallow regime near the coastal boundaries and relatively weak in the deep trough. However, the path of the YSWC is shifted to the west flank of the deep trough. Several potential causes of the westward shift of the YSWC have been examined by many

scientists. Xie et al. (2002) suggested that surface Ekman transport driven by northerly wind might play an important role in this shift. However, The Ekman transport cannot be a main driver of the westward shift because it does not affect the entire water column (Lin et al., 2011). The zonal front located at the entrance of the YS during winter has also proposed to be relevant to the westward shift of the YSWC (Wang et al., 2012). Huang et al. (2005) argued that baroclinic currents driven by surface cooling act to induce the shift. However, barotropic models assuming homogeneous temperature and salinity exhibited the westward shift, suggesting that continental shelf waves (CSWs) may induce the shift in response to north–westerly winds (Takahashi et al., 1995; Lin and Yang, 2011; Qu et al., 2018). Nevertheless, the generation of CSWs and the spatiotemporal evolution of the westward shift in relation to CSWs remain poorly understood.

The YSWC plays an important role in the ecosystem and spring bloom as providing an external water mass in the YS (Hyun and Kim, 2003; Xuan et al., 2011; Jin et al., 2013; Zhou et al., 2013; Liu et al., 2015a; Liu et al., 2015b). Previous studies showed the physical and biogeochemical effects of the YSWC on the spring bloom in the YS. Hyun and Kim (2003) implied that the YSWC might provide a proper environment to develop the primary production as

forming the thermohaline front in the YS. Xuan et al. (2011) presented that the YSWC would develop the spring bloom in the central YS by increasing the water temperature. Zhou et al. (2013) suggested the wind speed has significantly correlated with the spring bloom as developing the YSWC carrying nutrients or supplying accumulated nutrients in a bottom layer. Observations showed the YSWC provided relatively high nutrients water for the YS and had an influence on the phytoplankton community in the YS (Jin et al., 2013; Liu et al., 2015a). However, the relative contribution of the nutrients from the sources to the YS and the role of the YSWC which delivers nutrients have not been revealed yet.

2. Evolution of wind-driven flows in the Yellow Sea during winter[①]

2.1. Introduction

There are several studies about mechanism for the generation of the wind-driven flows including the YSWC in winter. However, the temporal evolution of the flows has not been investigated in the YS. Although some observations in the YS show significant upwind flows with one- or two-day lags to the northerly wind (Hsueh, 1988; Teague and Jacobs, 2000; Lin et al., 2011), it is not easy to quantify the relationship between the northwesterly wind and the responding flows owing to limited observations in time and space. Numerical experiments might be useful to understand the connection between the wind and the flows (Takahashi et al., 1995; Lin and Yang, 2011).

Takahashi et al. (1995) suggested that the clockwise circulation in the YS is balanced with the wind at a two-day lag based on a simple barotropic model experiment. However, their model was too simplified to simulate realistic flow in the YS including the CCC and the realistic path of the YSWC. Moreover, the model did not

[①] The results of the presented work have been published in Tak et al. (2016).

consider the tidal forcing, which can significantly alter the subtidal flow in the YS (Lie et al., 2001; Moon et al., 2009; Kim et al., 2013a). In the present study, a realistic three-dimensional numerical model forced by realistic atmospheric and tidal conditions was used to simulate the wind-driven flows and their evolution in winter. The evolution of the wind-driven flows is crucial not only in the formation of the YSWC but also the variability of the path.

2.2. Model configuration

The numerical model used for the study is the Regional Ocean Modeling System (ROMS), which is a free-surface ocean model with terrain-following vertical coordinates and curvilinear horizontal coordinates. ROMS is used to solve hydrostatic, incompressible, primitive equations. The model domain covers the Northwest Pacific (115-152° E, 18-52° N), which includes the YS, the East China Sea, and the East/Japan Sea (Figure 1.1b). The horizontal grid resolution is about 1/10° , and the model has 40 vertical layers. The horizontal advection scheme uses third-order upstream advection. The K-Profile Parameterization scheme (Large et al., 1994) is used for vertical mixing, and the Smagorinsky diffusivity and viscosity schemes are employed for

horizontal mixing.

For the lateral open boundary, the monthly mean temperature, salinity, and velocity averaged from the Simple Ocean Data Assimilation (SODA) for the period of 2001–2010 were used. The surface forcing data include 2013 values of daily mean wind, solar radiation, air temperature, sea level pressure, precipitation, and relative humidity from the ERA-Interim reanalysis data of the European Centre for Medium-Range Weather Forecasts (Dee et al., 2011). On the basis of these data, the surface heat flux was calculated by using bulk formulae (Fairall et al., 1996). Tidal forcing of 10 tidal components provided by TPXO6 was applied along the open boundaries (Egbert and Erofeeva, 2002). The topography data of the model was obtained from the Earth Topography five-minute grid (ETOPO5) dataset of the National Geophysical Data Center and was interpolated into model grid points. The buoyancy forcing by freshwater discharge from 12 rivers in the Bohai Sea and the YS was also used in the model. The monthly mean discharge from the Changjiang River was obtained by averaging the observed discharge from 2001 to 2010. The discharge data for other rivers were obtained from the Global River Discharge Database (Vörösmarty et al., 1996) and Wang et al. (2008).

The initial temperature and salinity for an experiment were

obtained from the National Ocean Data Center (NODC) World Ocean Atlas 1998 (WOA98) (Antonov et al., 1998; Boyer et al., 1998). The initial velocity field was calculated from the geostrophic equation. A three-year spin-up was performed to adjust the model state for a hindcast simulation. The model results for January to February 2013 were analyzed.

2.3. Model validation

To evaluate the model, the monthly mean simulated sea surface temperature (SST) was compared with monthly mean satellite SST observed in January and February 2013 (Figure 2.1) by the National Oceanic and Atmospheric Administration/Advanced Very High Resolution Radiometer (NOAA/AVHRR) Pathfinder distributed by the Jet Propulsion Laboratory of the National Aeronautics and Space Administration (NASA).

The maxima and minima of the simulated SST and the path of the YSWC were comparable to those of the observation in both months. However, the simulated SST was higher (lower) than the observation in the central area (coastal regions) of the YS. This difference may be attributed to model errors and an uncertainty from atmospheric forcing used in this study. Satellite SST with a

warm bias of about 1℃ in the central area and a cold bias of about 2–3℃ in the coastal area in the YS (Kwak et al., 2015) could have also caused these differences.

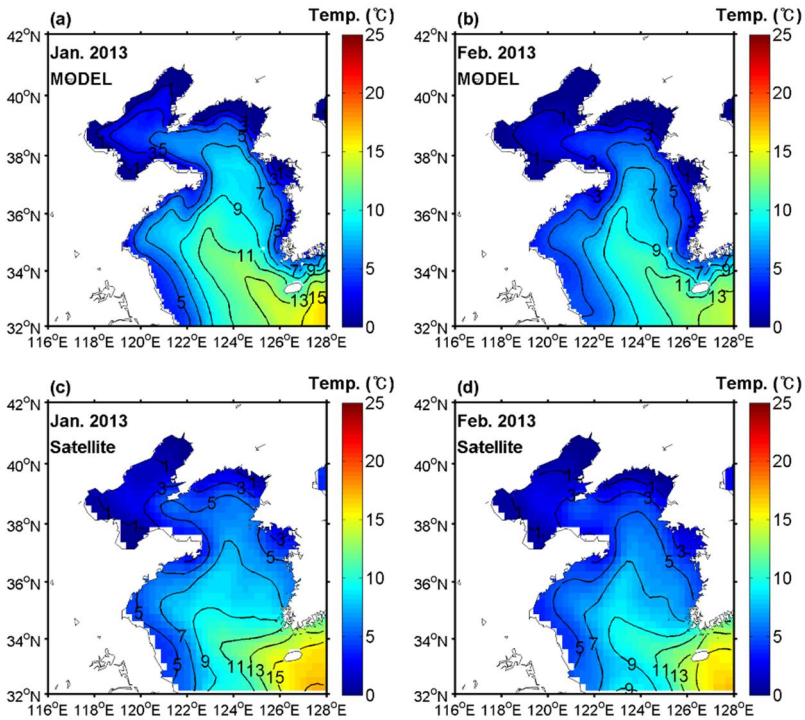

Figure 2. 1 Comparison of sea surface temperature between (upper) the model and (lower) the satellite observation in (left) January and (right) February of 2013.

Vertical sections of daily mean simulated temperature and salinity were compared with in-situ data observed along 124.4° E by National Institute of Fisheries Sciences, Korea on February 28, 2013 (Figure 2.2). Both simulated temperature and salinity were higher by 1° C and 1 than observed. Uncertainty of atmospheric forcing and river discharge may cause this difference. However, the

spatial gradients of simulated temperature and salinity are comparable with that of the observed data.

The differences in simulated and observed temperature and salinity may not be critical for this study because the focus is the evolution of the flows driven by wind. Despite the differences in temperature, the path of the YSWC, which was characterized by relatively warm and saline water in the model, matched well with the observation.

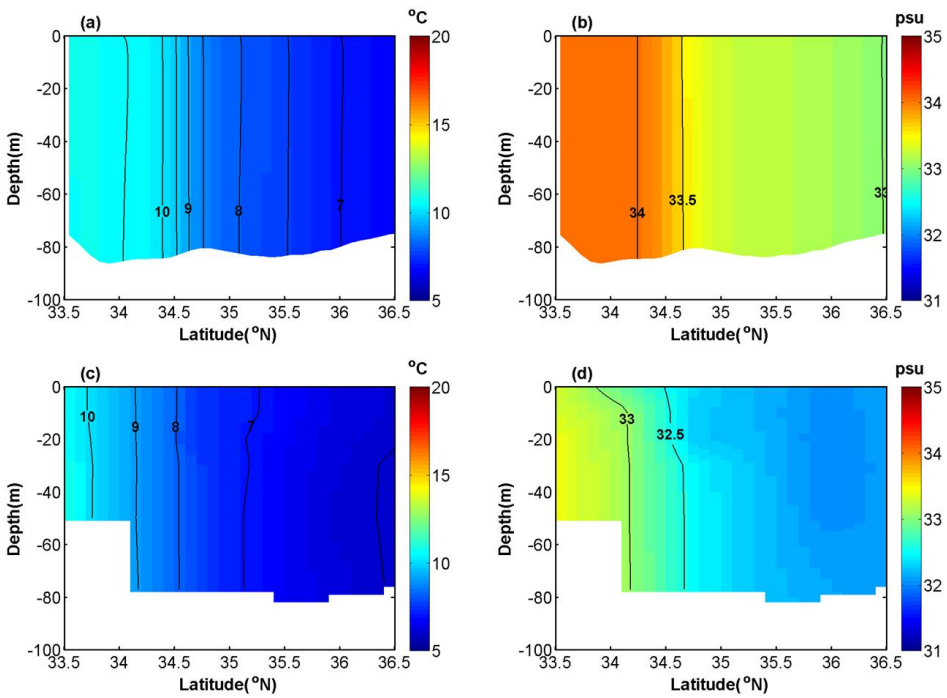

Figure 2. 2 Comparison of vertical sections of (a and c) temperature and (b and d) salinity along 124.4° E by National Institute of Fisheries Sciences, Korea on February 28, 2013. The upper (a and b) and lower (c and d) panels show the model and the in-situ observation, respectively.

2.4. Model results

2.4.1 Mean flow in winter

The monthly mean horizontal velocities in the surface and the subsurface layers effectively represented the surface and the subsurface layer flows in January 2013 (Figure 2.3). In this study, the surface layer is defined as the top layer, and the subsurface layer is defined as a layer between a depth of 30 m and the bottom. Southward coastal currents driven by the northwesterly wind were prominent features in the surface layer, and the southward flow along the Korean coast was stronger than the flow along the Chinese coast. The prominent KCC may crucially contribute to the sediment transport along the Korean coast (Lee, 2014). The northward YSWC to the west of the trough and the southward flow along the Korean coast were well identified in the subsurface layer. This flow pattern is consistent with those reported in previous model studies (Moon et al., 2009; Xu et al., 2009; Kim et al., 2013a).

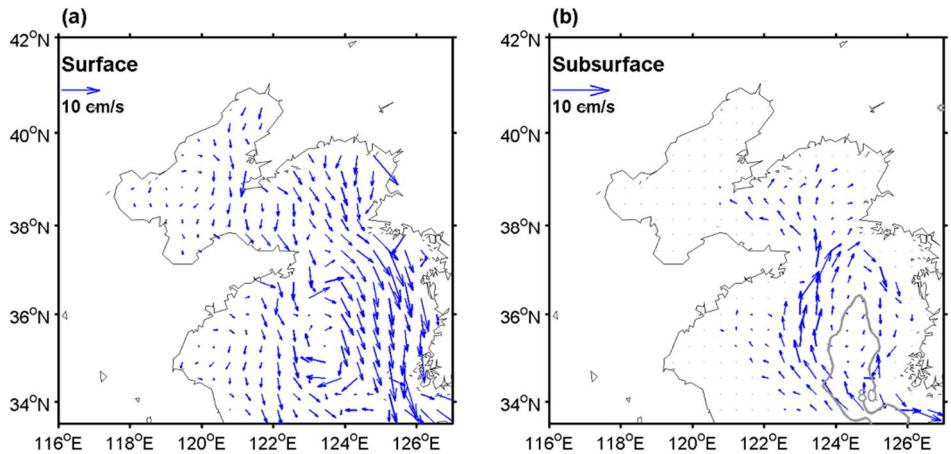

Figure 2. 3 Monthly mean horizontal distributions of (a) surface flow and (b) subsurface flow (averaged below a depth of 30 m) in January 2013.

Vertical sections of the monthly mean meridional flow along 34° N, 35° N, and 36° N in January 2013 are shown in Figure 2.4. The pronounced southward current along the Korean coast and the northward YSWC to the west of the trough were common features in all sections. On the other hand, the CCC along the Chinese coast was less pronounced and its speed was relatively weak. The maximum mean velocity of the YSWC, about 6 cm/s, observed in the 35° N section is close to the velocity observed by Lin et al. (2011). Teague and Jacobs, (2000) reported monthly mean northward velocities of −3.1, −1.8, and 0.3 cm/s at depths of 14 m, 44 m, and 72 m, respectively, which was observed within the central YS in January 1996. These observed velocities are comparable to the model velocities of −2.3, 0.2, and 2.2 cm/s at the corresponding

depths of the same location (35.967° N, 124.033° E). The small deviations between the simulated and observed velocities may be in part attributed to large inter-annual variations of circulation.

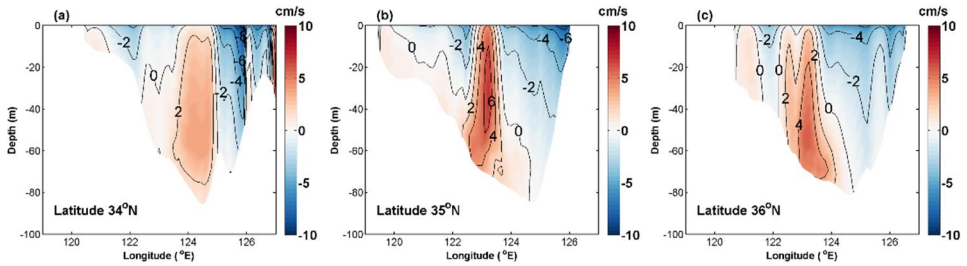

Figure 2. 4 The vertical sections of monthly mean meridional velocity across (a) 34° N, (b) 35° N, and (c) 36° N in January 2013. Positive values represent northward flow.

2.4.2 Temporal variation of the YSWC

Sparse observations of ocean currents have been made across the YS trough where the main path of the YSWC is expected (Lin et al. 2011). For this reason, less has been known regarding the spatial and temporal variabilities of the YSWC. To help elucidate the spatial and temporal variabilities of the YS ocean circulation, I examined Hovmöller diagrams of daily mean meridional velocity averaged from 30 m to the bottom along sections 34° N, 35° N, and 36° N, which cover 60 days starting from January 1, 2013 (Figure 2.5). The location of the maximum velocity changed with latitude. The maximum northward velocity generally appeared at the deep

trough in the 34° N section, but it appeared on the western slope of the trough in the 35° N and 36° N sections (Figures 2.4 and 2.5). The northward flow strengthened with an increase in latitude. The northward flow at 34° N was intermittent rather than steady, as suggested by Lie et al. (2001). In contrast, this flow was more persistent in the 35° N and 36° N sections, which is consistent with a recent observation study (Lin et al., 2011).

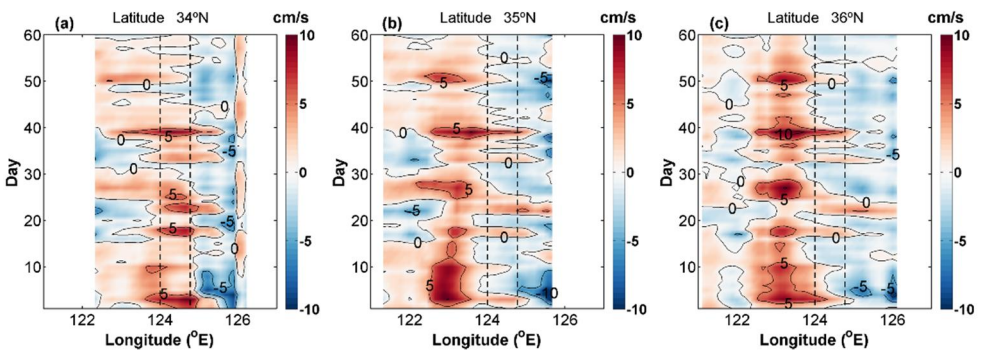

Figure 2. 5 Hovmöller diagrams of daily mean meridional velocity, vertically averaged from 30 m depth to the bottom along (a) 34° N, (b) 35° N, and (c) 36° N. The y-axis indicates days since January 1, 2013. Two dashed lines indicate the trough deeper than 80 m depth. Positive values represent northward flow.

The northward flows showed large temporal fluctuations (Figure 2.5). Previous studies have suggested that the YSWC is driven mainly by northwesterly wind (Park, 1986; Hsueh, 1987; Lin and Yang, 2011). The daily mean wind averaged spatially from 116° E to 128° E and from 33° N to 42° N showed large temporal variations (Figure 2.6). Spectral analysis of the daily mean wind

and northward flows in the subsurface layer indicated dominant variabilities at most periods (Figure 2.7). The spectral peaks of the northward flows in all sections were located at frequencies similar to those of the wind. However, a quantitative difference was noted in the frequencies of the maximum peaks of the northward flows among the sections. The maximum peak of the northward flow in the 34° N section occurred at 0.049 cpd (~1 cycle per 20 days), whereas the peaks in the 35° N and 36° N sections occurred at 0.083 cpd (~1 cycle per 12 days). Nevertheless, the highest spectral peak of the daily mean wind at the 12-day period corresponds well to those of the northward subsurface flow in the zonal sections at 35° N and 36° N. This suggests that the variability of the northward flow in the interior of the YS (35° N and 36° N) is controlled mainly by the wind with a shorter period of 12 days, although the variability of the subsurface northward flow near the entrance of the YS (34° N) is affected not only by the longer, 20-day period of wind variability but also by other forcing in the adjacent East China Sea (Lie et al., 2013).

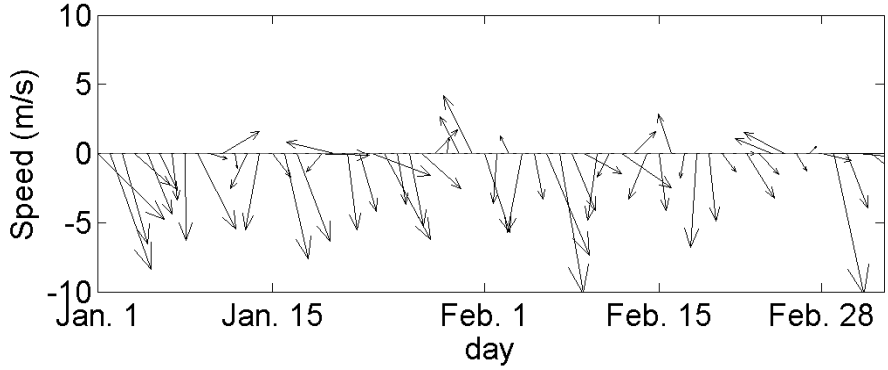

Figure 2. 6 Daily mean surface wind vector averaged over the Yellow Sea, starting from January 1 to March 5, 2013.

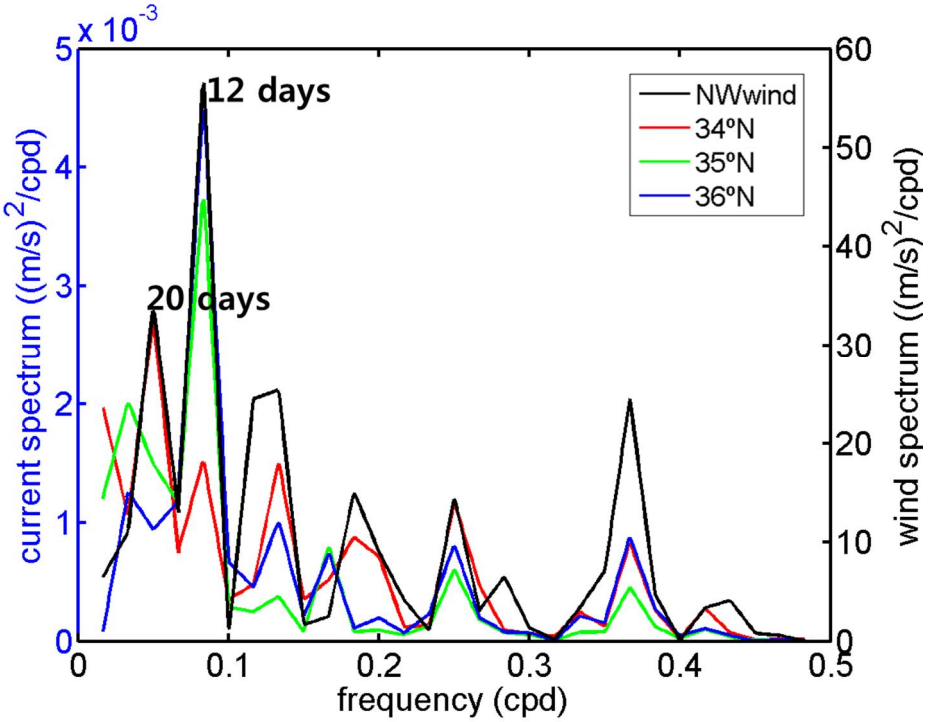

Figure 2. 7 Periodogram of (black line) daily mean northwesterly wind averaged over the Yellow Sea and daily mean meridional velocities of subsurface water across (red line) 34° N, (green line) 35° N, and (blue line) 36° N.

2.4.3 Correlation between northwesterly wind and meridional flow

To investigate the formation of the wind-driven flows and their evolutions in response to the northwesterly wind, the time-lagged correlation coefficients (R) between the northwesterly wind and the meridional flow were calculated. Figure 2.8 shows the horizontal distributions of the lagged correlation coefficients between the northward velocity and the northwesterly wind (positive when waters flow to the north and winds blow from the northwest to the southeast). The correlation coefficients above 0.26 are significant with 95 % confidence level.

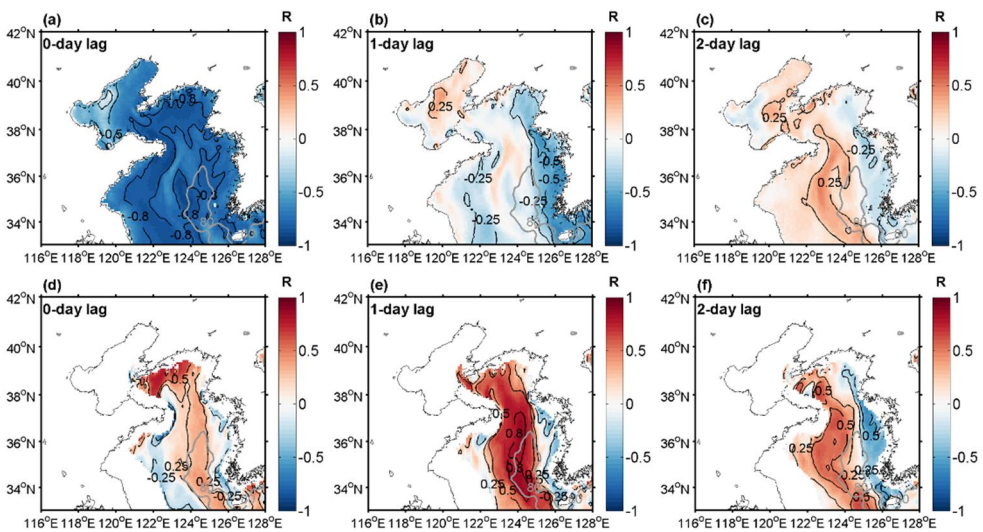

Figure 2. 8 Time-lagged correlation coefficients between northwesterly wind and the daily mean meridional velocities with lags of (a and d) zero, (b and e) one day, and (c and f) two days. The upper and lower panels show the correlation coefficients for

the surface flow and the subsurface flow, respectively. A grey solid line in the middle of the Yellow Sea indicates an isobath of 80 m depth.

In Figure 2.8a, strong negative correlations at the zero-day lag indicate that the surface flow responded to the wind variations almost instantly in the entire YS. The subsurface layer flow along the deep channel of the trough and in the northern YS responded to the wind variations without a time lag, and the correlation was positive (Figure 2.8d). This result is consistent with previous studies suggesting that the upwind flow in the trough appears due to sea level differences driven by the surface transport (Park, 1986; Winant, 2004).

The correlation coefficients of the surface flow decreased rapidly with a one-day lag (Figure 2.8b), whereas the flow along the Korean coast had relatively high correlation. The upwind flow in the deep trough showed the maximum correlations with wind variations at the one-day lag (Figure 2.8e). At the two-day lag, the correlations between the wind and the surface flow weakened overall (Figure 2.8c). However, the correlations between the wind and the subsurface flow showed an interesting feature (Figure 2.8f). While the upwind subsurface flow along the western trough remained significant at the two-day lag, a southward-flowing

current strengthened along the west coast of the Korean Peninsula two days after the northwesterly winds became stronger. The intensified region of the upwind flow corresponds to the main path of the YSWC (Figure 2.3b). Taken together, results imply that the westward shift of the YSWC might be closely coupled with the delayed intensification of the southward KCC in response to the northwesterly wind. The correlation coefficient at the three-day lag decreased in all areas of the YS and is not shown here. However, the spatial structure of the negative correlation along the Korean coast and the positive correlation to the west of the trough persisted.

The vertical distributions of correlation coefficients help us to more effectively understand the evolution of the current in response to the wind variations in the YS. Figure 2.9 shows the vertical sections of the lagged correlations between the wind and the meridional flow with lags of zero, one, and two days. A strong negative response appeared instantly in the surface layer of all sections, although a weak positive response appeared in the subsurface layer (Figures 2.9a, d, and g). The thickness of the negative correlation layer was about 20–30 m in coastal areas and about 15–20 m in the trough.

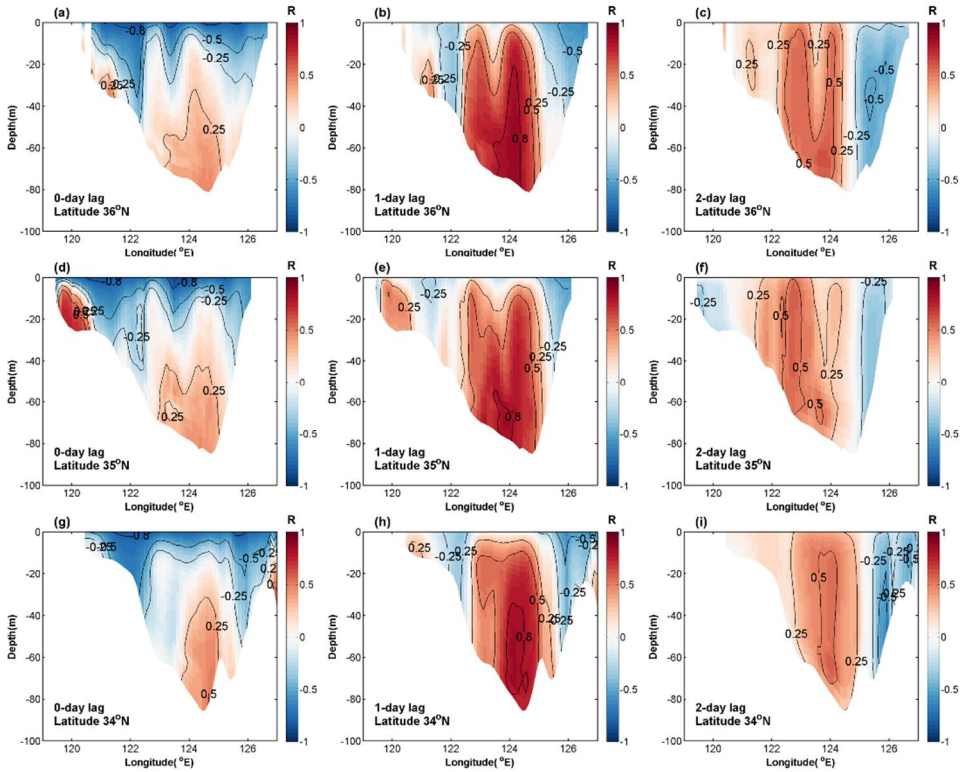

Figure 2. 9 Vertical sections of time-lagged correlation coefficients between northwesterly wind and the daily mean meridional velocities across (top) 36° N, (middle) 35° N, and (bottom) 34° N with lags of (a, d, and g) zero, (b, e, and h) one day, and (c, f, and i) two days.

The distribution of the correlation coefficients at the one-day lag was characterized by a thick layer of strong positive correlations in the central trough that increased in magnitude with an increase in latitude. The downwind currents along the Korean coast remained negatively correlated with the wind at the one-day lag. With a two-day lag, the center of the positive correlations moved to the west of the trough, which coincided with the westward expansion of the negatively correlated coastal water along the

Korean Peninsula.

The temporal sequence of lagged correlations suggests that the wind-driven flow evolves into clockwise subsurface circulation (Figure 2.3b) with a westward shift of northward flow in the subsurface layer flow. When the northwesterly wind starts to blow, the subsurface northward flow began to develop in the middle of the trough, and the flow signal then propagated to the west.

2.4.4 Correlation between northwesterly wind and zonal flow

The correlation analysis between the meridional flow and the wind discussed in the previous section implies potentially significant correlation between the zonal flow and wind according to the mass balance theory. Here, the correlation coefficient between the northwesterly wind and the zonal flow was calculated to examine a more complete structure of the circulation. Figure 2.10 is the same as Figure 2.8 except for the zonal flow (positive when waters flow to the east and winds blow from the northwest to the southeast).

The surface eastward flow showed positive correlations with the wind variations in the northern and eastern YS with no lag (Figure 2.10a). The northwesterly wind was positively correlated with the surface southeastward flow in the northeastern and eastern

YS (Figure 2.10b) and negatively correlated with the surface northwestward flow in the northwestern YS with one- and two-day lags (Figure 2.10c).

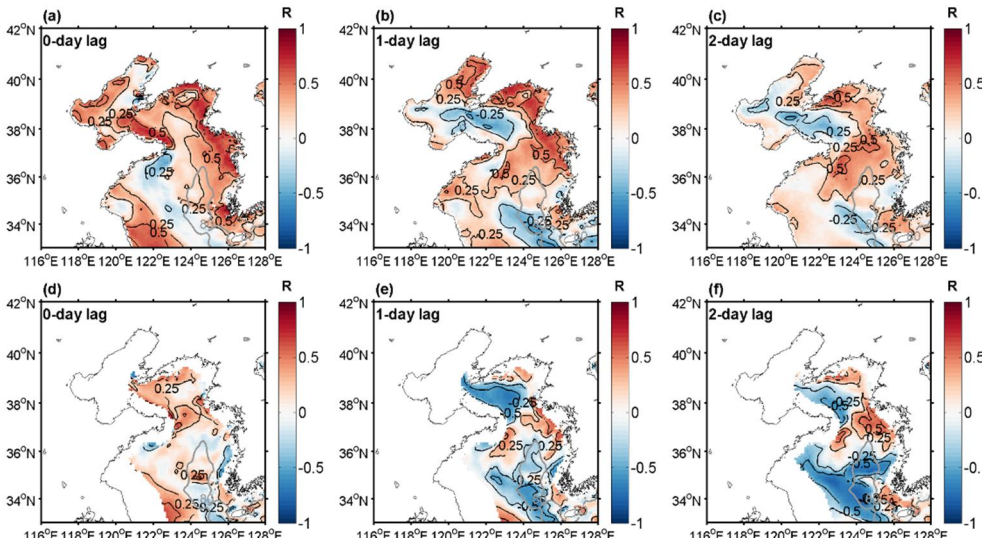

Figure 2. 10 Time-lagged correlation coefficients between northwesterly wind and the daily mean zonal velocities with lags of (a and d) zero, (b and e) one day, and (c and f) two days. The upper and lower panels show the correlation coefficients for the surface flow and the subsurface flow, respectively. A grey solid line in the middle of the Yellow Sea indicates an isobath of 80 m depth.

The eastward flow in the subsurface layer showed positive correlation with the northwesterly wind at the zero-day lag in the YS and negative correlations with the one- and two-day lags in the northwestern and southern YS. The most remarkable negative and positive correlations appeared in the southern YS and in the area between 36° N and 38° N, respectively, with one- and two-day

lags (Figures 2.10e and f). These responses of subsurface meridional and zonal flows to the northwesterly wind suggest that the mean subsurface circulation (Figure 2.3b) is modulated by the strength of the northwesterly wind such that as the northwesterly wind intensifies, the subsurface northwestward flows along the western slope of the YS trough increase one or two days later in the southern YS (122.5–124.0° E, 34.0–35.5° N) and in the northwestern YS (121–123° E, 37.5–38.5° N; Figures 2.8e and 2.8f and 2.10e and 2.10f).

2.4.5 Evolution of actual flow in response to northwesterly wind burst

While a correlation analysis is useful to show a statistical relationship between ocean circulation anomalies and wind anomalies, it does not show how ocean current vectors actually react to an episodic northwesterly wind burst. To further support the statistically significant relations between wind and circulation anomalies, the daily current velocity fields arising after a strong wind burst were investigated in this section. Because a strong northwesterly wind burst occurred on March 1, 2013 (Figure 2.6), the northward velocity distributions during March 1–3, 2013, were compared with the correlation patterns discussed in Sections 2.4.3

and 2.4.4. The horizontal wind distributions during the wind burst period were presented in Figure 2.11 to verify the spatial distributions of surface winds and the strength of the northerly wind component during the same period. The wind distribution on March 1 (Figure 2.11a) showed strong winds from the northwest throughout the region, and the wind was stronger in the eastern YS than that in the western region. The wind distribution on March 2 (Figure 2.11b) was similar to that on March 1, although the wind speed was significantly lower. The northerly wind component disappeared whereas the westerly wind continued to blow on March 3. This strengthening and weakening of the northerly wind component during March 1-3 allowed for examination of the evolution of the wind-driven flows in response to wind change.

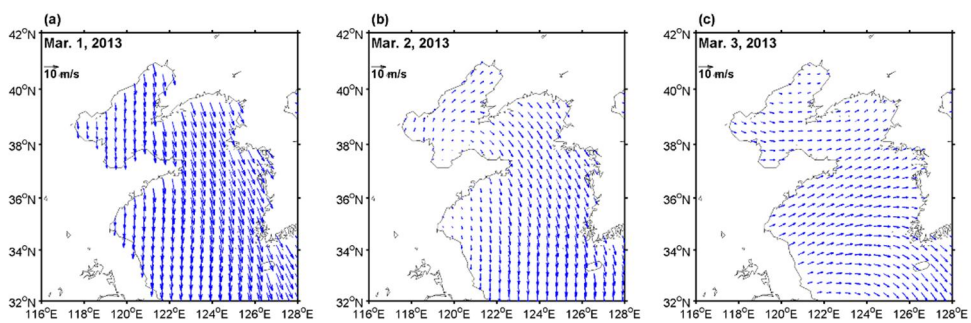

Figure 2. 11 Daily mean surface wind field during March 1-3, 2013.

To confirm that the evolution of the current velocity patterns in response to the wind changes are consistent to the variations in correlation patterns, the daily mean horizontal distributions of the

surface and subsurface currents during March 1–3 were analyzed (Figure 2.12). Although surface downwind flows were generated in the entire YS immediately after the wind burst, relatively small response was detected in the subsurface layer on March 1. One day after the wind burst, a northward upwind flow was generated in the subsurface layer in the central trough, whereas the downwind flows along both the Korean and Chinese coasts were maintained. The downwind flow along the Korean coast was stronger than that along the Chinese coast (Figure 2.12b). One possible explanation is the difference in the strength of the northwesterly wind between the western and eastern YS (Figures 2.11a and b). Two days after the wind event, the downwind flow existed only along the Korean coast. The upwind flow was maintained, although its main path shifted to the west of the trough, and its strength weakened. The vertical sections of the northward velocity (Figure 2.13) were also examined for comparison with the pattern of the correlation coefficients (Figure 2.9). The upper panels in Figure 2.13 show the vertical sections of the daily mean meridional velocity along 35° N during March 1–3, and the lower panels show those along 36° N for the same period. Both sections have similarities, although the northward flow generated at 36° N on March 2 shifted farther to the west of the trough than that generated at 35° N. These changes

in the current velocity distribution pattern, which represent the evolution of the wind-driven flows, are similar to those in the pattern of the correlation coefficients.

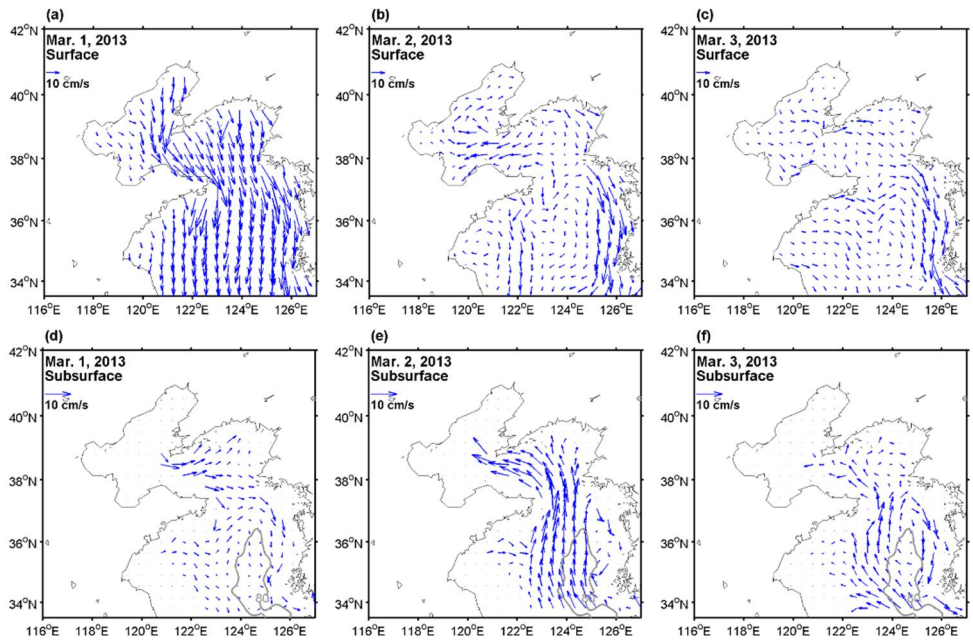

Figure 2. 12 Daily mean horizontal distributions of (a-c) surface current and (d-f) subsurface current during March 1-3, 2013.

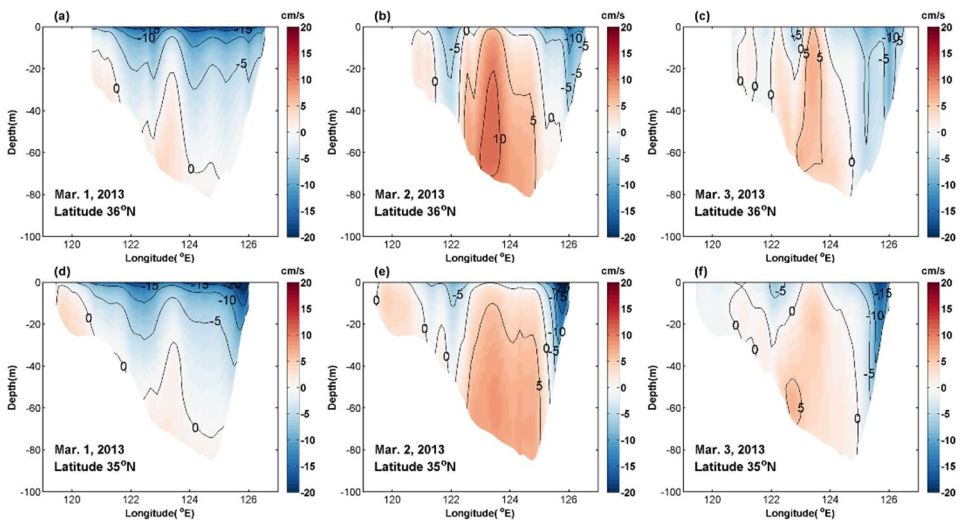

Figure 2. 13 The vertical sections of daily mean meridional velocity

across (a–c) 36° N and (d–f) 35° N during March 1–3, 2013. Positive values represent northward flow.

2.5. Summary

Ocean circulation driven by realistic winter atmospheric forcings in the YS was successfully simulated by the ROMS. Southward current driven by the northwesterly wind was stronger along the Korean coast than along the Chinese coast at the surface. Monthly mean current from the model simulation showed a clockwise circulation in the subsurface layer in the southern YS. The prominent flow pattern in the subsurface layer was the northward YSWC in the west of the trough, which was consistent with the recent currentmeter observation. Meridional flow in the subsurface layer existed persistently in the western trough, and its variation was coherent with wind fluctuations that had dominant variabilities at 12– and 20–day periods.

A time–lagged correlation analysis suggests that the downwind flow at the surface responds instantly to variations in northwesterly wind, which prevails over the entire YS in winter (Figure 2.14). The surface flow in the upper part of the eastern YS is still influenced by wind variations with a one–day lag, although the subsurface water does not respond promptly to wind variations.

Instead, the upwind current in the bottom layer within the trough responds to the wind variations with a one-day lag. After two days, the upwind flow shifts to the west of the trough as the downwind flow along the Korean coast strengthens. Simultaneously, the westward flow in the southern YS is intensified significantly. These responses of the currents to the wind variations result in a strengthened clockwise circulation in the YS when the northwesterly winds become stronger.

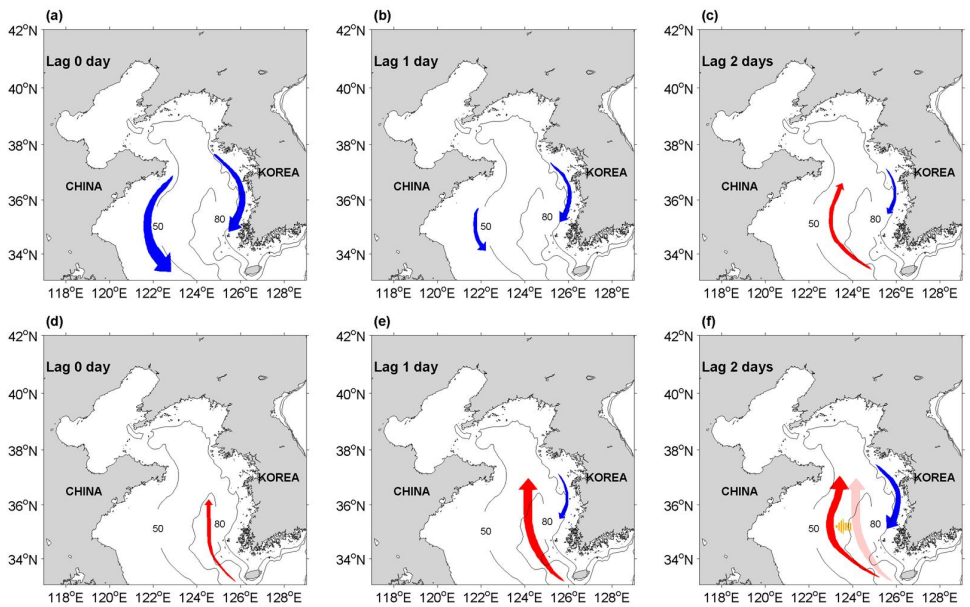

Figure 2. 14 Schematic diagram of Yellow Sea circulation in (upper panels) the surface layer and (lower panels) the subsurface layer. The ocean circulation response to the northwesterly wind is shown with time lags of (a and d) zero, (b and e) one day, and (c and f) two days.

3. Numerical investigation of the generation of continental shelf waves and their role in the westward shift of the YSWC

3.1. Introduction

Continental shelf waves (topographic Rossby waves) that conserve potential vorticity with significant bathymetric changes propagate to the right in the Northern Hemisphere, relative to the coast or shallow regime, after being generated by atmospheric forces, such as winds and changes in pressure (Buchwald and Adams, 1968; Adams and Buchwald, 1969). It is well known that CSWs can modify components of ocean circulation, such as the meandering of the Gulf Stream, upwelling and shelf circulation (Gill and Clarke, 1974; Brooks, 1978; Csanady, 1997). Several studies have been conducted in an attempt to reveal the effect of CSWs on the YSWC based on observations and model experiments (Hsueh and Pang, 1989; Jacobs et al., 1998; Teague and Jacobs, 2000).

Continental shelf waves in the YS were first examined by Hsueh and Pang (1989), who described the dispersion relationship of CSWs in a double-shelf channel and the mechanism for YSWC generation by analysing observed SSHs. Using satellite observed SSH and numerical model simulations, Jacobs et al. (1998)

suggested that coastally trapped waves (defined as a combination of CSWs and internal Kelvin waves) generated by strong northerly winds propagate equatorward along the Chinese coast.

The effect of coastally trapped waves on the YSWC has been studied using numerical models. Based on two-dimensional (2-D) barotropic models, Takahashi et al. (1995) and Lin and Yang (2011) proposed that the large clockwise circulation driven by CSWs is formed by balancing wind forcing with the topographic beta. Takahashi et al. (1995) further indicated that the YSWC departed from the circulation in the YS, with a path close to the Chinese coast, but far from the trough. Lin and Yang (2011) showed that moderate bottom friction controlled the path of the YSWC by shifting the current toward the trough. Yuan and Hsueh (2010) have also suggested the possibility that CSWs drive the westward shift of the YSWC by depressing the sea level along the Chinese coast of the YS. Based on observations and three-dimensional (3-D) numerical model experiments, Qu et al. (2018) suggested that the asymmetrical structure of CSWs is strongly related to the westward shift of the YSWC. Meanwhile, Ding et al. (2018) proposed that the YSWC may be intensified when the westward barotropic pressure gradient is enhanced due to the propagation of coastally trapped waves. Li and Huang (2019) interpreted SSHs and current

responses to synoptic winter winds with Kelvin and CSWs in the YS. Despite many studies on the relationship between CSWs and the westward shift, the generative mechanism of CSWs and the relationship between their propagation and the evolution of the westward shift remain unclear. Thus, numerical model experiments were used in this study in an attempt to elucidate the generative mechanism and role of CSWs on the westward shift of the YSWC.

3.2. Model configuration

The ROMS was used to examine the effect of CSWs on the westward shift of the YSWC. A third-order upstream horizontal advection scheme and fourth-order centred vertical advection scheme were used for the momentum and tracers (Shchepetkin and McWilliams, 2005). The bottom drag stress was calculated using a quadratic bottom stress scheme, and the drag coefficient was set to 2.6×10^{-3} (Moon et al., 2009; Yanagi and Takahashi, 1993). Radiation and reduced-physics schemes were used for the western, eastern and southern lateral boundary conditions. The horizontal viscosity of the domain was set to $100\ m^2\ s^{-1}$. To exclude the baroclinic effect, temperature and salinity were set uniformly at 10℃ and 34 g/kg, respectively, over the entire domain.

Experiments were performed on an f-plane with a Coriolis parameter set to $8.34 \times 10^{-5}\ s^{-1}$ at 35° N because the contribution of the variation in the water column thickness associated with the bottom topography to the potential vorticity change was much larger than that of the planetary vorticity in the YS (Naimie et al., 2001). The model was forced by a northerly wind blowing at 8 m/s on day 1. No wind was assumed for days 2–10. The model ran for ten days to evaluate the generation and evolution of CSWs.

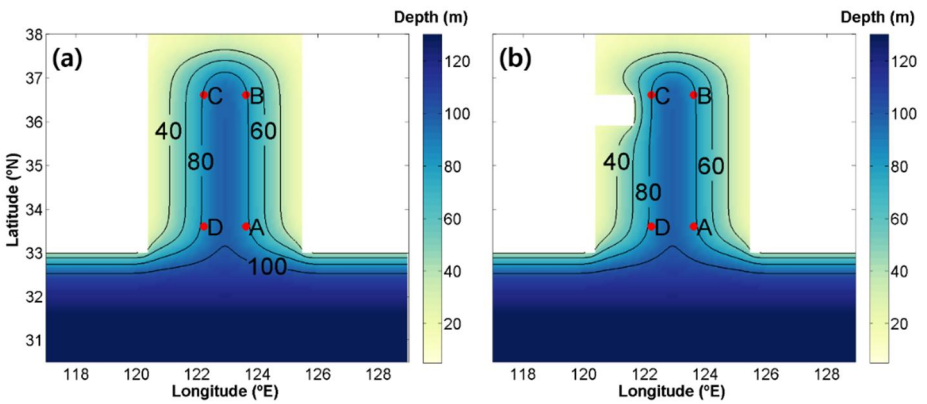

Figure 3. 1 Model domains for (a) experiments a and d; (b) experiment e. The depths (m) are shaded, and the red dots A–D on the 80-m isobath line represent boundaries on the eastern (points A–B), northern (B–C) and western (C–D) slopes.

A model domain ranged from 30.5–38° N and from 117–129° E. The horizontal grid spacing was 10 km with 20 vertical layers. The YS was simplified to an Ω-shaped bay to better investigate the mechanism(s) underlying the westward shift (Figure 3.1a). The model domain also had a meridional trough with a water depth of 95

m in the centre of the basin. I assumed that depth decreased symmetrically in the zonal direction, although the realistic bathymetry in the YS includes an asymmetrical slope; however, this assumption was reasonable given that previous studies have shown that the shift of the YSWC occurs regardless of the symmetry of the slope gradient in the YS (Xing and Huang, 2010; Qu et al., 2018). Two symmetrical slopes were connected by the northern slope, and I placed a sponge layer in a large southern basin to avoid boundary effects by increasing viscosity in a linear manner from $100\ m^2\ s^{-1}$ at 33° N to $10^5\ m^2\ s^{-1}$ at 30.5° N.

Various experiments using different boundary and topographic conditions were conducted to identify the generation of the CSWs (Table 3.1). Experiment a (Exp. a) was a control run used to examine the westward shift of the YSWC in an idealized domain. Experiment b (Exp. b) was the same as Exp. A, except for having an extended flat region from 38– 50° N, with a water depth of 10 m. The viscosity of the extended region increased linearly from $100\ m^2\ s^{-1}$ at 44° N to $1.2 \times 10^5\ m^2\ s^{-1}$ at 50° N. The northern radiation boundary condition was used to investigate CSW generation only. In Experiment c (Exp. c), I assumed a Γ−shaped slope without an eastern slope to exclude CSWs along the eastern slope. Experiment d (Exp. d) was the same as Exp. A, except for

the periodical wind conditions. A peninsula was added to the idealized topography for Experiment e (Exp. e) in order to examine the influence of the Shandong peninsula on the westward shift of the YSWC. Realistic topography was used for Experiment f (Exp. f); experiments g and h (Exp. g and Exp. h) were conducted with realistic topography, but without the eastern and northern slopes, respectively.

Table 3. 1 Description of various model experiments (Exp.).

Exp.	Domain	Northern boundary	Shape of topography	Wind condition
a	Figure 2a	Closed	Ω-shaped	8 $m\,s^{-1}$ for one day
b	Figure 7a	Open	Ω-shaped	8 $m\,s^{-1}$ for one day
c	Figure 7b	Open	Γ-shaped	8 $m\,s^{-1}$ for one day
d	Figure 2a	Closed	Ω-shaped	Periodic wind for a 7-day period
e	Figure 2b	Closed	Ω-shaped with peninsula	Periodic wind for a 7-day period
f	Figure 16a	Closed	Realistic	26 Feb.–5 Mar. 2013
g	Figure 16b	Closed	Γ-shaped	26 Feb.–5 Mar. 2013
h	Figure 16c	Closed	Channel	26 Feb.–5 Mar. 2013

3.3. Results and Discussion

3.3.1 Westward shift of upwind flow with equatorward propagation of CSWs along the Chinese coast

An idealized model experiment (Exp. a) was conducted to simulate the westward shift of an upwind flow. The distributions of the depth-averaged velocity and SSH anomaly for Exp. a are shown

in Figure 3.2. The path of an upwind flow was defined as the maximum northward velocity, and an anticyclonic (cyclonic) vortex formed early on due to northerly wind bursts on the eastern (western) slope, and subsequently propagated to the north (south) over time (Figure 3.2a). Upwind and downwind flows were generated in a deep trough and along the eastern and western boundaries, respectively. After the anticyclonic vortex reached the northern boundary, the vortex moves along the northern slope to the west and to the south along the western slope (Figure 3.2b). Meanwhile, the upwind flow shifted to the west side of the trough. A westward shift in the current occurred from north to south (Figure 3.2c). Flows that were nearly parallel to SSH contours implied a geostrophic balance. The downwind flow decreased along the western boundary, but increased along the eastern boundary over time. After 45 hours, the cyclonic vortex almost disappeared, while the anticyclonic vortex remained. This anticyclonic circulation, which was induced by the wind burst, is representative of a typical flow pattern during winter (Yanagi and Takahashi, 1993; Takahashi et al., 1995; Tak et al., 2016). The shift in the upwind flow and the southward current along the deep trough after 60 hours is exaggerated Figure 3.2d when compared to prior observations (Teague and Jacobs, 2000; Yu et al., 2010; Lin et al., 2011), and

was considered in detail in this study. However, the model results clearly showed the propagation of the vortex and the westward shift of the upwind flow.

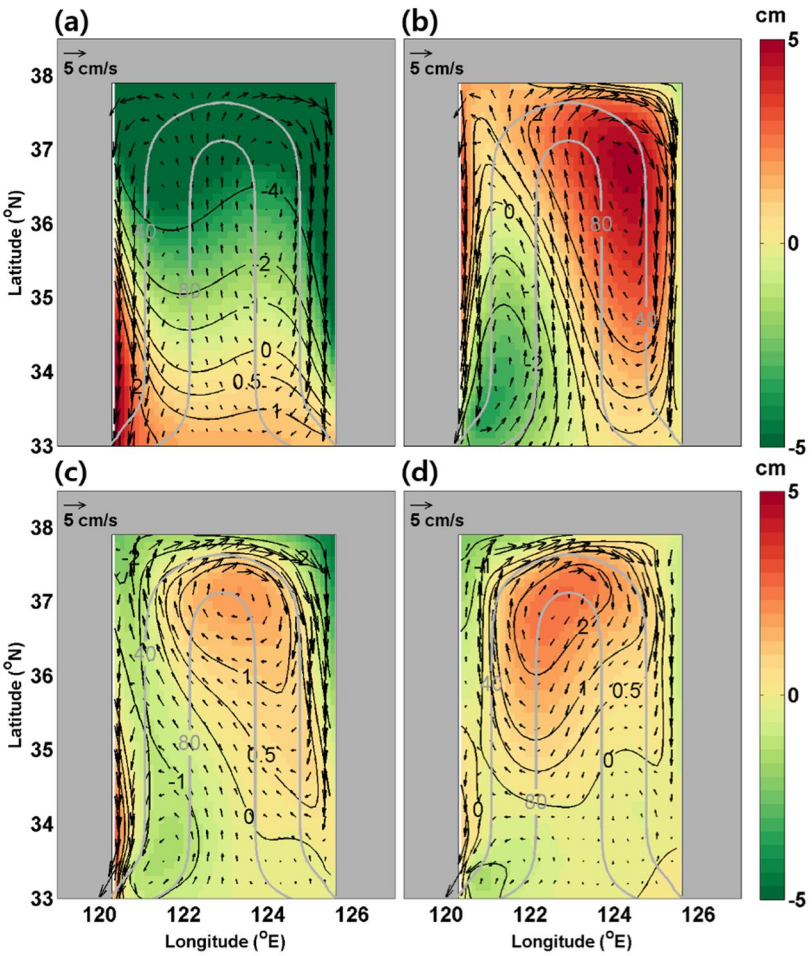

Figure 3. 2 Horizontal distributions of the depth-averaged velocity ($cm\,s^{-1}$, vectors) and sea surface height (SSH) anomaly (cm, shaded) from Exp. a at (a) 15, (b) 30, (c) 45 and (d) 60 hours. Red and green areas indicate positive and negative SSH anomalies, respectively. Grey lines denote depths of 40 and 80 m.

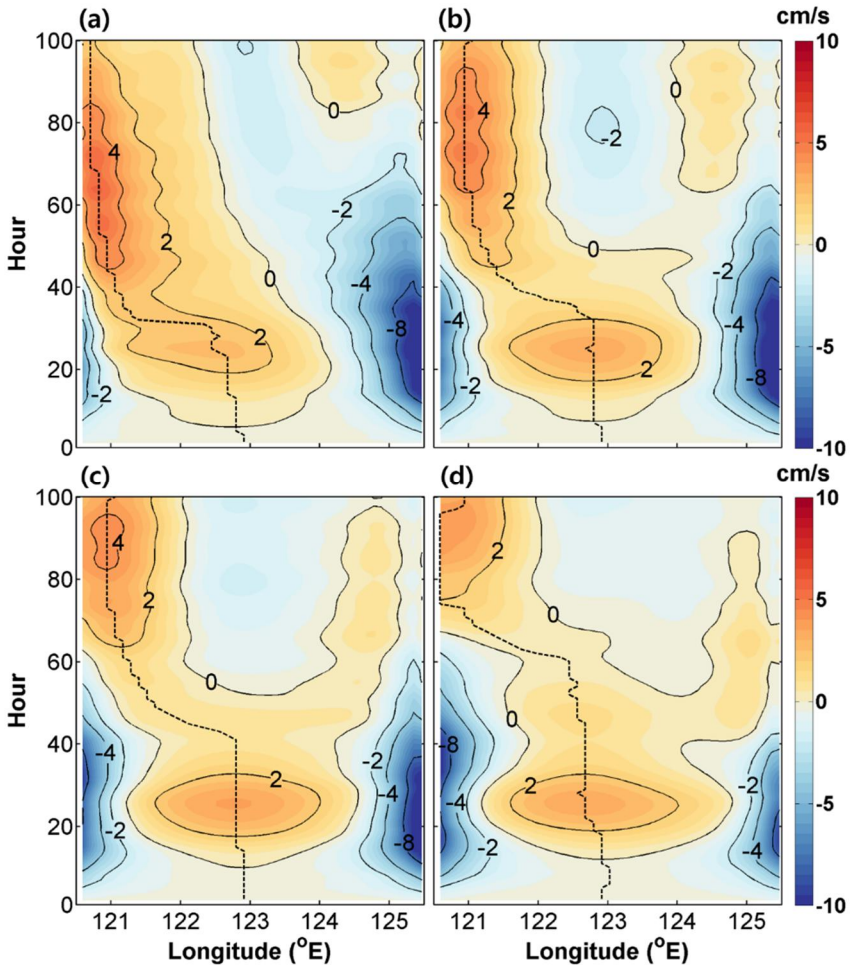

Figure 3. 3 Hovmöller diagrams of the depth-averaged meridional velocity ($cm\,s^{-1}$, shaded) along 37° N (a), 36° N (b), 35° N (c) and 34° N (d) in Exp. a. The y-axis represents the time from the onset of the northerly wind burst. Red and blue areas indicate northward and southward velocities, respectively. The black dashed line indicates the position of the maximum northward (upwind) velocity.

Hovmöller diagrams of the depth-averaged meridional velocity along latitudes 37° N, 36° N, 35° N and 34° N reveal that the westward shift of an upwind (northward) flow occurred at different

times (Figure 3.3). The shift time of the upwind flow was defined as the time when the position of the maximum upwind velocity passed 122° E, which occurred at 31, 38, 46 and 62 hours and at latitudes of 37° N, 36° N, 35° N and 34° N, respectively. The shift began at higher latitudes and progressed equatorward, and the propagation speed of the shift was defined as the speed of the westward shift of the maximum upwind velocity propagating from the north to south, which was calculated using the time when the westward shift occurred at each latitude. The propagation speed of the shift ranged from 1.92–4.80 $\mathrm{m\,s^{-1}}$, with a mean speed of 2.99 $\mathrm{m\,s^{-1}}$.

The equatorward propagation speed of the westward shift of the upwind flow could also be estimated using a Hovmöller diagram of the SSH anomaly along the 80-m isobath line (Figure 3.4). At the initial state, the SSH decreased in the northern region but increased in the south, owing to the northerly wind burst. A positive SSH signal in the southern region then propagated poleward along the eastern slope (points A–B, Figure 3.4). This SSH signal mainly propagated between 27 and 33 hours, with a poleward propagation speed of 15.87 $\mathrm{m\,s^{-1}}$. Some parts of the positive SSH anomaly that reached the north propagated quickly, at 15.87 $\mathrm{m\,s^{-1}}$, while others propagated slowly and in an anticlockwise fashion along the

northern and western slopes (points B–D) between 40 and 99 hours, at a speed of 1.64 $\mathrm{m\,s^{-1}}$.

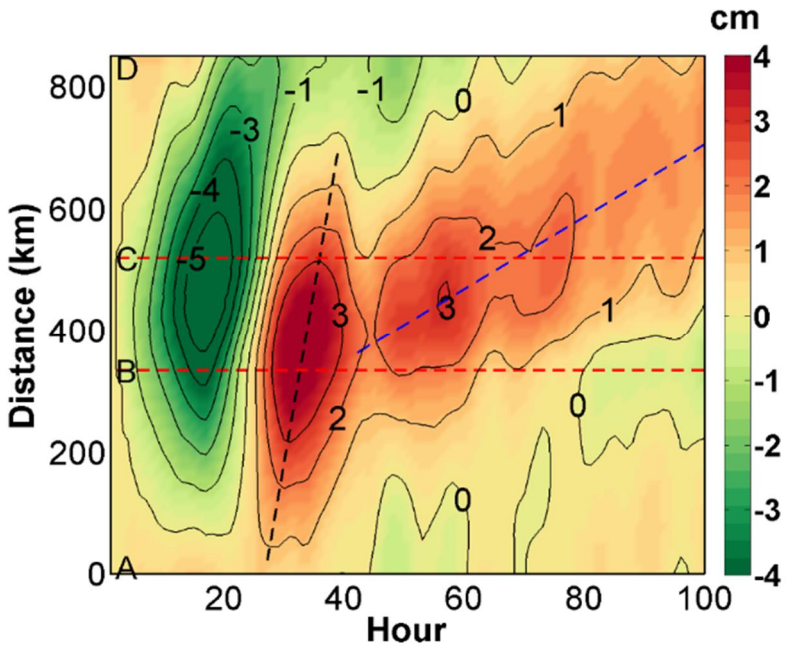

Figure 3. 4 Hovmöller diagram of the SSH anomaly (cm, shaded) along the 80-m isobath line in Exp. a. The x-axis shows the time from the onset of a northerly wind burst and the y-axis indicates the distance from point A along the 80-m isobath line in Figure 2a. Red dashed lines indicate points B and C in Figure 2a; red and green areas represent positive and negative anomalies of SSH, respectively. Black and blue dashed lines are the lines of linear fit along the maximum positive anomalies. They denote the propagation of positive SSH at phase speeds of 15.87 and 1.64 m/s, respectively. The squared Pearson's correlation coefficients ($\boldsymbol{r^2}$) and the p-values ($\boldsymbol{p}$) for these lines were $\boldsymbol{r^2 = 0.96}$ ($\boldsymbol{p < 0.01}$) and $\boldsymbol{r^2 = 0.93}$ ($\boldsymbol{p < 0.01}$), respectively.

A westward shift occurred within two days after the wind burst,

whereas the maximum positive SSH propagated later. Despite this difference, the maximum positive SSH was selected to calculate propagation speed instead of the more complicated front lines of the vortex, which correspond to the maximum velocity of the upwind flow. Although the propagation of the westward shift of the upwind flow preceded the propagation of the maximum positive SSH, both of them captured the same anticyclonic vortex at the same speed. The propagation speed along the western slope was comparable to that of the westward shift of the estimated upwind flow (Fig. 4), implying that the westward shift is strongly related to the equatorward propagation of the SSH signal.

3.3.2 Characteristics of CSWs driving westward shifting

Barotropic (external) Kelvin waves, which are distinct from the internal Kelvin waves and CSWs known as coastally trapped waves, propagate in the same direction (i.e., to the rights relative to the coast or shallow regime in the Northern Hemisphere, but at markedly different speeds, as Kelvin waves propagate faster). According to Thomson (1880), the phase speed of an external Kelvin wave in the YS is 21 $\mathrm{m\,s^{-1}}$, similar to the propagation speed of the SSH anomaly along the eastern boundary (black dashed line

in Figure 3.4). The propagation of Kelvin waves along the eastern coast and its effect on the strength on the YSWC have been explored in previous studies (e.g., Ding et al., 2018; Li and Huang, 2019). However, the typical propagation speed of an external Kelvin wave is much higher than those of the westward shift and other waves, such as coastally trapped waves.

Hsueh and Pang (1989) proposed a dispersion relationship for CSWs in an infinitely long channel with double-shelf topography. The relationship was evaluated on the f-plane assuming that the horizontal divergence, bottom friction, time tendency of atmospheric pressure, horizontal diffusion, beta effect and the effect of nonlinearity were absent. The governing equation for pressure (p) is then:

$$\frac{\partial}{\partial x}\left(H\frac{\partial^2 p}{\partial x \partial t}\right)+H\frac{\partial^3 p}{\partial y^2 \partial t}+f\frac{\partial H}{\partial x}\frac{\partial p}{\partial y}=f\left(\frac{\partial \tau_y}{\partial x}-\frac{\partial \tau_x}{\partial y}\right), \qquad (3.1)$$

where H, g, τ_x and τ_y denote the depth, gravity acceleration, zonal and meridional components of the wind stress, respectively. All experiments conducted in this study were performed with spatially constant northerly winds such that the spatial derivatives of the wind stress could be ignored. I could thus assume a solution of the following form:

$$p = X(x)exp\{i(ly+\omega t)\}, \qquad (3.2)$$

where X, l and ω refer to the eigenfunction, meridional wavenumber and angular frequency, respectively. Based on the substitution of Equation (3.2) into Equation (3.1) and the boundary conditions described by Pang (1991), I obtain the dispersion relationship:

$$\tanh(n_1 L_1) = -\frac{n_1}{s_1 + s_2}\left\{1 - \frac{\frac{n_2}{s_1 + s_2}}{\tanh(n_2 L_2) + \frac{n_2}{s_1 + s_2}}\right\}; \qquad (3.3a)$$

$$\tanh(n_2 L_2) = -\frac{n_2}{s_1 + s_2}\left\{1 - \frac{\frac{n_1}{s_1 + s_2}}{\tanh(n_1 L_1) + \frac{n_1}{s_1 + s_2}}\right\}, \qquad (3.3b)$$

where the subscripts 1 and 2 refer to the western and eastern slopes and s, L and n are the slope coefficient, width of the slope and eigenvalue, respectively. Moreover:

$$n_1 = \sqrt{\left(s_1^2 - 2s_1\frac{fl}{\omega} + l^2\right)}; \qquad (3.4a)$$

$$n_2 = \sqrt{\left(s_2^2 + 2s_2\frac{fl}{\omega} + l^2\right)}. \qquad (3.4b)$$

The slope coefficients and widths of both slopes were the same ($s_1 = s_2$, $L_1 = L_2$) because I assumed a symmetrical bottom topography. The slope coefficients ($s_1 = 3.02 \times 10^{-6}\ \mathrm{m^{-1}}$) were evaluated using a least squares fitting method for the analytical model (Figure 3.5a). The wavelengths of the CSWs were set to twice the value of the meridional basin scale (1000 km) to obtain

the available wavenumber ($l = 6.28 \times 10^{-6}\ \mathrm{m}^{-1}$; Csanady, 1976).

Based on Equations (3.3a) and (3.3b), the dispersion relationships for the first, second and third modes of the CSWs were estimated (Figure 3.5b). The phase speeds with a wavelength of 1000 km were 2.99, 0.86 and 0.38 $\mathrm{m\,s}^{-1}$, respectively. As shown in Figure 3.5b, the propagation of the positive SSH for Exp. a was equatorward with a speed of 1.64 $\mathrm{m\,s}^{-1}$ and belonged to the first mode of CSWs. The difference between the numerical and analytical solutions may result from bottom friction, as bottom friction may decay the energy of the CSW (Power et al., 1989). Considering the assumptions applied to the dispersion relationship and the bottom friction, equatorward propagation of the westward shift appeared closely consistent with the first mode of CSWs. Although the phase speed of the CSW varies with the bottom topography and winds in the YS, the phase speed of the CSW (~2.31 $\mathrm{m\,s}^{-1}$) obtained from YS current measurements (Teague and Jacobs, 2000) was comparable to the speeds estimated by the numerical and analytical models (Table 3.2).

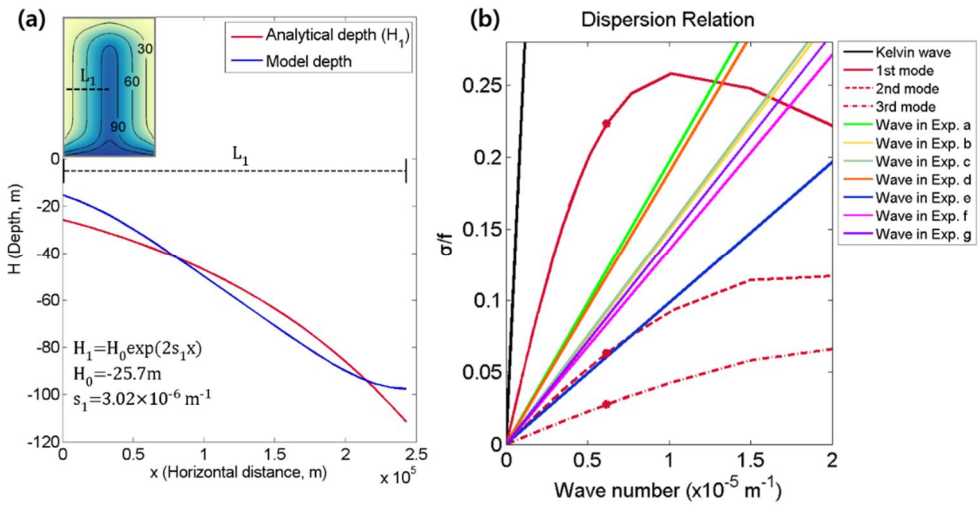

Figure 3. 5 (a) Depth profiles of the numerical model (blue) and analytical model (red) evaluated using the least squares fitting method. The x− and y−axes indicate the distance ($\times \mathbf{10^5\ m}$) from the western boundary and depth (m), respectively; $\boldsymbol{L_1}$ and $\boldsymbol{s_1}$ indicate the width and slope coefficient for the western slope. (b) Dispersion relationships among the Kelvin wave and the first, second and third modes of continental shelf waves (CSWs) for the analytical depth profile and the propagation speeds of the positive SSH from the numerical results. Each red dot on the lines for the analytical depth profiles indicates the value corresponding to a wavelength of 1000 km. The y−axis shows the frequency of the wave ($\boldsymbol{\sigma}$) divided by the Coriolis parameter ($\boldsymbol{f = 8.34\ \times 10^{-5}\ s^{-1}}$).

Table 3. 2 Phase speeds for the analytical and numerical models, as well as observations.

Model/Observation	Phase speed ($m\ s^{-1}$)
Analytical 1st mode of the CSW	2.99
Analytical 2nd mode of the CSW	0.86
Analytical 3rd mode of the CSW	0.38
Wave in *Exp. a*	1.64
Wave in *Exp. b*	1.24
Wave in *Exp. c*	1.26
Wave in *Exp. d*	1.58
Wave in *Exp. e*	0.82
Wave in *Exp. f*	1.13
Wave in *Exp. g*	1.19
Observation (Teague and Jacobs, 2000)	~2.31
Analytical 1st mode of the CSW (Hsueh and Pang, 1989; Qu et al., 2018)	1.89–3.71

3.3.3 Generation of CSWs driving the westward shift of the YSWC

Decay distance is an important factor in clarifying the source of the CSWs driving the westward shift of the YSWC. Since decay distance depends on the bottom resistance coefficient and meteorological forcing, it is not easy to estimate exactly. Hsueh and Pang (1989) estimated that the decay distances of the first mode CSWs in the YS were 245 and 481 km along the eastern and

western slopes, respectively; those of the second and third mode CSWs were much shorter, based on simple models with uncertain friction and topography. If the estimated decay distance is applicable to the YS, most CSWs from the south–eastern slope may decay before reaching the northern slope. Moreover, if the CSWs propagate from the eastern slope, the phase speeds of the CSWs estimated from observations and the analytical model (Table 3.2) are too slow to drive the westward shift, considering the observation that the YSWC occurs on the western slope roughly 1–2 days after the northerly wind burst (Lin et al., 2011). Numerical studies also support the idea that the westward shift occurs with a two–day lag in the wind (Tak et al., 2016; Qu et al., 2018).

Results from Exp. a showed that the westward shift occurred over the entire domain two days after the northerly wind burst. Continental shelf waves that induce the westward shift of the YSWC cannot be generated from the south–eastern YS owing to the decay distance and the long travel time. External Kelvin waves, which may enhance the strength of the YSWC, also appeared as a result of the wind bursts in the YS (Hsueh and Romea, 1983; Hsueh and Pang, 1989; Jacobs et al., 1998; Ding et al., 2018; Qu et al., 2018; Li and Huang, 2019). These waves can transfer some energy to CSWs when propagating into irregular topography by disturbing the

background potential vorticity, which has been referred to as the 'scattering' of Kelvin waves in previous studies (Wilkin and Chapman, 1990; Johnson, 1990, 1993). Thus, some energy from the Kelvin waves propagating across the northern slope of the YS could be scattered into CSWs, while the remaining energy continued to propagate in an anticlockwise fashion along the boundary.

To investigate the generation of CSWs, experiments were performed using modified model domains. Experiment b had the same topography as Exp. a, but Exp. c did not include an eastern slope (Figure 3.6). Experiments b and c had a flat region from 38–50° N, with a water depth of 10 m and an open northern boundary condition such that Kelvin waves propagating northward along the eastern boundary exited through the northern boundary. Initial and wind conditions were the same as those in Exp. a, but the radiation scheme used for the northern boundary was such that Kelvin waves could scatter over the northern slope and exit through the northern boundary.

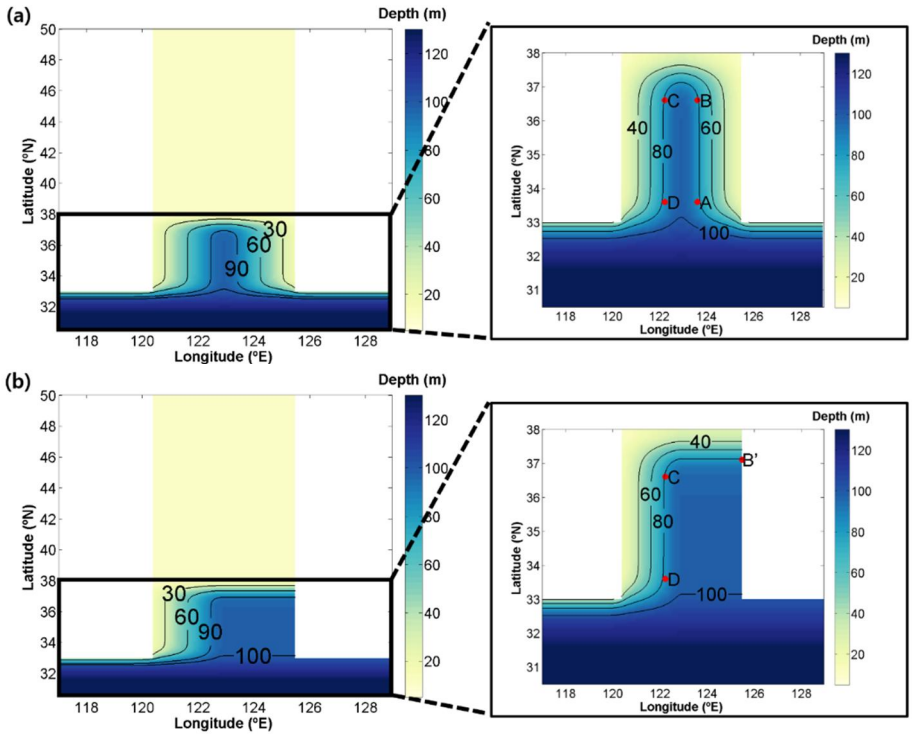

Figure 3. 6 Model domains for (a) Exp. b and (b) Exp. c. Depths (m) are shaded, and the red dots on the 80-m isobath represent boundaries on the eastern (points A–B), northern ((a) B–C, (b) B' –C) and western (C–D) slopes.

Comparing Exps. b and c enables us to identify CSW generation. Figure 3.7 shows horizontal SSH and depth-averaged velocity distributions at 15, 30, 45 and 60 hours from the initial stage in these experiments. The SSH distribution in Exp. b distinctly showed that the anticyclonic vortex propagated along the isobath line. Meanwhile, an upwind flow occurred in the deep trough and shifted to the west side with vortex propagation (Figures 3.7a–d). These results are consistent with those of Exp. a. Although an anticyclonic vortex and downwind flow along the eastern boundary

did not appear in the early stage of Exp. c, the westward shift of the upwind flow propagated with the anticyclonic vortex (Figures 3.7e–h), as in Exps. a and b.

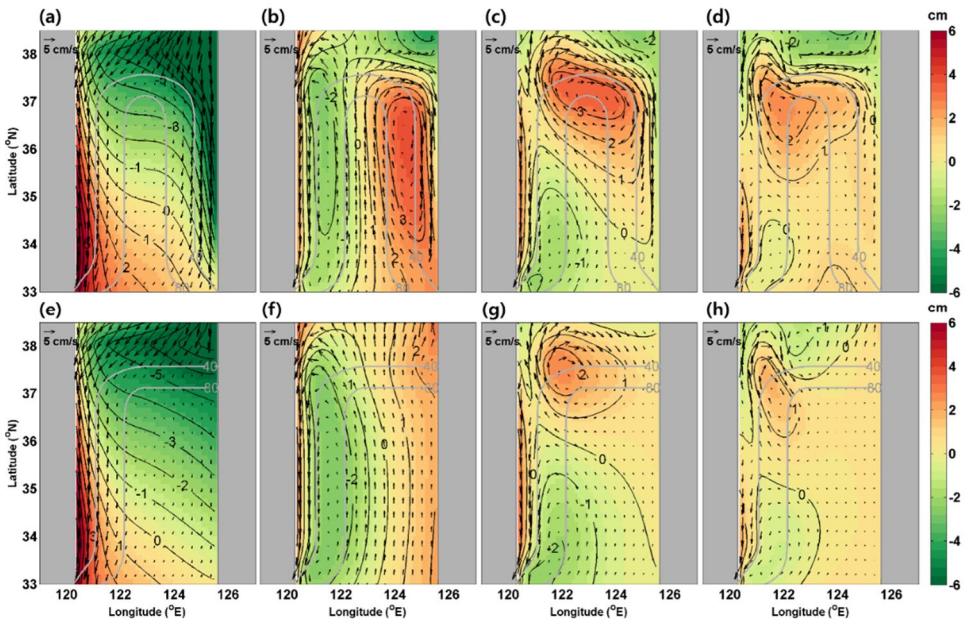

Figure 3. 7 Horizontal distributions of the depth–averaged velocity (**cm s^{-1}**, vectors) and SSH anomaly (cm, shaded) for (top) Exp. b and (bottom) Exp. c at (a, e) 15 hours, (b, f) 30 hours, (c, g) 45 hours and (d, h) 60 hours. Red and green areas represent positive and negative SSH anomalies, respectively. Grey lines denote depths of 40 and 80 m.

Hovmöller diagrams of SSH along the 80–m isobath line (Figure 3.8) show the propagation of the anticyclonic vortices, with speeds of 1.24and 1.26 **m s^{-1}**, respectively, on the western slopes in Exps. b and c. These speeds are comparable to that of the positive signal in Exp. a (Figure 3.4). The positive SSH signal propagated quickly

at 17.01 $\mathrm{m\,s^{-1}}$, which corresponds to the phase speed of the Kelvin waves on the eastern slope (points A–B) in Exp. b (Figure 3.8a). On the northern slope (points B–C) the signal changed speed to 1.24 $\mathrm{m\,s^{-1}}$, corresponding to that of the first mode CSW, and maintained its speed on the western slope. The positive SSH signal also showed the same change in propagation speed on the northern slope in Exp. c, which lacks an eastern slope (Figure 3.8b). The positive anomaly generated on the northern slope (points B' –C) propagated at 1.26 $\mathrm{m\,s^{-1}}$ on the western slope (points C–D). This shows that CSWs are generated on the northern slope when the Kelvin waves along the eastern boundary propagate across the northern slope. Hovmöller diagrams of the meridional velocity along 37° N, 36° N, 35° N and 34° N in Exps. b and c reveal that the westward shift of an upwind flow coexists with the propagation of the anticyclonic vortex in both experiments (Figure 3.9). The Hovmöller diagrams also show the time of the westward shift of the upwind flow at each latitude, which occurred from 37° N to 34° N at 33, 45, 57 and 77 hours at speeds of 1.54–2.57 $\mathrm{m\,s^{-1}}$ in Exp. b and at 31, 44, 60 and 78 hours at speeds of 1.72–2.37 $\mathrm{m\,s^{-1}}$ in Exp. c. The speed of the shift in Exp. b was comparable with that in Exp. c. Figure 3.9 shows that the westward shift appeared concurrently with the propagation of the anticyclonic vortex, moving as fast as

the CSW first mode, regardless of the presence of the eastern slope in Exp. c. This strongly suggests that CSWs driving the shift can be generated from the scattering of Kelvin waves into CSWs when the Kelvin waves cross the northern slope.

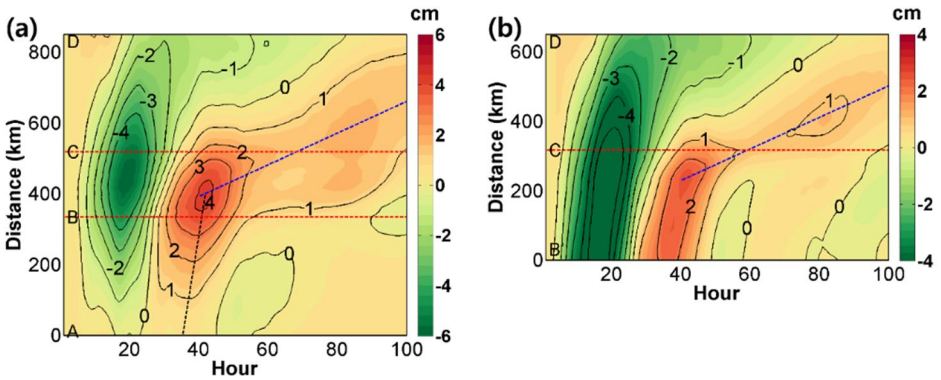

Figure 3. 8 Hovmöller diagrams of the SSH anomaly (cm, shaded) along the 80−m isobath line in (a) Exp. b and (b) Exp. c. The x−axes denote the time from the onset of a northerly wind burst and the y−axes denote the distance from the point (a) A and (b) B' along the isobath line in Figures (a) 7a and (b) 7b, respectively. Red dashed lines indicate points B and C in Figures (a) 7a and (b) 7b. Red and green areas represent positive and negative SSH anomalies, respectively. Black and blue dashed lines in (a) and the blue dashed line in (b) indicate lines of linear fit along the maximum positive anomalies, which denote the propagation of the positive SSH anomalies moving at 17.01, 1.24 and 1.26 $\mathbf{m\,s^{-1}}$, respectively. For the black and blue lines in (a) and the blue line in (b), $\boldsymbol{r^2 = 0.89\ (p < 0.01)}$, $\boldsymbol{r^2 = 0.96\ (p < 0.01)}$ and $\boldsymbol{r^2 = 0.99\ (p < 0.01)}$, respectively.

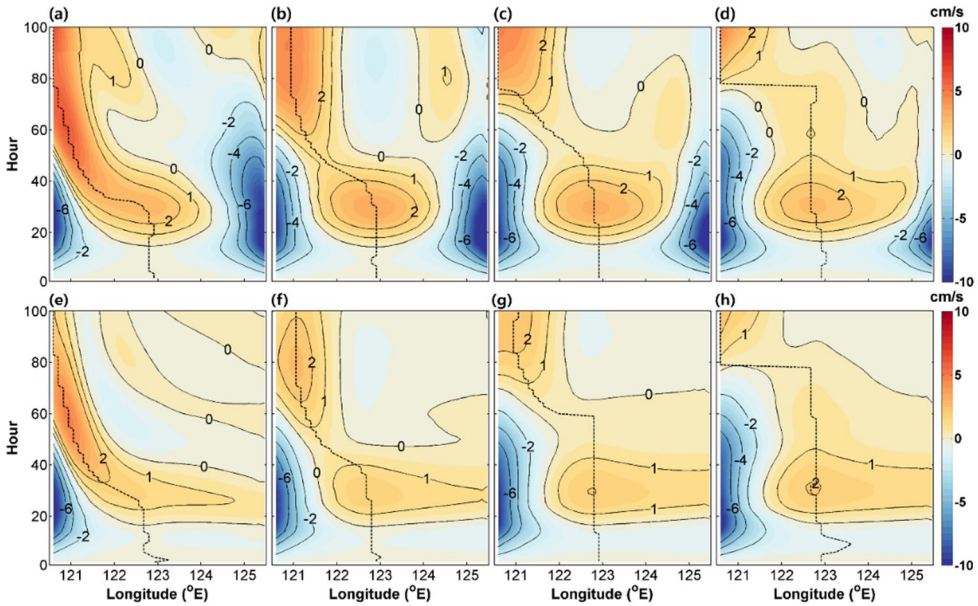

Figure 3. 9 Hovmöller diagrams of the depth-averaged meridional velocity ($\mathbf{cm\,s^{-1}}$, shaded) for (top) Exp. b and (bottom) Exp. c along (a, e) 37° N, (b, f) 36° N, (c, g) 35° N and (d, h) 34° N. The y-axis represents the time from the onset of the northerly wind burst. Red and blue areas reflect northward and southward velocities, respectively. The black dashed line indicates the position of the maximum northward velocity.

To quantify the scattering of Kelvin waves on the northern slope, the energy fluxes of incoming and outgoing Kelvin waves and scattered CSWs on the slope were estimated according to the methods of Spall and Pedlosky (2005). Energy flux was calculated as:

$$E = \int\int \rho g |v| \hbar \, ds \, dt, \qquad (3.5)$$

where ρ, g, $|v|$ and $\hbar$ denote gravitational acceleration, water density, the perpendicular speed to the section and water depth,

respectively. In Exp. b, energy fluxes could include the scattering of the low-mode CSWs into higher mode CSWs because the incident waves had CSWs, as well as Kelvin waves, due to the eastern slope. However, the energy fluxes for Exp. c might show the scattering of the Kelvin waves into CSWs.

Figure 3.10 shows the energy fluxes in the incident, transmitted Kelvin waves and the scattered CSWs on the northern slope from when Kelvin waves reached the slope in Exps. b and c. Energy fluxes in the CSWs increased as those in incident Kelvin waves decreased due to the difference in the phase speed. The fluxes in the incident Kelvin waves and transmitted Kelvin waves decreased simultaneously. The amount of scattering was estimated by comparing energy fluxes between the incident and transmitted Kelvin waves.

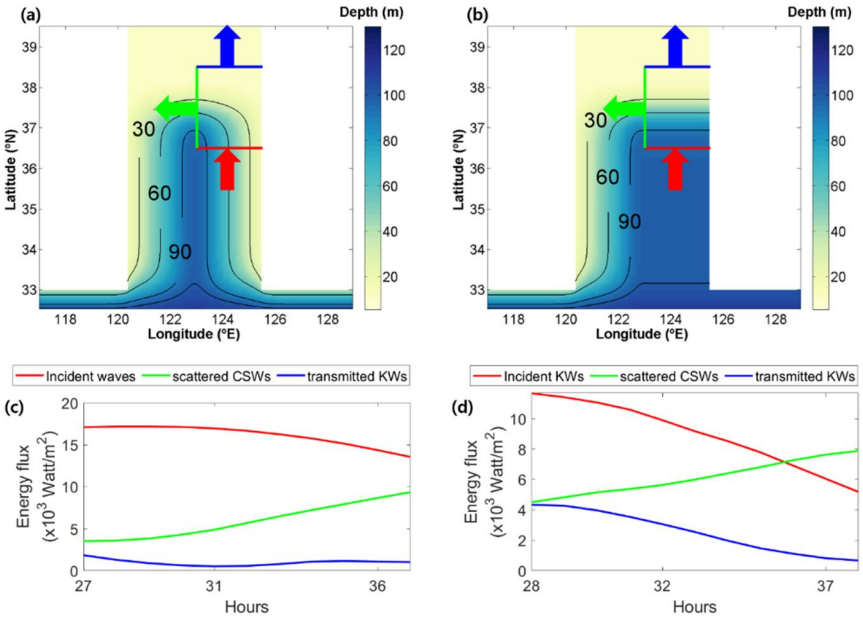

Figure 3. 10 Time series of (c, d) energy fluxes in (red line) incident waves and (blue line) transmitted Kelvin waves (KWs) and (green line) scattered CSWs on the northern slope in (a) Exp. b and (b) Exp. c from 27 and 28 hours, when Kelvin waves reached the northern slope, respectively.

The scattering coefficient (C_{sc}) based on Wilkin and Chapman (1990) is defined as:

$$C_{sc} = 1 - \frac{Energy\ in\ transmitted\ Kelvin\ waves}{Energy\ in\ incident\ Kelvin\ waves}. \qquad (3.6)$$

If there no scattering of Kelvin waves into CSWs occurs, $C_{sc} = 0$. If all of the energy of Kelvin waves scatters into CSWs, $C_{sc} = 1$. The C_{sc} was estimated from the period when the potential vorticity reached its maximum to 10 hours after the incident Kelvin waves propagated fully across the northern slope during the period. For Exp. b, C_{sc} = 0.94, which suggests that 94% of incident waves,

including both CSWs and Kelvin waves, propagated or were scattered along the northern slope, and 6% of the energy continued propagating along the boundary. The C_{sc} for Exp. c is 0.72, indicating that 72% of the energy of Kelvin waves was scattered into CSWs on the northern slope, and 28% of the energy continued propagating along the boundary. These findings suggest that the major source of CSWs on the northern slope originates from the scattering of incident Kelvin waves.

3.3.4 Effects of periodic wind and the Shandong Peninsula on the westward shift of the upwind flow

The results of the idealized model experiment (Exp. a) showed that the shift in the upwind flow was overshot. Previous numerical studies using constant northerly wind conditions have simulated the realistic path of the upwind flow (Lin and Yang 2011; Qu et al., 2018), and Lin and Yang (2011) suggested that the westward shift was controlled by the bottom drag coefficient. However, the path of the upwind flow in Exp. a, which included a comparable bottom drag coefficient to that employed by Lin and Yang (2011), was exaggerated during the wind-free period because the path was determined by the episodic current driven by propagation of the anticyclonic vortex.

The winter wind in the YS is inconstant and periodic (Hsueh and Romea, 1983). Experiment d, with periodic wind, was performed to reflect the realistic wind in the YS. Spectral analysis of winter winds, which was obtained from ERA-Interim reanalysis of the European Centre for Medium-Range Weather Forecasts (ECMWF, 2013) indicated dominant variability with an approximately seven-day period (Figure 3.11a). Periodic winds with a skew-normal distribution of the following form were adopted (Figure 3.11b):

$$V(t) = -\frac{11}{\sqrt{2\pi}} e^{-\frac{(0.7t-0.2)^2}{2}} \left[1 + erf\left(\frac{5(0.7t-0.2)}{\sqrt{2}}\right)\right] \ (0 \le t \le 7), \quad (3.7)$$

where V and *erf* denote the meridional wind speed and error function, respectively. Experiment d was conducted for 21 days.

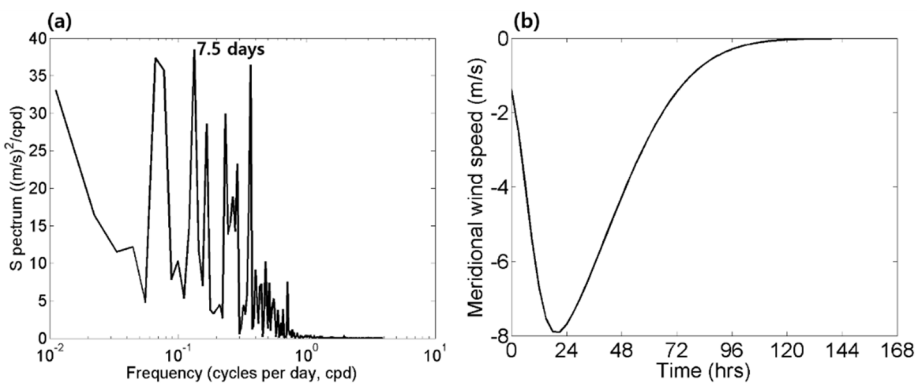

Figure 3. 11 (a) Spectral analysis of meridional wind over the Yellow Sea (YS) from December of 2012 to February of 2013. (b) Time series of the periodic meridional wind for Exps. d and e.

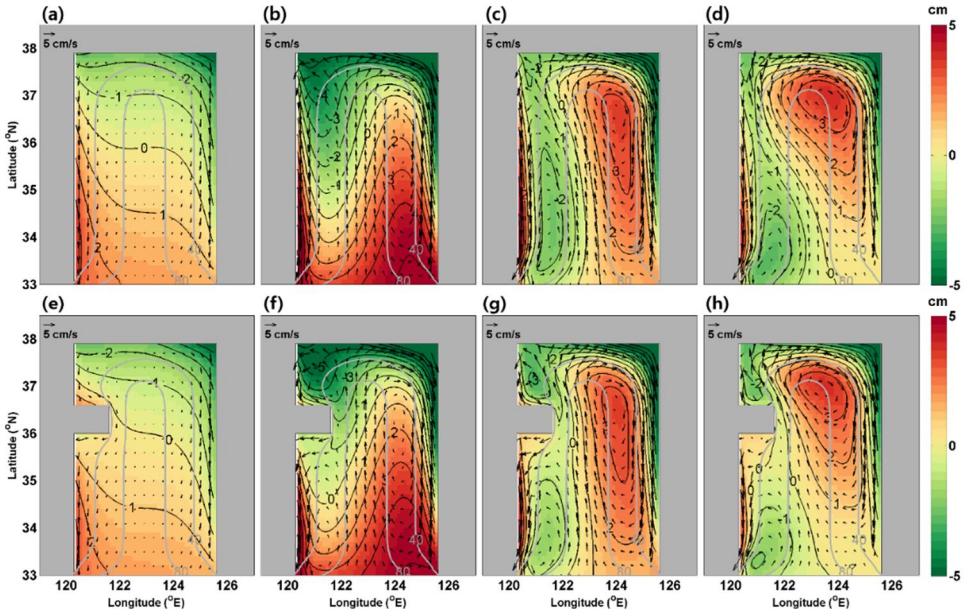

Figure 3. 12 Horizontal distributions of the depth-averaged velocity (**cm s^{-1}**, vectors) and SSH anomaly (cm, shaded) for (top) Exp. d and (bottom) Exp. e at (a, e) 15 hours, (b, f) 30 hours, (c, g) 45 hours and (d, h) 60 hours. Red and green areas represent positive and negative SSH anomalies, respectively. Grey lines denote depths of 40 and 80 m.

The Shandong Peninsula is one of the unique topographic features in the YS. The protrusion of the peninsula may modify the path of the YSWC. To determine the effects of the Shandong Peninsula on the path of the upwind flow, Exp. e was performed with an artificial protrusion representing the peninsula and with periodic wind forcing. Figure 3.12 shows the horizontal distributions of the SSH and depth-averaged velocity from Exps. d and e. The propagation of a positive SSH signal in Exp. d was closely comparable to that in Exp. a (Figures 3.12a-d). However, there was

a delay in the propagation of positive SSH anomalies between Exps. a and d. The vortex propagation in Exp. d begins slightly later than in Exp. a because the periodic wind blows longer than the wind forcing in Exp. a. The overshoot of the westward shift still appeared during the wind relaxation period regardless of the wind forcings. The propagation of the vortex in Exp. e was roughly consistent with that in Exp. d before 45 hours (Figures 3.12e–f). After 45 hours, the vortex shrunk due to the protrusion of the artificial peninsula (Figures 3.12g–h). This result implies that protrusions, such as the Shandong Peninsula, may hamper the westward shift of the upwind flow. Temporal variations in the SSH and the depth–averaged velocity in Exp. e were comparable with those in Exp. f with the realistic topography of the YS.

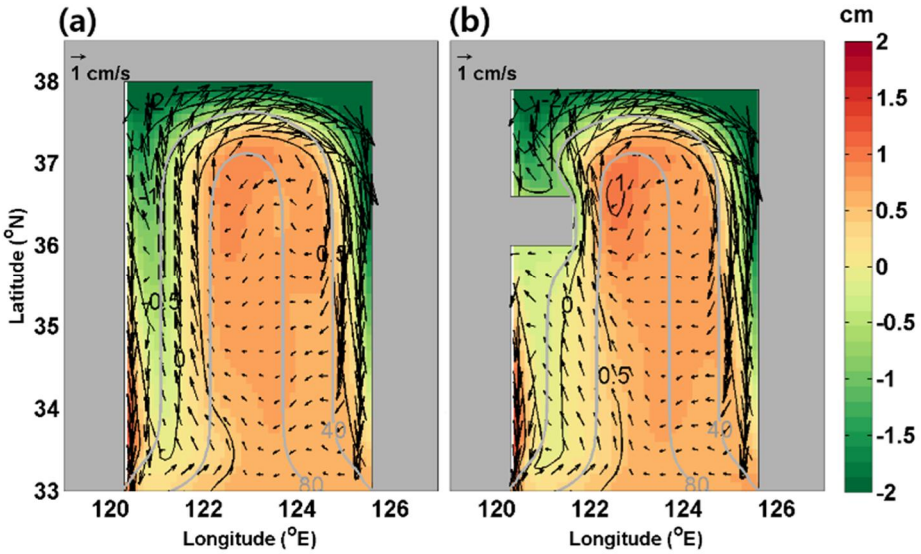

Figure 3. 13 Horizontal distributions of the depth-averaged (mean) velocity (**cm s^{-1}**, vectors) and SSH anomaly (cm, shaded) during the 7-day wind period for (a) Exp. d and (b) Exp. e. Red and green areas represent positive and negative SSH anomalies, respectively. Grey lines denote depths of 40 and 80 m.

Figure 3.13 shows the SSH and depth-averaged (mean) velocity for seven days in Exps. d and e. The mean paths of the upwind flow in both experiments followed the western flank of the trough, and were thus comparable to previous observations, unlike the episodic paths shown in Figure 3.12. The path of the upwind flow in Exp. e with the protrusion was closer to the observed paths. The absence of the Shandong Peninsula in model domains therefore may cause overestimation of the westward shift. Ding et al. (2018) suggested that coastal currents along both coasts and a northward current along the western flank of the trough may be related to the

cumulative effect modulated by the propagation of SSH and driven by coastally trapped waves. This suggests that the propagation of SSHs during the wind relaxation period should be examined, as well as during the wind blowing period, to understand the temporal variation in the YSWC and its mean status.

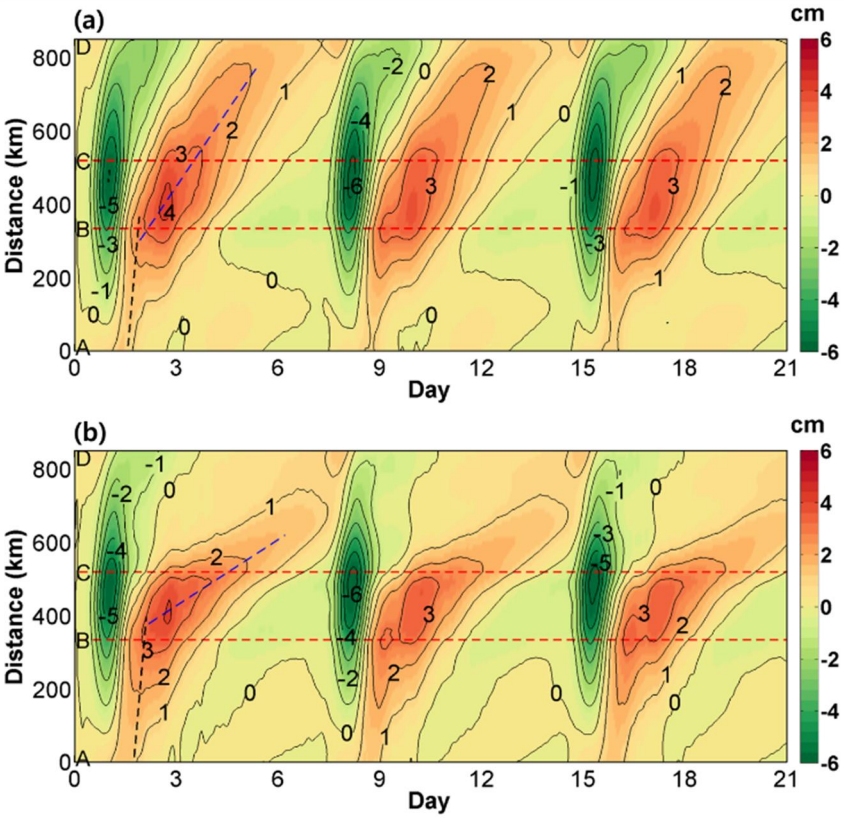

Figure 3. 14 Hovmöller diagrams of the SSH anomaly (cm, shaded) along the 80-m isobath line in (a) Exp. d and (b) Exp. e. The y-axes denote the distance from point A along the isobath line in Figures (a) 2a and (b) 2b, respectively. Red dashed lines indicate points B and C in Figures (a) 2a and (b) 2b. Red and green areas represent positive and negative SSH anomalies, respectively. Black and blue dashed lines indicate lines of linear fit along the maximum

positive anomalies. They denote the propagation of the positive SSH anomalies moving at (a) 12.35, 1.58 $\mathbf{m\,s^{-1}}$ and (b)12.45, 0.82 $\mathbf{m\,s^{-1}}$. For the black and blue lines, (a) $\boldsymbol{r^2 = 0.93\ (p < 0.01)}$, $\boldsymbol{r^2 = 0.96\ (p < 0.01)}$ and (b) $\boldsymbol{r^2 = 0.94\ (p < 0.01)}$, $\boldsymbol{r^2 = 0.98\ (p < 0.01)}$, respectively.

Hovmöller diagrams of the SSH anomaly for both experiments (d and e) were examined to investigate the effect of periodic winds and peninsular protrusion on the propagation speed of the SSH vortex (Figure 3.14). The propagations of positive SSH anomalies in Exps. d and e were fast along the eastern slope (points A–B) and slowed abruptly on the northern slope (points B–C), as in Exp. a. Propagation speeds along the eastern slope in Exps. d and e were 12.35 and 12.45 $\mathrm{m\,s^{-1}}$ and decreased to 1.58 and 0.82 $\mathrm{m\,s^{-1}}$ from the northern slope, respectively, which indicates that the propagation speed of the SSH during the wind relaxation period was not affected by the wind conditions. The protrusion caused wave propagation to slow, and the propagation along the western slope in Exp. e was much slower than the first mode of CSW in the analytical solution (Figure 3.5b) because the domain was modified by considering the protrusion.

3.3.5 Model application to realistic topography in the YS

Additional model experiments with realistic and modified topographies of the YS were conducted to determine if CSW generation drives the westward shift of the YSWC (Figure 3.15). The topography of the realistic model (Exp. f) was derived from the Earth Topography 5 min grid (ETOPO5) dataset (National Geophysical Data Center, 1988). The topographies of Exps. g and h, which were based on Exp. f, had no eastern and northern slopes, respectively, such that the scattering of Kelvin waves and the effect of CSWs along the eastern slope could be examined. Temperature and salinity were homogenised to exclude baroclinic effects, and there was no heat flux through the surface. Winds were obtained from ERA-Interim reanalysis of the European Centre for Medium-Range Weather Forecasts (ECMWF, 2013). Grid resolutions and momentum schemes, such as horizontal advection and vertical mixing, were the same as those used by Tak et al. (2016). Experiments were performed from 26 February to 5 March of 2013 because the wind burst occurred on 1 March 2013 (Figure 3.16a).

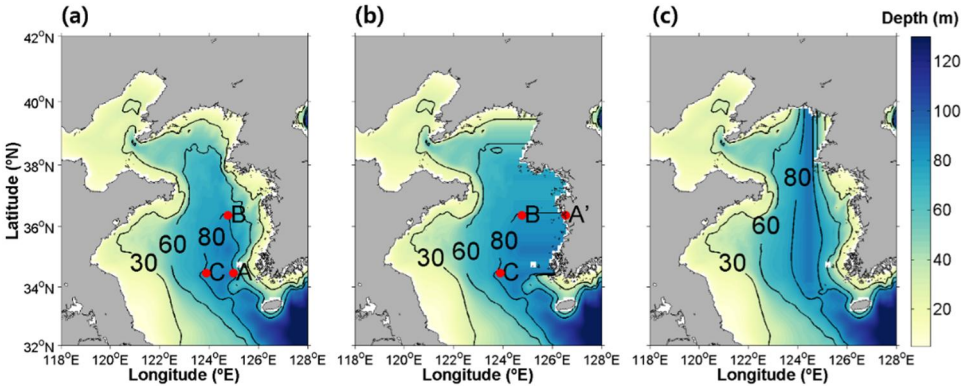

Figure 3. 15 Model domains for (a) Exp. f, (b) Exp. g and (c) Exp. h. Depths (m) are shaded; red dots on the 80-m isobath line separate (a) the eastern (points A–B) and western slopes (B–C) and (b) the northern (A' –B) and western slopes (B–C).

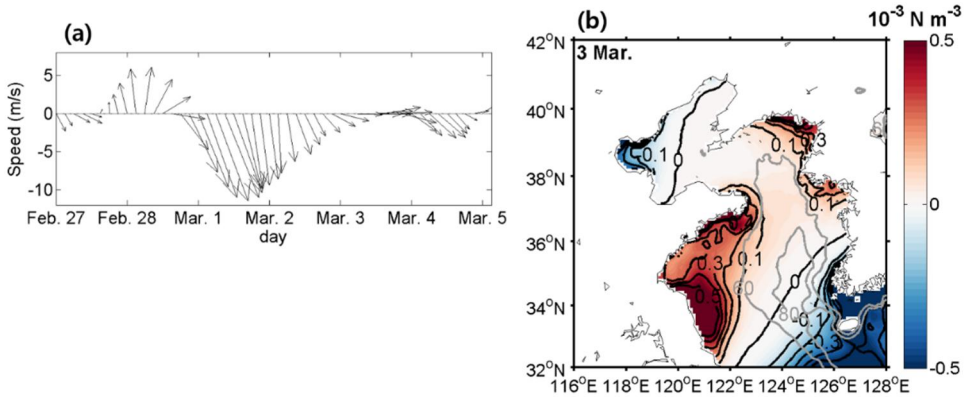

Figure 3. 16 (a) Three-hourly surface wind vector ($\mathbf{m\,s^{-1}}$) averaged over the YS from 27 February to 5 March 2013; (b) daily mean meridional wind stress divided by the distribution of water depth ($\times \mathbf{10^{-3}\,N\,m^{-3}}$, shaded) on 3 March 2013.

Figure 3.17 shows the SSH anomaly and depth-averaged velocity distributions for Exp. f. In the initial stage, the SSH increased in the southern YS and a positive SSH anomaly rapidly propagated along the eastern slope (Figures 3.17a–b). After the

positive SSH anomaly reached the northern slope, some of it propagated in an anticlockwise fashion along the slope, while the rest propagated along the coast of the YS and Bohai Sea (Figures 3.17c–d). These results imply that some of the energy of the Kelvin waves scattered into CSWs, while the remaining energy continued to propagate along the boundary of the YS and Bohai Sea. An upwind flow generated in the trough shifted to the west side of the trough concurrently with the propagation of the positive SSH anomaly trapped on the northern slope (Figures 3.17f–h). These features are consistent with results of Exps. a, d and e.

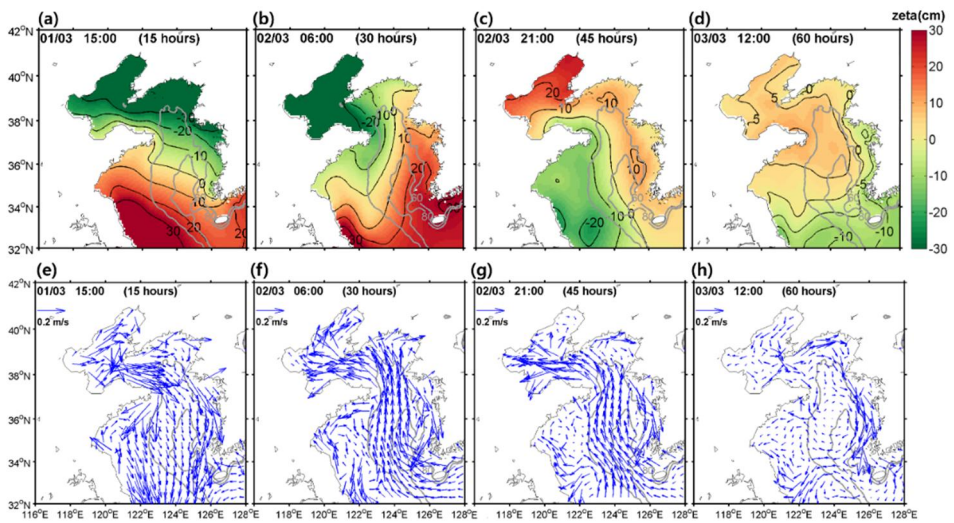

Figure 3. 17 (Top) Horizontal SSH (cm, shaded) and (bottom) depth-averaged velocity distributions for Exp. d at (a, e) 15:00 UTC 1 March, (b, f) 06:00, (c, g) 21:00 UTC 2 March and (d, h) 12:00 UTC 3 March 2013. Red and green areas represent positive and negative SSH anomalies, respectively. Grey lines denote depths of 40 and 80 m.

Hovmöller diagrams of the depth-averaged meridional velocity along the 35.5° N, 35° N and 34.5° N sections in Exps. f, g and h displayed the propagation of the westward YSWC shift (Figure 3.18). The YSWC in Exp. f passed a depth of 80 m at 39.4, 45.3 and 52.3 hours after 0000 UTC 1 March 2013 at latitudes 35.5° N, 35° N and 34.5° N, respectively. It is worth noting that the westward shift of the YSWC occurred two days after the wind burst. The propagation speed of the shift from 35.5° N to 34.5° N was approximately 2.40 $\mathrm{m\,s^{-1}}$. These results are comparable to those from the simplified model experiments and the analytical model (Figure 3.5b, Table 3.2). The westward shift also occurred in Exp. g at 32.5, 44.0 and 59.5 hours at latitudes 35.5° N, 35° N and 34.5° N, respectively. The propagation speed was approximately 1.14 $\mathrm{m\,s^{-1}}$, which is also consistent with the results of Exp. f and the analytical model (Figure 3.5b). A Hovmöller diagram of the SSH anomaly along the 80-m isobath line in Exp. f (Figure 3.19a) shows the propagation of the SSH with the phase speed of the Kelvin waves (17.21 $\mathrm{m\,s^{-1}}$) on the eastern slope (points A–B). It propagated at the speed of the first mode CSW (1.13 $\mathrm{m\,s^{-1}}$) on the western slope (points B–C). These results are consistent with those from Exps. a, b and d. The Hovmöller diagram of the SSH anomaly in Exp. g (Figure 3.19b) also shows a similar propagation pattern.

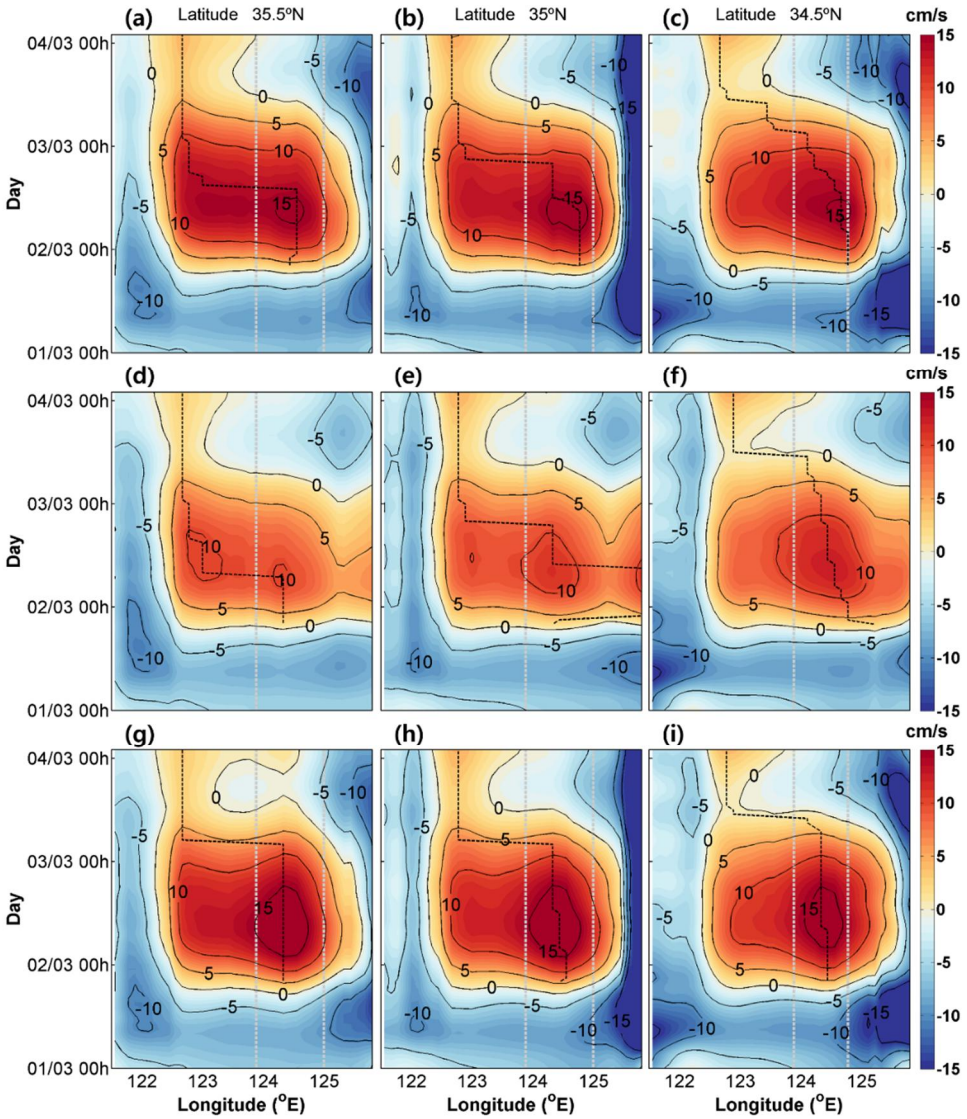

Figure 3. 18 Hovmöller diagrams of the depth-averaged meridional velocity (**cm s^{-1}**, shaded) along (a, d, g) 35.5° N, (b, e, h) 35° N and (c, f, i) 34.5° N in (top) Exp. f, (middle) Exp. g and (bottom) Exp. h. The y-axis represents the time from 1-4 March 2013. Red and blue areas represent the northward and southward velocities, respectively. The black dashed line indicates the position of the maximum meridional upwind velocity. The grey dashed line denotes a depth of 80 m.

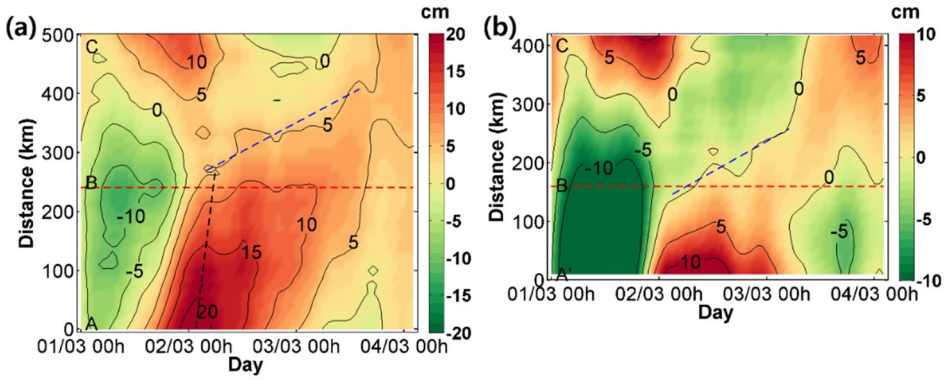

Figure 3. 19 Hovmöller diagrams of the SSH anomaly (cm, shaded) along the 80-m isobath line in (a) Exp. f and (b) Exp. g. The x-axes denote the period from 1-4 March 2013 and the y-axes denote the distance from the point (a) A and (b) A' along the isobath lines in Figures (a) 3.15a and (b) 3.15b. Red dashed lines indicate point B in Figures (a) 3.15a and (b) 3.15b. Red and green areas represent positive and negative SSH anomalies, respectively. The black and blue dashed lines in (a) and the blue dashed line in (b) indicate the lines of linear fit along the maximum positive SSH anomaly, contour lines of 5 and 0 cm. The lines denote the propagation of positive SSHs with phase speeds of 17.21, 1.13 and 1.19 $\mathbf{m\,s^{-1}}$. For the black and blue lines in (a) and the blue line in (b), $\boldsymbol{r^2 = 0.89\ (p < 0.01)}$, $\boldsymbol{r^2 = 0.83\ (p < 0.01)}$ and $\boldsymbol{r^2 = 0.88\ (p < 0.01)}$, respectively.

The positive SSH anomaly resulting from the Kelvin waves propagating along the eastern boundary propagated from the northern (points A' -B) to the western slope (points B-C) with at 1.19 $\mathbf{m\,s^{-1}}$. The experiment without the eastern slope (Exp. g) showed that CSWs driving the westward shift of the YSWC appeared regardless of the presence/absence of an eastern slope.

The propagation of the positive anomaly on the western slope resulted in the westward shift of the YSWC in each experiment. The horizontal distribution of SSH and Hovmöller diagrams further suggest that some of the energy of Kelvin waves scatters into CSWs, driving the westward shift on the northern slope, and the remaining energy continues propagating along the boundary of the YS. The numerical model results with realistic topographies also suggest that CSWs driving the westward shift of the YSWC are generated by the scattering of Kelvin waves on the northern slope. Numerical model results without a northern slope should show that the YSWC does not shift to the west due to the absence of the CSWs. Qu et al. (2018) proposed that the westward shift of the YSWC could not appear without the northern slope providing a wave guide for CSWs between the eastern and western shelves. However, the YSWC in Exp. h shifted to the west of the trough approximately 53–60 hours after the onset time and concurrently at all latitudes (Figures 3.18g–i). An upwind flow occurred in the region where the depth–averaged wind stress was the weakest (Csanady, 1982; Lin and Yang, 2011). If the wind stress in the western region of the trough is weaker than in the trough, upwind flow may develop in the region of weak wind stress. Figure 3.16b shows the daily mean meridional wind stress divided by the depth on 3 March 2013. In the

west, the northward wind stress may be another reason for the shift of the YSWC in the real ocean.

3.4. Conclusion

Three-dimensional numerical models were used to investigate the generation of CSWs which drives the westward shift of the YSWC. The model experiments with simplified topographies showed the formation of the upwind (poleward) flow one day after a northerly wind burst, and its shift to the west after two days. The westward shift of the upwind flow propagated equatorward from north to south at 2.99 $\mathrm{m\,s^{-1}}$, which corresponded to the phase speed of the first mode CSW estimated by the analytical model in the YS.

A positive SSH anomaly driven by the northerly wind propagated poleward along the eastern boundary with the speed of barotropic (external) Kelvin waves. The CSWs that developed on the northern slope due to the scattering of Kelvin waves were the main factors driving the westward shift of the YSWC. The CSWs generated from the eastern slope may also contribute to the shift, despite energy decay due to long propagation distance. Model experiments with realistic topographies confirmed that CSWs propagating equatorward from the northern slope induced the

westward shift of the YSWC. Topographic features, such as the Shandong Peninsula, and spatially different wind stresses may affect the path of the YSWC. The roles of CSWs under stratified conditions and/or with spatially variable wind stress on the westward shift of the YSWC should be further investigated in the future.

4. Contribution of the YSWC to nitrate flux in the YS based on a 3-D physical-biogeochemical coupled model

4.1. Introduction

Seaweed aquaculture is one of the most important aquaculture industries in the coastal area of the YS during winter (Chengkui, 1984; Park et al., 2018). Sometimes the color of seaweed is changed due to the depletion of nitrate (NO3), which is known as the chlorosis (Kang et al., 2014; NFRDI, 2014; Shim et al., 2014; Kim et al., 2017). NO3 distribution could also affect the distribution and the community of the phytoplankton in the YS (Liu et al., 2015a; Xuan et al., 2011). The Kuroshio Current (KC), the Taiwan Warm Current (TWC), the Changjiang River, and other rivers have been suggested as the sources of NO3 the YS (Lim et al., 2007; Lim et al., 2008; Lim et al., 2011; Liu et al., 2015b; Wei et al., 2016).

The distribution of NO3 which originates from the sources might be affected by currents. The YSWC transports an external water mass from the ECS to the YS. Observations showed the YSWC supplies relatively high NO3 water to the YS (Jin et al., 2013; Liu et al., 2015a). Liu et al. (2015b) implied that the high NO3 may originated from the Kuroshio subsurface water and Changjiang

River estuary. Because the Kuroshio subsurface water played a major role in supplying NO3 to the ECS (Chen, 1996; Guo et al., 2012), NO3 from the water mass might be intruded into the YS by the YSWC during winter. NO3 transported through the Taiwan strait may be closely related with the ecosystem in the YS, because the TWC would transport NO3 to the East China Sea (ECS) in summer (Wei et al., 2016).

The Yellow Sea Bottom Cold Water (YSBCW) is also another major source of NO3 in the YS. Previous studies suggested that the YSBCW would store nutrients through the mineralization of the organic matter produced during spring and summer (Hyun and Kim, 2003; Jang et al., 2013; Wei et al., 2016; Fu et al., 2018). The accumulated nutrients in the YSBCW are supplied to the surface layer through the vertical mixing by wind and cooling in winter. Since the YSBCW originates from vertically well-mixed water mass in the central YS during winter, some part of it may be related with the YSWC (Yang et al., 2014; Zhu et al., 2018).

These previous studies suggest that the YSWC could impact on the ecosystem in the YS all the year round. However, there is no study on contribution of the YSWC to NO3 in the YS. This study aims at (1) evaluating the contributions of each source of the NO3 in the YS and (2) figuring out the contribution of the YSWC on

horizontal distribution of NO3 in the YS using a three-dimensional physical-biogeochemical coupled numerical model.

4.2. Data and Model configuration

The physical-biogeochemical coupled model applied for this study is ROMS. The model domain ranged zonally from 117.5° E to 130.3° E and meridionally from 24.8° N to 41° N including the ECS and YS (Figure 4.1a). Bottom topography data was derived from Kim et al. (2013a). The grid resolution was about 1/30 degree horizontally, and 40 sigma layers vertically. The horizontal advection scheme used third-order upstream advection. The horizontal harmonic mixing scheme and the K-Profile Parameterization scheme were used (Large et al., 1994). For the lateral open boundary, the monthly mean temperature, salinity, sea surface height, and velocity were obtained from the Northwestern Pacific model (Seo et al., 2014). The 6-hourly wind, air temperature, sea level pressure, relative humidity, and 12-hourly solar radiation were obtained from the ERA5 reanalysis data of the European Centre for Medium-Range Weather Forecasts as the surface forcing (Copernicus Climate Change Service, 2017). The surface heat flux was calculated using bulk formulae (Fairall et al.,

1996). Tidal forcing of 10 tidal components obtained from TPXO6 was imposed at the lateral boundaries (Egbert and Erofeeva, 2002). Monthly mean river discharges were used in the model including 12 rivers in the Bohai Sea and the YS. The freshwater discharge from the Changjiang River was observed at the Datong station. The discharge data for Han and Geum rivers along the eastern coast of the YS were derived from the National Institute of Environmental Research (NIER), Korea. The discharge data for the other rivers along the Chinese and Korean coasts were obtained from the Global River Discharge Database (Vörösmarty et al., 1996) and Wang et al. (2008). The initial temperature and salinity for an experiment were obtained from the National Ocean Data Center (NODC) World Ocean Atlas 2013 (WOA2013) (Locarnini et al., 2013; Zweng et al., 2013). The initial velocity field was estimated from the geostrophic equation.

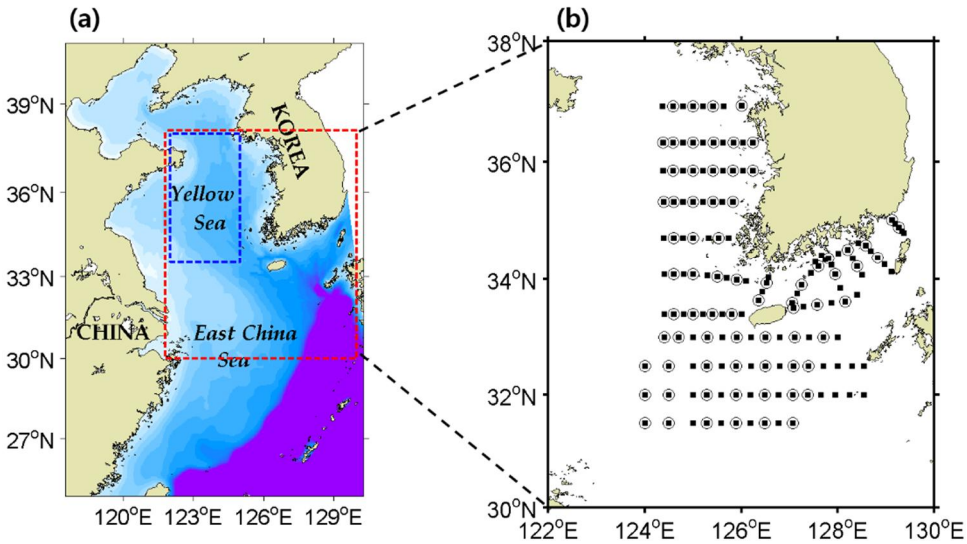

Figure 4. 1 (a) A model domain and (b) stations of observed data obtained from the National Institute of Fisheries Science (NIFS). Stations for temperature, salinity are denoted by filled squares and stations for NO3 are denoted by circles, respectively.

Previous studies have proposed the large seasonal variation in nutrients in the YS (Wang et al., 2003; Jin et al., 2013). They suggested that the YS is not silicate-limited environment, but nitrogen- or phosphorus-limited environment. Especially, in the central and eastern YS, the growth of phytoplankton was potentially limited by nitrogen during the spring bloom. It shows that the biogeochemical model based on the nitrogen cycle is proper to simulate the biogeochemical environment in the YS.

The physical-biogeochemical coupled model is based on the nitrogen cycle described by Fennel et al. (2006). A schematic diagram for the scheme is shown in Figure 4.2. The scheme

includes seven prognostic variables: phytoplankton, chlorophyll, zooplankton, small nitrogen detritus (SDN), and large nitrogen detritus (LDN), nitrate (NO3), ammonium (NH4).

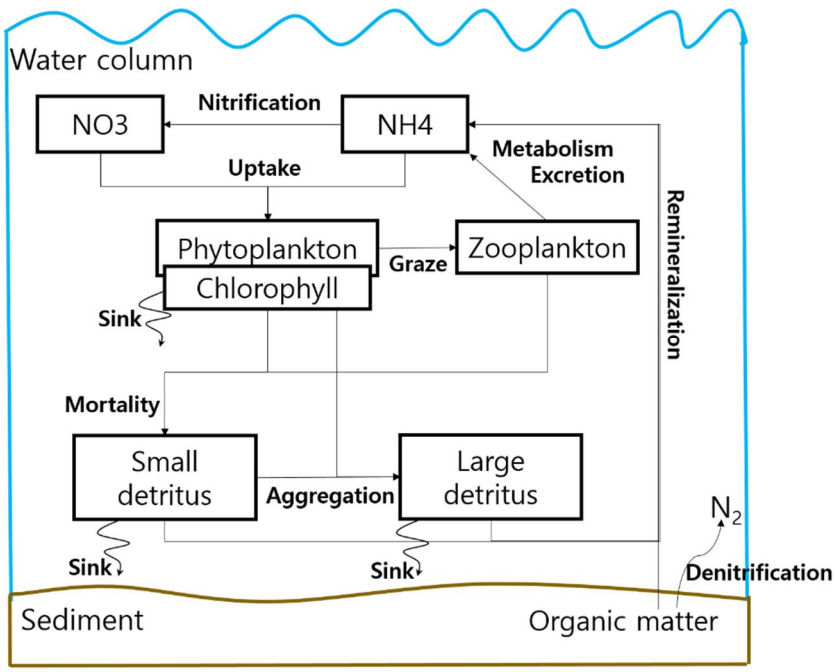

Figure 4. 2 A biogeochemical model schematic diagram for the nitrogen cycle proposed by Fennel et al. (2006).

The growth of phytoplankton depends on the temperature, the photosynthetically available radiation, and nutrients concentration. The radiation is attenuated by water and chlorophyll concentration and the phytoplankton preferentially consumes NH4 and the NO3 uptake is controlled by NH4.

The time rate of phytoplankton change caused by biological sinks and sources is defined by

$$\frac{\partial[Phy]}{\partial t} = \mu[Phy] - g[Zoo] - m_P[Phy] - \tau([SDet] + [Phy])[Phy]$$

$$- w_P \frac{\partial[Phy]}{\partial z}. \qquad (4.1)$$

The growth rate of phytoplankton (μ) is related with the temeperature (T) through the maximum growth rate (μ_{max}), the photosynthetically available radiation (I), and the nutrient concentrations NO3 and NH4,

$$\mu_{max} = \mu_0 \cdot 1.066^T, \qquad (4.2)$$

$$\mu = \mu_{max} \cdot f(I) \cdot (L_{NO3} + L_{NH4}), \qquad (4.3)$$

$$L_{NH4} = \frac{[NH4]}{k_{NH4} + [NH4]}, \qquad (4.4)$$

$$L_{NO3} = \frac{[NO3]}{k_{NO3} + [NO3]} \cdot \frac{1}{1 + \frac{[NH4]}{k_{NH4}}}, \qquad (4.5)$$

where L_{NO3}, L_{NH4}, k_{NO3}, and k_{NH4} are nutrients limiations and the half-saturation concentrations for upatke of NO3 and NH4, respectively. NO3, NH4 uptakes rate. The nutrient limitation is estimated by the Michealis-Menten equations for NO3 and NH4. NO3 uptake is calculated to be inhibited by NH4 through the factor $1/(1 + [\mathrm{NH4}]/k_{NH4})$.

I decreases exponentially with the depth of water colume (z) according to

$$I = I(z) = I_s \cdot PARfrac \cdot exp\left\{-z\left(K_w + K_{chl}\int_z^0 Chl(\zeta)d\zeta\right)\right\}, \quad (4.6)$$

where I_s, $PARfrac$, K_w, and K_{chl} are the shortwave radiation flux,

the fraction of light, the light attenuation coefficients for water and chlorophyll, respectively. The photosynthesis−light (P−I) relationship ($f(I)$) are defined as,

$$f(I) = \frac{\alpha I}{\sqrt{\mu_{max}{}^2 + \alpha^2 I^2}}, \tag{4.7}$$

where α is the initial slope.

The phytoplankton grazing rate by zooplankton (g) is estimated by the Holling−type curve as,

$$g = g_{max} \frac{[Phy]^2}{k_P + [Phy]^2}, \tag{4.8}$$

where g_{max} and k_P are the maximum grazing rate and half−saturation for phytoplankton ingestion. Phytoplankton loss terms are mortality (m_P), aggregation of small detritus and phytoplankton to large detritus, and vertical sinking. Aggregation of phytoplankton and small detritus resulting in large detritus was assumed in this study. The aggregation rate is evaluated with the square of abundance of small particle and multiplied by the aggregation factor (τ). Vertical sinking loss term is presented by multiplying the vertical gradient of concentration of phytoplankton and a constant sinking velocity (w_P).

The time rate of zooplankton change caused by biological sinks and sources is defined as:

$$\frac{\partial[Zoo]}{\partial t} = g\beta[Zoo] - l_{BM}[Zoo] - l_E \frac{[Phy]^2}{k_P + [Phy]^2}\beta[Zoo] - m_z[Zoo]^2, \quad (4.9)$$

where β is the efficiency while the remaining fraction is being transferred to the small detritus pool. Zooplankton loss is evaluated by excretion and mortality. l_{BM}, l_E, and m_z are the basal metabolism, assimilation rate, and zooplankton mortality, respectively.

The time rates of the detrital pools are defined as:

$$\frac{\partial[SDet]}{\partial t} = g(1-\beta)[Zoo] + m_Z[Zoo]^2 + m_P[Phy] - \tau([SDet] + [Phy])[SDet] - r_{SD}[SDet] - w_s\frac{\partial[SDet]}{\partial z}, \quad (4.10)$$

$$\frac{\partial[LDet]}{\partial t} = \tau([SDet] + [Phy])^2 - r_{LD}[LDet] - w_L\frac{\partial[LDet]}{\partial z}, \quad (4.11)$$

where r_{SD}, r_{LD}, w_S, and w_L are the remineralization rates, sinking velocities for the small, large detritus pools, respectively. The remineralization transfers detritus into the NH4, and NH4 is progressively transferred into the NO3 pool due to the nitrification.

The nitrification rate (L_{nitri}) is assumed by

$$L_{nitri} = n_{max}\left(1 - max\left[0, \frac{I - I_0}{k_I + I - I_0}\right]\right), \quad (4.12)$$

where n_{max}, k_I, and I_0 are the maximum rate of nitrification, half-saturation for light inhibition, and inhibition threshold.

The time rates of change for NO3 and NH4 through biological processes are defined as:

$$\frac{\partial[NO3]}{\partial t} = -\mu_{max} f(I) L_{NO3}[Phy] + n[NH4], \quad (4.13)$$

$$\frac{\partial[NH4]}{\partial t} = -\mu_{max} f(I) L_{NH4}[Phy] - nNH4 + l_{BM}[Zoo] + l_E \frac{[Phy]^2}{k_P + [Phy]^2} \beta \cdot [Zoo] + r_{SD}[SDet] + r_{LD}[LDet]. \quad (4.14)$$

The model parameters are listed in Table 4.1 in comparison with parameters from previous studies.

Nutrients are supplied from terrestrial run-off and the deep water by vertical mixing, upwelling, diffusion, or advection. NO3 is also supplied biologically from nitrification and NH4 results from the remineralization. The remineralization does not only occur in the water column, but also the sediment. The model assumes that the decomposition of organic matter occurs completely when it reaches the bottom based on the previous study that approximately 90% of the organic matters derived from the primary production was mineralized in the water column in the YS (Song et al., 2016). All parameters applied in this model are noted in Table 4.1.

Table 4. 1 Biogeochemical Model Parameters

Description	Symbol	Value	Units
Phytoplankton growth rate at 0 ℃	μ_0	0.59[a]	d^{-1}
Light attenuation due to seawater	K_{water}	0.09[b]	m^{-1}
Light attenuation by chlorophyll	K_{Chla}	0.0249[c]	$(mg\ Chl)^{-1}\ m^{-2}$
Initial slope of the P-I curve	α	0.03[d]	$mgC\ gChl^{-1}\ (W\ m^{-2})^{-1}\ d^{-1}$

Maximum chlorophyll to phytoplankton ratio	θ_{max}	0.0535[d]	$mgChl\ mgC^{-1}$
Half-saturation for phytoplankton NO_3 uptake	k_{NO3}	0.33[e]	$mmol\ N\ m^{-3}$
Half-saturation for phytoplankton NH_4 uptake	k_{NH4}	0.1[e]	$mmol\ N\ m^{-3}$
Phytoplankton mortality rate	m_p	0.1[f]	d^{-1}
Zooplankton maximum grazing rate	g_{max}	0.9[a]	$(mmol\ N\ m^{-3})^{-1}\ d^{-1}$
Zooplankton assimilation efficiency for nitrogen	β	0.75[g]	dimensionless
Zooplankton half-saturation constant for ingestion	k_p	2[e]	$(mmol\ N\ m^{-3})^2$
Zooplankton-basal metabolism	l_{BM}	0.1[g]	d^{-1}
Zooplankton-specific excretion rate	l_E	0.1[g]	d^{-1}
Zooplankton mortality rate	m_Z	0.025[a]	$(mmol\ N\ m^{-3})^{-1}\ d^{-1}$
Small detritus remineralization rate for nitrogen	r_{SD}	0.05[g]	d^{-1}
Large detritus remineralization rate for nitrogen	r_{LD}	0.05[g]	d^{-1}
Aggregation parameter	τ	0.008[e]	$(mmol\ N\ m^{-3})^{-1}\ d^{-1}$
Sinking velocity for small detritus	w_{SDet}	0.009[e, h]	$m\ d^{-1}$
Sinking velocity for large detritus	w_{LDet}	0.35[e, h]	$m\ d^{-1}$
Sinking velocity for Phytoplankton	w_{Phy}	0.17[e, h]	$m\ d^{-1}$
Maximum nitrification rate	n_{max}	0.1[j]	d^{-1}
Threshold PAR for nitrification inhibition	I_0	0.0095[i]	$W\ m^{-2}$
Half-saturation PAR for nitrification inhibition	k_I	0.036[i]	$W\ m^{-2}$

[a]Fennel et al., 2006; [b]Evans and Parslow, 1985; [c]Kirk, 1983; [d]Geider et al., 1997; [e]Lima and doney, 2004; [f]Taylor et al., 1991; [g]Leonard et al., 1999; [h]Moskilde, 1996; [i]Olson, 1981; [j]Zhou et al., 2017.

The model did not consider the atmospheric deposition. The nutrients input from the atmospheric deposition is less than half than that from the Changjiang Diluted Water (CDW)in the ECS and YS (Kim et al., 2013b; Li et al., 2015).

The initial and lateral boundary conditions of the biological variables were obtained from WOA2013, SeaWiFS and evaluated using an empirical equation. The initial and boundary conditions for the chlorophyll in the water column was evaluated using the climatology monthly mean surface chlorophyll data obtained from SeaWiFS and an empirical model (Morel and Berthon, 1989; Uitz et al., 2006). The initial and boundary concentration of NO3 was derived from the climatological monthly mean WOA2013 data. The concentration of NH4 was set as 1 μmol/L because NH4 is much less than NO3 by the consumption by phytoplankton and nitrification (Garcia et al., 2013). The initial conditions of phytoplankton, zooplankton, large and small detritus were evaluated from the phytoplankton/chlorophyll, zooplankton/chlorophyll, and detritus/phytoplankton ratios of 0.5, 0.2, and 0.35 (Gruber et al., 2006). The climatological yearly mean concentration of the dissolved inorganic nitrogen in the 2000s and the NO3/NH4 ratio

for the Changjiang River were applied in the model (Dai et al., 2011; Wang et al., 2011; Zhou et al., 2017). For the Yellow River, the concentration of NO3 and NH4 for 2002–2004 was derived from Gong et al. (2015) and its yearly mean concentration was used in the model. The monthly mean riverine NO3 and NH3 from the Korean peninsula were obtained from NIER.

One of the effective analyses to find out and quantify the sources of NO3 in the YS is to exclude NO3 from influential sources such as the Kuroshio water, Changjiang River, TWC, and run-off in the YS through sensitivity experiments. Table 4.2 presents characteristics of sensitivity experiments. Experiments K, C, T, and R indicate experiments excluding NO3 from the Kuroshio water, Changjiang River, TWC, and run-off in the YS, respectively. Experiment Y is same with the control run except for the initial condition of NO3 set to 0 μmol/L in the YS in order to examine spatial contribution of the YSWC to NO3 distribution. Control run has spun up for three years and each experiment has been integrated from 2001 to 2014 from the last day of the control run.

Table 4. 2 Conditions of each sensitivity experiment

	Characteristic of each experiment
Control	All nitrate inflows near the ECS and YS
Exp. K	NO3 inflows excluding the Kuroshio water
Exp. C	NO3 inflows excluding the Changjiang River
Exp. T	NO3 inflows excluding the Taiwan Warm Current
Exp. R	NO3 inflows excluding rivers in the YS
Exp. Y	Same with the control except for the initial condition of NO3 which is set to 0 μmol/L in the YS

The simulated temperature, salinity and NO3 in the eastern YS were compared with observed data to evaluate the performance of the physical-biogeochemical coupled model. The observed data was obtained from the National Institute of Fisheries Science (NIFS) in the eastern YS bimonthly from 2001 to 2010 and data deviated from the mean by more than one standard deviation was excluded in this study.

4.3. Results and Discussion

4.3.1 Seasonal variations in temperature, salinity, chlorophyll, and NO3 in the YS

To validate the model performance for the physical-

biogeochemical process in the YS, simulated temperature, salinity, and NO3 concentration are compared with observed data in February and August. Comparison between the observation and model is examined with climatological mean dataset by averaging each data from 2001 to 2010 in order for the model to simulate seasonal variation in the YS. Figures 4.3, 4.4, and 4.5 show horizontal distributions of temperature, salinity, and NO3 for the climatological observation and control run at surface layer and 50 m depth in February and August, respectively.

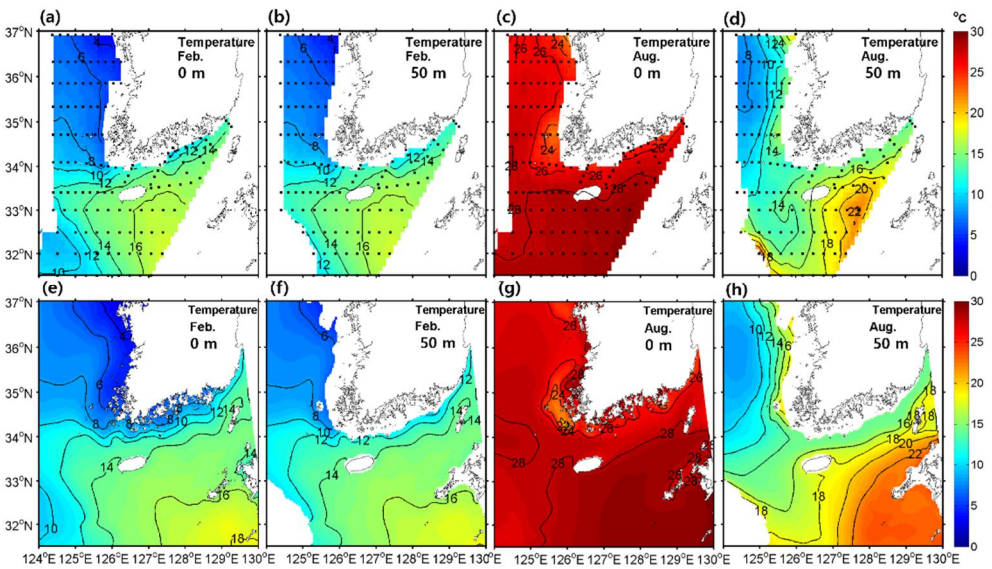

Figure 4. 3 Horizontal distributions of temperature for (upper) the observation and (lower) model at (a, c, e, g) the surface layer and (b, d, f, h) 50 m depth in (a, b, e, f) February and (c, d, g, h) August.

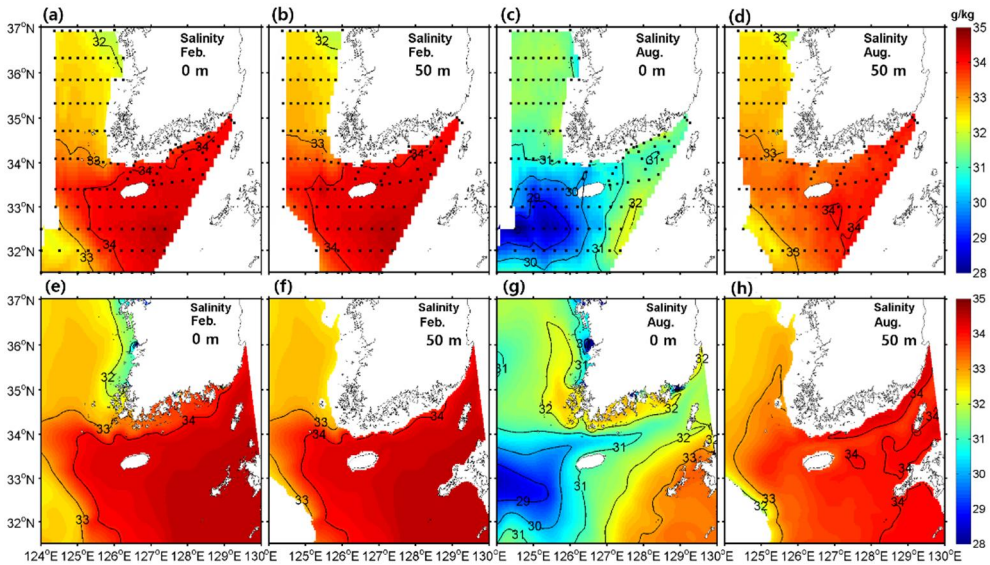

Figure 4. 4 Horizontal distributions of salinity for (upper) the observation and (lower) model at (a, c, e, g) the surface layer and (b, d, f, h) 50 m depth in (a, b, e, f) February and (c, d, g, h) August.

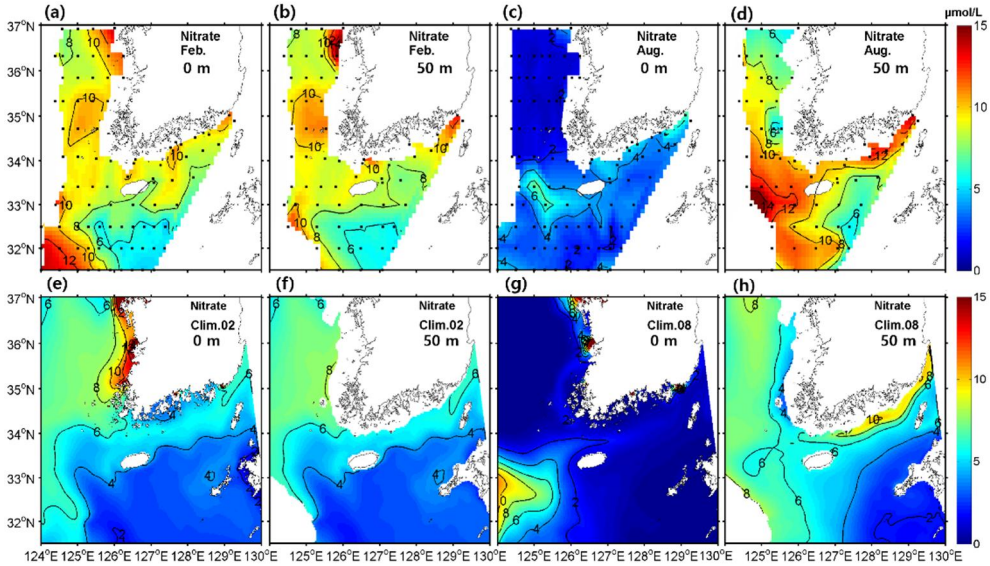

Figure 4. 5 Horizontal distributions of NO3 for (upper) the observation and (lower) model at (a, c, e, g) the surface layer and (b, d, f, h) 50 m depth in (a, b, e, f) February and (c, d, g, h) August.

In February, horizontal distributions at surface layer are the same with those at 50 m depth due to the strong vertical mixing. A

warm, saline, and low NO3 tongue appears on the eastern entrance of the YS. This tongue is well consistent with the observation. The concentration of NO3 is high in the eastern YS and the southwestern area of the Jeju island. The low NO3 water appears with the warm tongue. Although simulated NO3 concentration is lower by 4–5 μmol/L than the observed data, a pattern of the distribution is similar with the observation.

In August, surface temperature increases over 28℃ and relatively low temperature patches occur along western coast of the Korean peninsula due to the tidal mixing. The YSBCW appears in the central YS at 50 m depth. Salinity has different patterns from temperature. The low salinity patch, which is lower than 31 g/kg, appears near the Jeju island especially at the southwestern region of the island because of the CDW. NO3 is transported with the CDW in the surface layer, but the effect is limited to the west of the Jeju island. At 50 m depth, high NO3 water exists with the YSBCW in the YS but low NO3 water is located at southeastern region of the Jeju island due to the effect of the Kuroshio water. These seasonal features for temperature, salinity, and NO3 are distinctly simulated in the coupled model although the absolute value of NO3 concentration is lower by 4–5 μmol/L than that from the observed data.

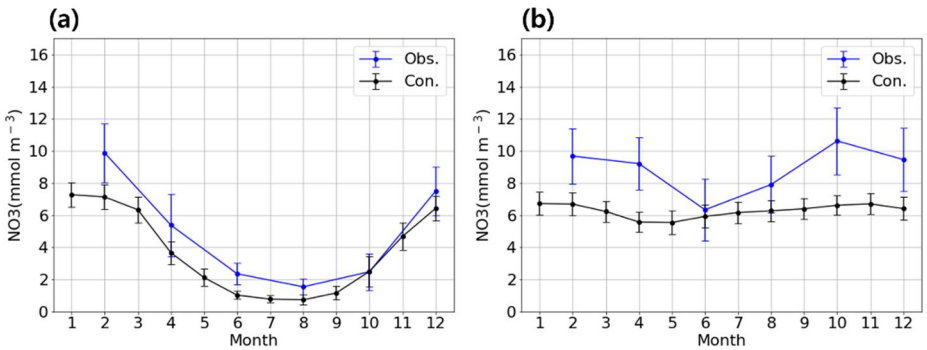

Figure 4. 6 Climatological monthly mean time series of NO3 for (a blue line) the observation and (a black line) model at (a) the surface layer and (b) 50 m depth averaged for NIFS observation stations. Vertical bars represent the mean plus minus a standard deviation.

Climatological monthly mean time series of NO3 for the model is also compared with the observation (Figure 4.6). A large seasonal variation in NO3 concentration at the surface layer because of the consumption by the phytoplankton in spring and the supply by the vertical mixing in winter. The seasonal variation at 50 m depth has also been influenced by the spring bloom and vertical mixing. But the impacts are limited by the stratification. There is a distinct increase of NO3 concentration from June to October, which may be related with the biological activity such as the remineralization and nitrification. Model results have similar features with the observation. The simulated NO3 concentration at the surface layer is nearly consistent with the observation, but the concentration at 50 m depth is lower by 1–4 μmol/L than the

observed data, especially in fall. The difference might be caused by the limitation of input data for organic matters and nutrients from lateral boundary and rivers.

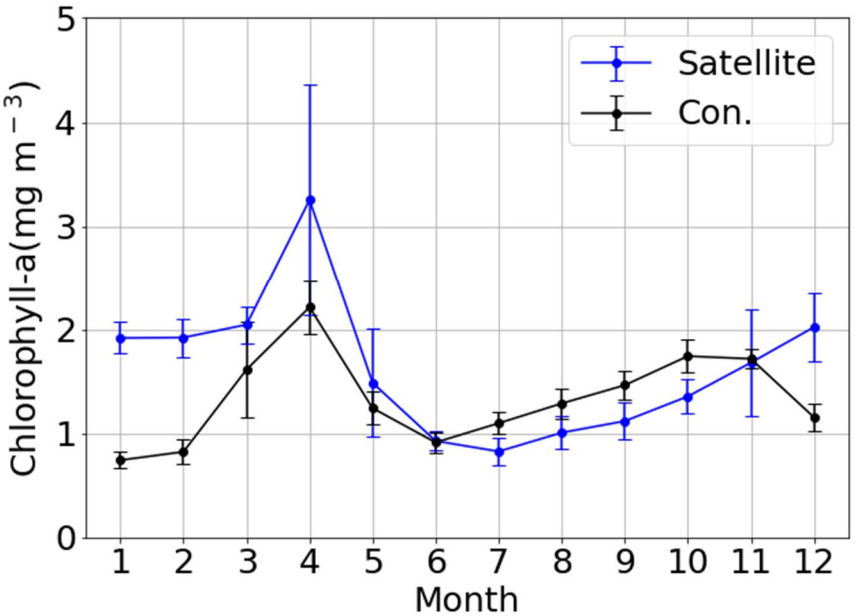

Figure 4. 7 Climatological monthly mean time series of chlorophyll for the (a blue line) satellite data and (a black line) model averaged over the central YS (a blue dashed box in Figure 4.1a). Vertical bars indicate the mean plus minus a standard deviation.

Chlorophyll concentration is one of the important variables to evaluate the coupled model performance. The satellite data from SeaWiFS from 2001 to 2002 and MODIS aqua from 2003 to 2010 which are climatologically monthly averaged, were compared with simulated chlorophyll from the model. Time series of the climatological monthly mean chlorophyll concentration from the

satellite data and the model is displayed in Figure 4.7. The spring bloom is distinctly simulated in the model. Its absolute value is included within one standard deviation from the mean of the satellite data. However, the fall bloom occurs only in the model. Chlorophyll concentration observed the satellite during winter season are higher than those during fall season. Tan and Shi (2012) presented the distinct spring and fall blooms using the primary production derived from the SeaWiFS data and the seasonal variation in the primary production. The reason for the abnormal high chlorophyll concentration from the satellite data during winter might result from the particle resuspension by the strong vertical mixing.

4.3.2 NO3 fluxes in the ECS

Calculation of NO3 fluxes by various paths in the ECS is essential to validate the model performance. Figure 4.8 shows the annual mean schematic diagram and monthly mean time series of the NO3 fluxes through the major sections and the Changjiang River. NO3 flows into the ECS from the KC, TWC, the YS, and the Changjiang River and flows out through the Korea Strait. The schematic diagram shows that the KC is a main source, which has already suggested by previous papers (Chen, 1996; Guo et al.,

2012). The Changjiang River and TWC are minor sources. NO3 flux from the YS is comparable with run-off from rivers in the YS and it is an order of magnitude lower than the others. 80% of the total inflow of NO3 into the ECS runs out through the Korea Strait by the TsWC. Annual mean NO3 fluxes in Figure 4.8a are comparable to the fluxes estimated by previous studies (Chung et al., 2000; Kim et al., 2013b).

Monthly mean NO3 fluxes are also estimated (Figure 4.8b). NO3 through the KC flows mainly in summer and winter. The maximum flux is approximately 0.4 Tmol/year in July and the minimum is under 0.2 Tmol/year in February. The flux through the TWC is maximum of 0.2 Tmol/year, in January and lower than 0.06Tmol/year in late spring. Seasonal variation in NO3 fluxes by the KC and TWC estimated from the model results are comparable to the box model result and the observation (Chung et al., 2001; Zhang et al., 2007). NO3 flux from the Changjiang River has a distinct seasonal variation depending on the river discharge which is maximum in summer due to the precipitation.

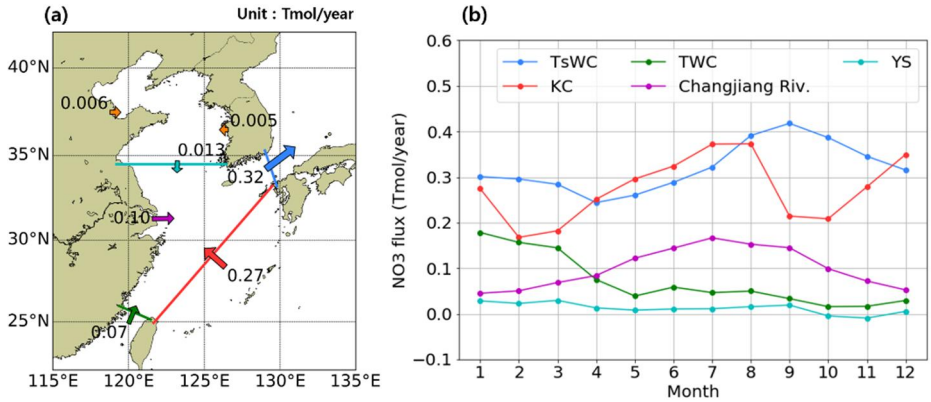

Figure 4. 8 (a) A schematic diagram for annual mean NO3 fluxes (Tmol/year) in the ECS through (a blue arrow) the TsWC, (a red arrow) KC, (a green arrow) TWC, (a cyan arrow) currents in the YS (YS), (a purple arrow) Changjiang River, and (orange arrows) run-off of rivers in the YS and Bohai Sea. Numbers near the arrows indicate annual mean NO3 fluxes from the climatological model result. (b) Climatological monthly mean time series of NO3 fluxes through (a blue line) the TsWC, (a red line) KC, (a green line) TWC, (a cyan line) currents in the YS (YS), and (a purple line) Changjiang River.

4.3.3 Water mass analysis to figure out the sources of NO3

Temperature and Salinity (TS) diagram analysis was performed by using the observed data to trace out each source of NO3 in the YS (Figure 4.9). The diagrams show that there are two high NO3 water masses. One is the YSBCW whose temperature is less than 10℃ and salinity ranges from 32 to 33 g/kg. The other is the

Tsushima Middle Water (TsMW) which originates from the Kuroshio subsurface water. The temperature and the salinity of the TsMW range from 14 to 17℃ and from 34.30 to 34.60 g/kg (Kwan, 1963; Park, 1978; Kim and Kim, 1983; Hur et al., 1999; Park et al., 2011; Yang et al., 2014). These two water masses have similar density between 1,025 kg/m^3 and 1,026 kg/m^3. Spiciness is an effective method to classify water masses with similar density. Spiciness of the YSBCW in winter is lower than −2 and the spiciness in summer is nearby −1. Spiciness of the TsMW is approximately 2 all year round. In general, spiciness of high NO3 water is presented under 0 close to the YSBCW. It suggests that most of the water mass with high NO3 near the Korean peninsula is mainly mixed with the YSBCW.

The TsMW denoted by triangles in Figure 4.9 is not observed in the YS, but only at the entrance of the YS. Although the water mass is not directly transported into the YS, it may indirectly affect NO3 distribution in the YS since the YSWC intrudes a mixed water mass in the ECS into the YS. The diagrams also suggest that the YSBCW would be a main source of NO3 in the YS. The YSBCW is isolated by the stratification in summer and connected with a water mass in the ECS by the YSWC in winter. It implies that the YSBCW may accumulate NO3 through the biological process (e.g.

nitrification) and the intrusion of external water masses in the ECS by the YSWC. Zhu et al. (2018) have suggested that some part of the YSWC intruded along the YS trough could remain and provide nutrients to the YSBCW. The TS diagram analysis with previous study suggest that the NO3 flows in the YS by the YSWC from water masses in the ECS in winter and remains as a part of the YSBCW in summer.

Previous studies suggested that the Changjiang River also is a major source of nutrients. However, NO3 concentration in a low saline water mass was generally low in TS diagrams because the NO3 at the surface is consumed by biological activity during long transport (Kwon et al., 2018). Although it is not clearly shown in the diagrams, run-off in the YS such as the Yellow, Han, and Geum River would also supply NO3 into the YS. However their discharges are much lower than that of the Changjiang River.

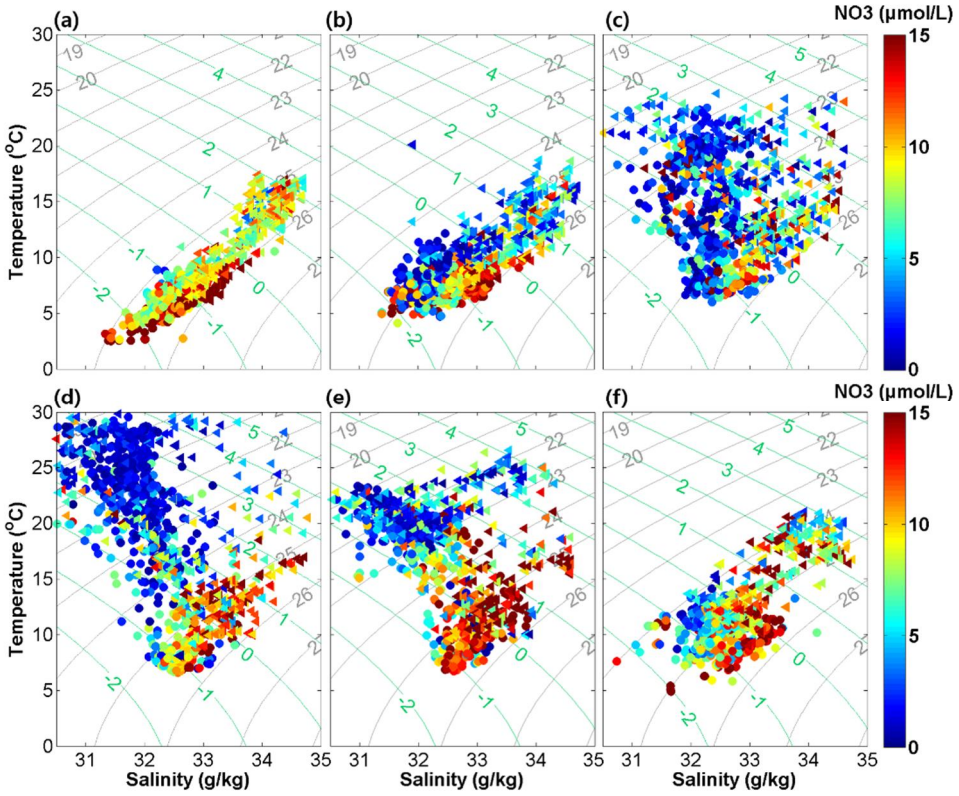

Figure 4. 9 TS diagrams for the observed data from 2001 to 2010 in (a) February, (b) April, (c) June, (d) August, (e) October, and (f) December. Color indicates NO3 concentration. Grey and green lines indicate density and spiciness, respectively. Circles denote stations over 34.5° N in the YS and triangles denote stations between 33° N and 34.5° N in the sea around the Jeju island. The stations are denoted in Figure 4.1b.

4.3.4 Contribution of each origin of NO3 in the YS

Temporal variation in NO3 concentration can be expressed by a following equation:

$$\frac{\partial[NO3]}{\partial t} = (-\vec{u} \cdot \nabla[NO3]) + \left(k_h \nabla^2[NO3]\right)$$

$$+\left(-L_{NO3} \cdot [Phyto]\right) + (L_{nitri} \cdot [NH4]). \quad (4.15)$$

Each term of the right side of the equation (4.15) indicates the advection, diffusion, NO3 uptake in phytoplankton, and nitrification, respectively. Those terms can be classified by the physical and biological factors. The first two terms are caused by the physical process, and the rest terms are related to the biological process. Contributions of the external sources of NO3 supplied by the advection term of the physical process to the YS can be quantified by multiple sensitivity experiments (Table 4.2). Since NO3 can be supplied by nitrification process according to the equation (4.15), a biological source is also estimated.

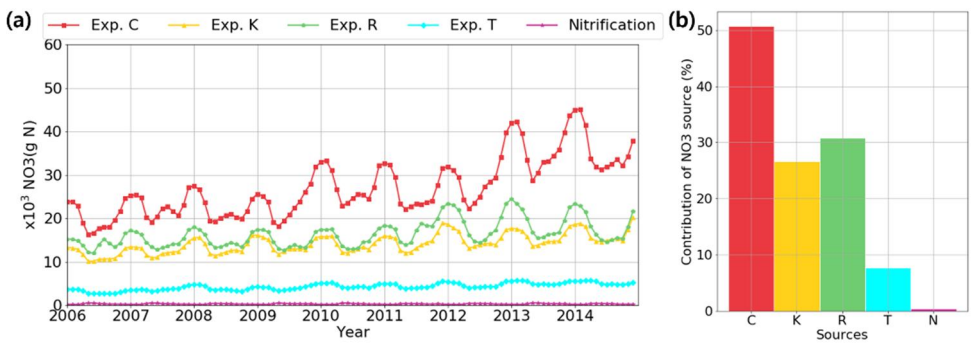

Figure 4. 10 (a) Monthly mean time series of the difference between the mass of NO3 for the control run and each sensitivity experiment in the YS. Colored lines represent the differences of the mass of NO3 for the control run with (red) Exp. C, (yellow) Exp. K, (green) Exp. R, (cyan) Exp. T, and (purple) nitrification. (b)

Annual mean contribution of each source to NO3 in the YS. Colored Bars indicate contribution of (red) the Changjiang River, (yellow) KC, (green) rivers in the YS, (cyan) TWC, and (purple) nitrification to NO3 in the YS, respectively.

Figure 4.10 shows monthly mean time series of the difference between the mass of NO3 in the YS from the control run experiment and each sensitivity experiment, and contribution of each source to NO3 in the YS. The area of the YS for the calculation ranges meridionally from 34.5° N to 38° N and zonally from 119° E to 127° E. Production of NO3 by nitrification is estimated from result of the control run experiment using equations (4.6, 4.12, 4.15). The monthly mean time series was calculated from 2006 to consider spin-up time. The difference represents contribution of each source to NO3 in the YS. The result shows that the Changjiang River is a primary source and the KC and rivers in the YS are secondary sources. The TWC plays the minor role in the contribution. The difference between control run and Exp. C increases greatly in 2009 and 2012, which might result from the abnormal large inflow of the CDW into the YS (Hong et al., 2016).

Quantitative contribution of NO3 from each source is estimated by dividing NO3 of the control run into it for each sensitivity experiment. Figure 4.10b shows annual mean contributions of sources in the YS. Annual mean data of each sensitivity experiment

is averaged from 2006 to 2014. The annual contributions of the Changjiang River, KC, run-off in the YS, TWC, and nitrification are 50.7, 26.6, 30.8, 7.7, and 0.5%, respectively. NO3 from the Changjiang River accounts for a half of total NO3 in the YS. NO3 from the KC and rivers in the YS contribute a quarter of the total NO3, respectively. NO3 from the TWC plays a minor role in the NO3 source to the YS. The production by nitrification process only explains under 1% of the total NO3 in the YS. Total contribution of the sources exceeds 100% because uptake rate of NO3 (equation 4.5) in each experiment is different. It means that total NO3 consumption by phytoplankton from sensitivity experiments exceeds the consumption from control run. The contributions of sources suggest that most NO3 in the YS originates from the advection and the biological process is ineffective for supplying NO3 to the YS.

In order to investigate spatial contributions of NO3 sources in the YS during winter, horizontal distribution of contribution of each source at the surface layer is presented in Figure 4.11. The distributions at the bottom layer are nearly same with those at the surface layer due to strong vertical mixing (not shown). Figure 4.11 shows that NO3 from the Changjiang River contributes over 80% of NO3 in the western YS and a half of it in the central sea. NO3 from

the KC mainly explains the eastern entrance of the YS and plays a secondary role in NO3 in the central YS as contributing 20 to 40% of the NO3. The TWC rarely have an influence on the YS as accounting for under 20% of the NO3. More than 80% of NO3 in the east coast of the YS originates from the rivers in the YS and over a half of NO3 near the Shandong peninsula originates from the rivers in the YS. Figure 4. 11 presents that external sources mainly contribute to the western and central region, whereas local river source contributes to the east coast.

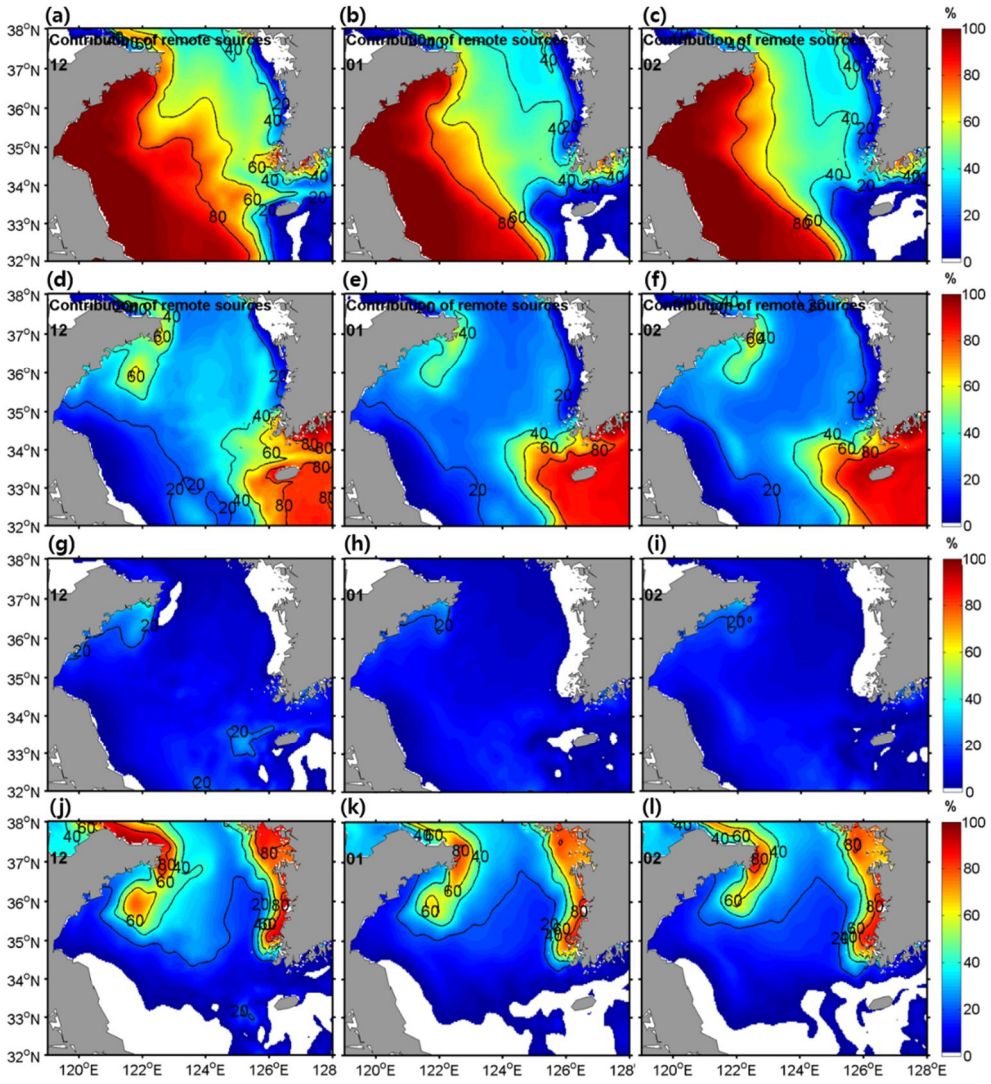

Figure 4. 11 Horizontal distributions of contributions of NO3 sources from (a, b, c) the Changjiang River, (d, e, f) KC, (g, h, i) TWC, and (j, k, l) rivers in the YS at the surface layer in (left) December, (middle) January, and (right) February.

4.3.5 Estimation of NO3 flux by the YSWC

Previous studies have suggested that the YSWC could supply NO3 to the YS. The intruded high NO3 water by YSWC may impact the ecosystem as a part of the YSBCW in spring and summer. It is obvious that the YSWC supplies NO3 during winter. However, there has been no study on quantifying NO3 supplied to the YS through the YSWC. The northwesterly wind generates an upwind flow known as the YSWC in the central region of the YS and two downwind coastal flows along the eastern and western coast during winter (Lie et al., 2001; Lin et al., 2011; Tak et al., 2016). To estimate contribution of the YSWC to NO3 in the YS, vertical sections of NO3, meridional velocity, and NO3 flux in the YS are examined.

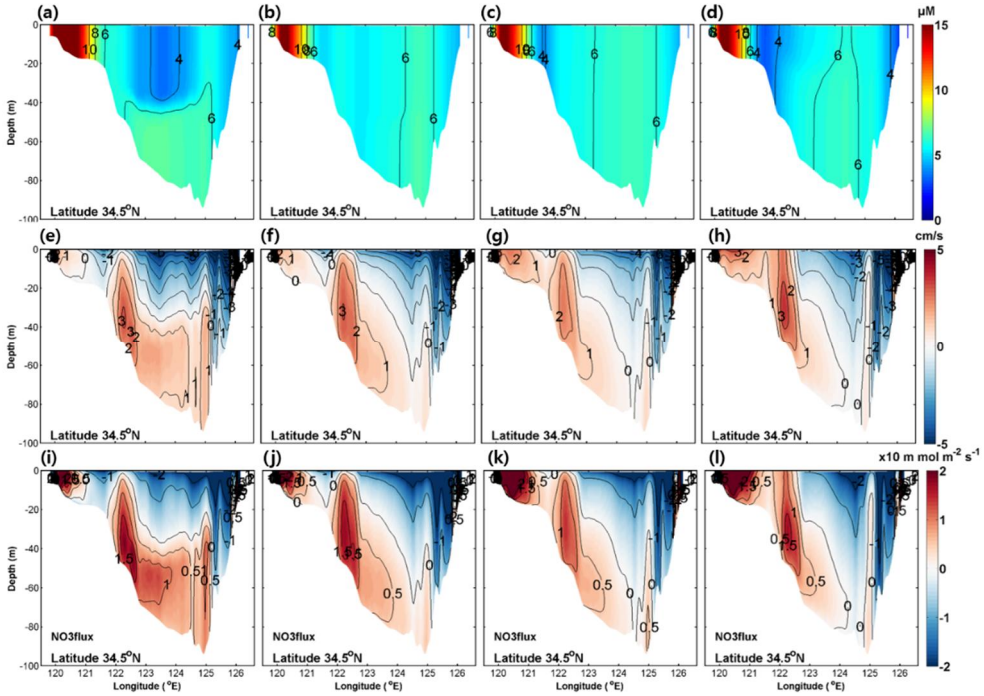

Figure 4. 12 Vertical sections of (upper) NO3, (middle) meridional velocity, and (lower) NO3 flux across the 34.5° N section in (a, e, i) December, (b, f, j) January, (c, g, k) February, and (d, h, l) March. Rainbow color in upper panels indicates concentration of NO3 (unit : μmol/L) across the section and red, blue indicate northward, southward velocities (unit : cm/s) and NO3 fluxes (unit : $\times$ 10 mmol/m^2s) in middle and lower panels, respectively.

Vertical sections of NO3, meridional velocity, and NO3 flux into the YS across the 34.5° N during winter are shown in Figure 4.12. The NO3 in December is relatively high in the bottom layer of the trough where the YSWC flows. However, the NO3 is vertically homogeneous by strong vertical mixing during the whole period except for December. Northward flow on the western flank of the trough, which indicates the existence of the YSWC from December

to March. NO3 flux during the period was estimated using NO3 concentration and the meridional velocity. The spatial pattern of NO3 flux is comparable with it of the meridional velocity. This means that the high NO3 flux on the western flank of the trough is closely related with the path of the YSWC.

To quantify the horizontal NO3 flux by the YSWC, monthly mean horizontal NO3 flux into the YS across the 34.5° N section was estimated (Figure 4.13). Dashed and solid lines indicate NO3 fluxes into the YS across the whole section and the trough between 121.6° E and 125.5° E which is the main path of the YSWC. The solid line represents the NO3 flux into the YS by the YSWC during winter. Two black lines show time series of the NO3 fluxes from the control run. During winter, the NO3 flux through the trough (a black dashed line) is similar to the NO3 flux through the whole section (a black solid line) which represents the NO3 flux by the YSWC in winter. Total NO3 inflow across the whole section is 0.507 Tg N and a NO3 inflow by the YSWC from December to March is 0.137 Tg N, which accounts for 27% of the total inflow. Total mass of NO3 in the YS ranging zonally from 119° E to 127° E and meridionally from 34.5° N to 38° N is normally 0.735 Tg N during winter (Figure 4.13b). It suggests that the NO3 inflow by the YSWC contributes about 20% of the mass of NO3 in the YS during winter.

The NO3 inflow originating from the Changjiang River plays a primary role in the inflow by the YSWC. Those from the KC, TWC are secondary factors. Figure 4.13c quantitatively shows winter mean contribution of NO3 inflow from each source by the YSWC. The Changjiang River is a main source of the NO3 inflow by the YSWC contributing 64% of the inflow. The NO3 flux from the KC, TWC accounts for 29%, 10% of the total flux, respectively.

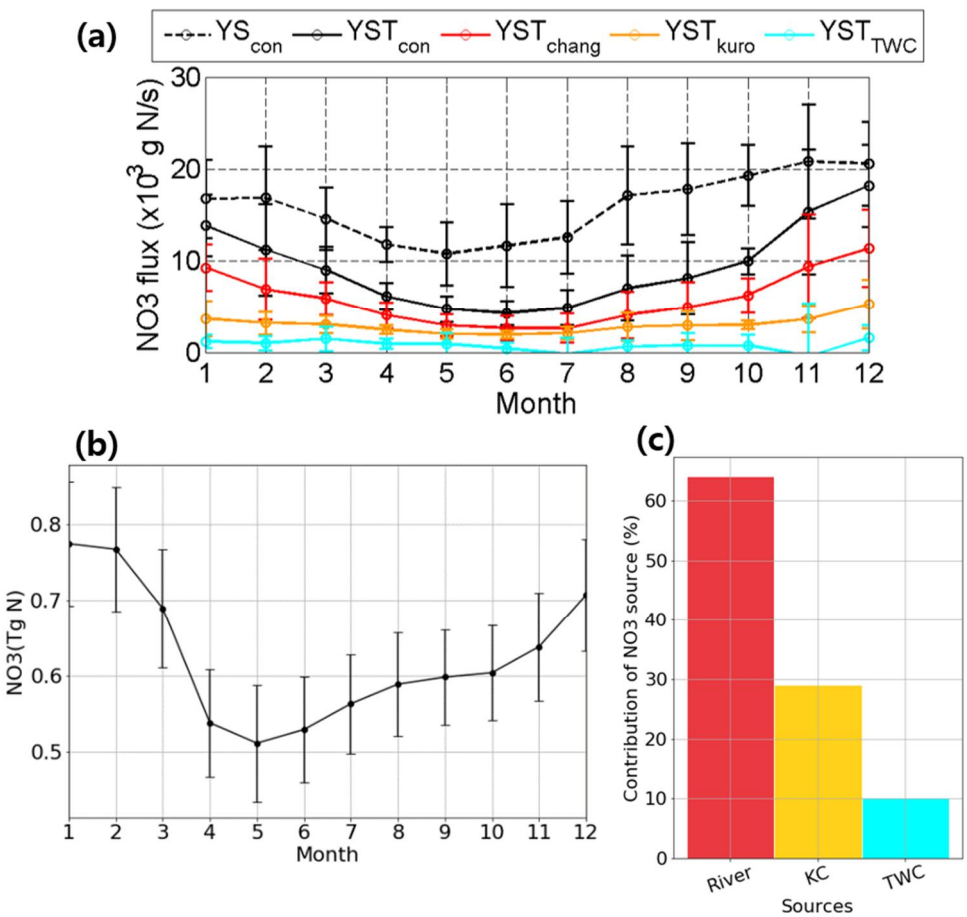

Figure 4. 13 (a) Monthly mean time series of NO3 flux into the YS across the 34.5° N section. A black dashed line denotes NO3 flux

across the whole section from the control run. Black, red, orange, cyan lines denote NO3 flux across the section between 121.6° E and 125.5° E originating from all sources, the Changjiang River, KC, and TWC, respectively. Vertical bars indicate the mean plus minus a standard deviation. (b) Monthly mean time series of the mass of NO3 in the YS which ranges zonally from 119° E to 127° E and meridionally from 34.5° N to 38° N. (c) Winter mean contributions of NO3 fluxes by the YSWC originating from (red) the Changjiang River, (orange) KC, and (cyan) TWC, respectively.

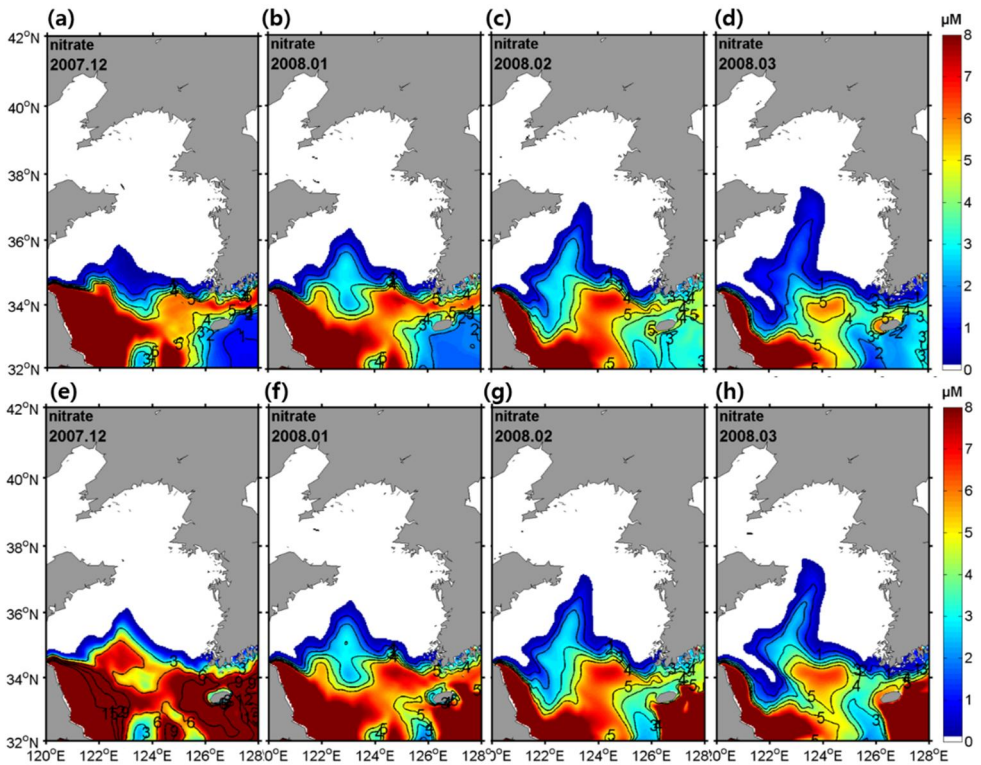

Figure 4. 14 Horizontal distributions of NO3 at (upper) the surface and (lower) bottom layers from Exp. Y in (a, e) December, (b, f) January, (c, g) February, and (d, h) March. Color map denotes concentration of NO3 (unit : μmol/L).

In order to evaluate spatial contribution of the YSWC to NO3 distribution in the YS, a sensitivity experiment (Exp. Y) was performed. Exp. Y is same with the control run except for the initial condition of concentration of NO3 which is set to 0 μmol/L in the YS. The experiment has been simulated from 1 November of 2007. Figure 4.14 shows monthly mean horizontal distributions of NO3 for Exp. Y in December, January, February, and March. The NO3 spreads northward along the path of the YSWC. During winter, the YSWC could supply NO3 to the sea off the Shandong peninsula. The NO3 transported by the YSWC mainly affects both the surface and the bottom layer in the western region of the YS.

4.3.6 Limitations of this study and future works

The role of the YSWC in the NO3 flux into the YS during winter was investigated based on the nitrogen cycle. However, previous studies reported that the YS has abundant silicate and nitrogen- or phosphorus-limited environment (Wang et al., 2003; Jin et al., 2013). Since the biological module used in this study was based on the nitrogen cycle, it could not consider the effect of phosphorus cycle on the ecosystem of the YS. Although dissolved inorganic nitrogen including NO3 and NH4 would limit phytoplankton growth

during the spring bloom, phosphate also would play an important role in controlling the phytoplankton growth after the bloom (Fu et al., 2009; Jin et al., 2013). Li et al. (2015) have proposed that dissolved inorganic nitrogen and phosphate have increased and decreased from 1980s to 2012, respectively. It implies that the YS may be predominantly transformed to phosphorus-limited environment in future. Thus, the biological module considering the phosphorus cycle would be applied to investigate long-term variation of the contribution of the YSWC in future study.

According to the chapter 3, generation of the YSWC and change in the path of the current occurs within 2 or 3 days after the wind burst, but this study does not investigate the effect of the YSWC on short-scale variation in the NO3 distribution and flux. The short-term variation also should be revealed through further investigation.

4.4. Conclusion

A physical-biogeochemical coupled model experiment was performed to investigate the role of the YSWC in NO3 budget in the YS and quantify contributions of sources to NO3 in the YS. The coupled model simulated well seasonal variation in temperature, salinity, chlorophyll, NO3. The simulated NO3 fluxes through

various currents in the ECS also were comparable with the previous studies. TS diagrams analysis showed that the TsMW and YSBCW were high NO3 water masses nearby the YS. The TsMW originating from the KC might supply to the YS by the YSWC. The YSWC supplies the NO3 to the YSBCW which persists to summer in the lower layer of the YS.

Contributions of each origin of NO3 in the YS were quantified using multiple sensitivity experiments. The NO3 from the Changjiang River explained 51% of NO3 in the YS. The KC and rivers in the YS accounted for about 25% of NO3, respectively. NO3 from the TWC plays the minor role. The production by nitrification process only contributed under 1% of NO3 in the YS. It suggested that the external sources are dominant but the biological process is insignificant. The NO3 from the Changjiang River mainly contributed the western and central region of the YS. That from the KC played a secondary role in the central YS. Local rivers from Korea explained mainly the east coast of the YS.

The NO3 inflow by the YSWC in winter was about 0.14 Tg N, which contributed about 20% of the winter mean mass of NO3 in the YS. The NO3 from the Changjiang River contributed 64% of the inflow. The NO3 from the KC, TWC accounted for 29%, 10% of the inflow, respectively (Figure 4.15).

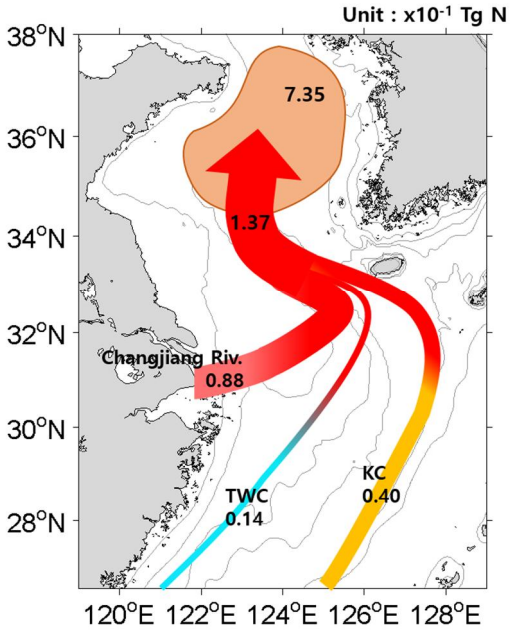

Figure 4. 15 A schematic flow for NO3 flux by the YSWC. A red arrow indicates NO3 inflow by the YSWC and bright red, orange, cyan denote contributions of sources from the Changjiang River, KC, and TWC to the inflow, respectively (unit : $\times 10^{-1}$ Tg N). A brown patch in the YS indicates winter mean mass of NO3 in the YS.

5. Summary and conclusion

Ocean circulation driven by winds and its evolution in the YS were successfully simulated by the ROMS forced by realistic winter atmospheric conditions. Southward current was stronger along the Korean coast than along the Chinese coast at the surface. Monthly mean current from the model simulation showed a clockwise circulation in the subsurface layer in the southern YS. A time-lagged correlation analysis suggested that the downwind flow at the surface responded instantly to variations in northwesterly wind, which prevailed over the entire YS in winter. The surface flow in the upper part of the eastern YS was still influenced by wind variations with a one-day lag and the upwind current in the bottom layer within the trough responded to the wind variations with a one-day lag. After two days, the upwind flow shifted to the west of the trough as the downwind flow along the Korean coast strengthened.

Idealized models were used to investigate the cause of the westward shift in the YSWC. Model experiments with simplified topographies showed the westward shift propagated equatorward from north to south at 2.99 $\mathrm{m\,s^{-1}}$, which corresponded to the phase speed of the first mode CSW estimated by the analytical model. A

positive SSH anomaly driven by the northerly wind generated barotropic Kelvin waves that quickly propagated poleward along the eastern boundary. The CSWs that developed on the northern slope due to the scattering of Kelvin waves were the main factors driving the westward shift of the YSWC, while the CSWs generated from the eastern slope may have also contributed to the shift, despite a long decay distance. Model experiments with realistic topographies confirmed that CSWs propagating equatorward from the northern slope induced the westward shift of the YSWC.

The physical–biogeochemical coupled model was performed to investigate the role of the YSWC in NO3 budget in the YS and quantify contributions of origins of NO3. TS diagrams showed the TsMW and YSBCW were high NO3 water masses nearby the YS. The TsMW originating from the KC might be supplied into the YS by the YSWC and the YSBCW would reserve NO3 by the YSWC. The multiple sensitivity experiments proposed that NO3 from the Changjiang River explained 51% of NO3 in the YS and the KC and run–off in the YS accounted for about 25% of NO3, respectively. NO3 from the TWC plays the minor role. The production by nitrification process only contributed under 1% of NO3 in the YS. It suggested that the external sources were dominantly supplied by currents and the biological process was insignificant for supplying

NO3 to the YS. Spatial contribution of each source proposed that NO3 from the Changjiang River contributed the western and central YS. NO3 from the KC played a secondary role in NO3 in the central YS. Local rivers from Korea contributed mainly the eastern coast of the YS.

The NO3 flux by the YSWC was 0.137 Tg N, which contributed about 20% of the total mass of NO3 in the YS during winter. NO3 from the Changjiang River, KC, and TWC contributed 64%, 29%, and 10% of the inflow by the YSWC, respectively.

References

Adams, J. K., and V. T. Buchwald (1969), The generation of continental shelf waves, J. Fluid Mech., 35, 815–826, doi:https://doi.org/10.1017/S0022112069001455.

Antonov, J. I., S. Levitus, T. P. Boyer, M. E. Conkright, T. O' Brien, and C. Stephens (1998), World Ocean Atlas 1998 Vol. 2: Temperature of the Pacific Ocean, NOAA Atlas NESDIS 28, U.S. Government Printing Office, Washington, D.C.

Beardsley, R. C., R. Limeburner, K. Kim, and J. Candela (1992), Lagrangian flow observations in the East China, Yellow and Japan seas, La Mer, 30(3), 297–314.

Boyer, T. P., S. Levitus, J. I. Antonov, M. E. Conkright, T. O'Brien, and C. Stephens (1998), World Ocean Atlas 1998 Vol. 5: Salinity of the Pacific Ocean, NOAA Atlas NESDIS 31, U.S. Government Printing Office, Washington, D.C.

Brooks, D. A. (1978), Subtidal sea level fluctuations and their relation to atmospheric forcing along the North Carolina coast, J. Phys. Oceanogr., 8, 481–493, doi:https://doi.org/10.1175/1520-0485(1978)008<0481:SSLFAT>2.0.CO;2.

Buchwald, V. T., and J. K. Adams (1968), The propagation of

continental shelf waves, Proc. Roy. Soc. Lond. Ser. A, 305, 235–250, doi:https://doi.org/10.1098/rspa.1968.0115.

Chen, C. T. (1996), The Kuroshio intermediate water is the major source of nutrients on the East China Sea continental shelf, Oceanol. Acta, 19(5), 523–527.

Chengkui, Z. (1984), Phycological research in the development of the Chinese seaweed industry, Hydrobiologia, 116(1), 7–18, doi:https://doi.org/10.1007/BF00027633.

Chung, C.–S., G.–H. Hong, S.–H. Kim, J.–K. Park, Y.–I. Kim, D.–S. Moon, K.–I. Chang, S.–Y. Nam, and Y.–C. Park (2000), Biogeochemical fluxes through the Cheju Strait, J. Korean Soc. Oceanogr., 5(3), 208–215.

Chung, S.–W., S. Jan, and K.–K. Liu (2001), Nutrient fluxes through the Taiwan Strait in Spring and Summer 1999, J. Oceanogr., 57(1), 47–53.

Csanady, G. T. (1976), Topographic waves in Lake Ontario, J. Phys. Oceanogr., 6, 93–103, doi:https://doi.org/10.1175/1520–0485(1976)006<0093:TWILO>2.0.CO;2.

Csanady, G. T. (1982), Circulation in the Coastal Ocean, 1st ed. Springer Netherlands, Dordrecht, pp. 281.

Csanady, G. T. (1997), On the theories that underlie our understanding of continental shelf circulation, J. Oceanogr.,

53, 207–230.

Dai, Z., J. Du, X. Zhang, N. Su, and J. Li (2011), Variation of riverine material loads and environmental consequences on the Changjiang (Yangtze) Estuary in recent decades (1955–2008), Environ. Sci. Technol., 45(1), 223–227,doi:https://doi.org/10.1021/es103026a

Dee, D. P., S. M. Uppala, A. J. Simmons, P. Berrisford, P. Poli, S. Kobayashi, U. Andrae, M. A. Balmaseda, G. Balsamo, P. Bauer, P. Bechtold, A. C. M. Beljaars, L. van de Berg, J. Bidlot, N. Bormann, C. Delsol, R. Dragani, M. Fuentes, A. J. Geer, L. Haimberger, S. B. Healy, H. Hersbach, E. V. Hólm, L. Isaksen, P. Kållberg, M. Köhler, M. Matricardi, A. P. McNally, B. M. Monge-Sanz, J.-J. Morcrette, B.-K. Park, C. Peubey, P. de Rosnay, C. Tavolato, J.-N. Thépaut, and F. Vitart (2011), The ERA-Interim reanalysis: Configuration and performance of the data assimilation system, Q. J. R. Meteorol. Soc., 137(656), 553–597, doi:10.1002/qj.828.

Ding, Y., X. Bao, Z. Yao, D. Song, J. Song, J. Gao, and J. Li (2018), Effect of coastal-trapped waves on the synoptic variations of the Yellow Sea Warm Current during winter, Cont. Shelf Res., 167, 14–31, doi:https://doi.org/10.1016/j.csr.2018.08.003.

Egbert, G. D., and S. Y. Erofeeva (2002), Efficient Inverse Modeling

of Barotropic Ocean Tides, J. Atmos. Oceanic Technol., 19, 183–204, doi:http://dx.doi.org/10.1175/1520-0426(2002)019<0183:EIMOBO>2.0.CO;2.

[dataset]European Centre for Medium-Range Weather Forecasts, ERA-Interim project, Research Data Archive at the National Centre for Atmospheric Research, Computational and Information Systems Laboratory, 2013, accessed, 12 March 2014, doi:https://doi.org/10.5065/D6CR5RD9.

Fairall, C. W., E. F. Bradley, D. P. Rogers, J. B. Edson, and G. S. Young (1996), Bulk parameterization of air–sea fluxes for Tropical Ocean–Global Atmosphere Coupled–Ocean Atmosphere Response Experiment, J. Geophys. Res., 101(C2), 3747–3764, doi:10.1029/95JC03205.

Fennel, K., J. Wilkin, J. Levin, J. Moisan, J. O'Reilly, and D. Haidvogel (2006), Nitrogen cycling in the Middle Atlantic Bight: Results from a three□dimensional model and implications for the North Atlantic nitrogen budget. Glob. Biogeochem. Cycles, 20(14), doi:https://doi.org/10.1029/2005GB002456.

Fu, M., P. Sun, Z. Wang, Q. Wei, P. Qu, X. Zhang, and Y. Li (2018), Structure, characteristics and possible formation mechanisms of the subsurface chlorophyll maximum in the Yellow Sea

Cold Water Mass, Cont. Shelf Res., 165, 93-105, doi: https://doi.org/10.1016/j.csr.2018.07.007.

Fu, M., Z. Wang, Y. Li, R. Li, P. Sun, X. Wei, X. Lin, and J. Guo (2009), Phytoplankton biomass size structure and its regulation in the Southern Yellow Sea (China): Seasonal variability, Cont. Shelf Res., 29(18), 2178-2194, doi: https://doi.org/10.1016/j.csr.2009.08.010.

Garcia, H. E., R. A. Locarnini, T. P. Boyer, J. I. Antonov, O. K. Baranova, M. M. Zweng, J. R. Reagan, D. R. Johnson, A. V. Mishonov, and S. Levitus. (2013), World ocean atlas 2013. Volume 4, Dissolved inorganic nutrients (phosphate, nitrate, silicate), NOAA Atlas NESDIS 76, U.S. Government Printing Office, Washington, D.C., doi:http://doi.org/10.7289/V5J67DWD.

Gill, A. E., and A. J. Clarke (1974), Wind-induced upwelling, coastal currents and sea-level changes, Deep Sea Res., 21, 325–345, doi:https://doi.org/ 10.1016/0011-7471(74)90038-2.

Gong, Y., Z. Yu, Q. Yao, H. Chen, T. Mi, and J. Tan. (2015), Seasonal variation and sources of dissolved nutrients in the Yellow River, China, Int. J. Environ. Res. Public Health, 12(8), 9603-9622, doi:https://doi.org/10.3390/ijerph120809603.

Gruber, N., H. Frenzel, S. C. Doney, P. Marchesiello, J. C. McWilliams, J. R. Moisan, J. J. Oram, G.-K. Plattner, and K. D. Stolzenbach (2006), Eddy-resolving simulation of plankton ecosystem dynamics in the California Current System, Deep Sea Res. Part I, 53(9), 1483-1516, doi: https://doi.org/10.1016/j.dsr.2006.06.005.

Guo, X., X. H. Zhu, Q. S. Wu, and D. Huang (2012), The Kuroshio nutrient stream and its temporal variation in the East China Sea, J. Geophys. Res. Oceans, 117(C1), doi:https://doi.org/10.1029/2011JC007292.

Hong, J.-S., J.-H. Moon, J.-H. Lee, and I.-C. Pang (2016), Modeling the largest inflow of Changjiang freshwater into the Yellow Sea in 2012 with particle-tracking experiment, Ocean Sci. J., 51, 549-562, doi https://doi.org/10.1007/s12601-016-0057-1.

Hsueh, Y. (1988), Recent current observations in the eastern Yellow Sea, J. Geophys. Res., 93(C6), 6875–6884, doi:https://doi.org/10.1029/JC093iC06p06875.

Hsueh, Y., and I.-C. Pang (1989), Coastally trapped long waves in the Yellow Sea, J. Phys. Oceanogr., 19(5), 612–625, doi:http://dx.doi.org/10.1175/1520-0485(1989)019<0612:CTLWIT>2.0.CO;2.

Hsueh, Y., and R. D. Romea (1983), Wintertime winds and coastal sea-level fluctuations in the Northeast China Sea. Part I: observations, J. Phys. Oceanogr., 13, 2091–2106, doi:https://doi.org/10.1175/1520- 0485(1983)0132.0.CO;2.

Hsueh, Y., R. D. Romea, and P. W. DeWitt (1986), Wintertime winds and coastal sea level fluctuations in the Northeast China Sea. Part II: numerical model, J. Phys. Oceanogr., 16, 241–261, doi:https://doi.org/10.1175/1520- 0485(1986)0162.0.CO;2.

Hsueh, Y., and D. Yuan (1997), A numerical study of currents, heat advection, and sea-level fluctuations in the Yellow Sea in winter 1986, J. Phys. Oceanogr., 27(11), 2313–2326, doi:http://dx.doi.org/10.1175/1520-0485(1997)027<2313:ANSOCH>2.0.CO;2.

Huang, D., X. Fan, D. Xu, Y. Tong, and J. Su (2005), Westward shift of the Yellow Sea warm salty tongue, Geophys. Res. Lett., 32, L24613, https://doi.org/10.1029/2005GL024749.

Hur, H. B., G. A. Jacobs, and W. J. Teague (1999), Monthly variations of water masses in the Yellow and East China Seas, November 6, 1998, J. Oceanogr., 55(2), 171-184, doi: https://doi.org/10.1023/A:1007885828278.

Hyun, J.-H., and K.-H. Kim (2003), Bacterial abundance and production during the unique spring phytoplankton bloom in

the central Yellow Sea, Mar. Ecol. Prog. Ser., 252, 77–88, doi:https://doi.org/10.3354/meps252077.

Isobe, A. (2008), Recent advances in ocean-circulation research on the Yellow Sea and East China Sea shelves, J. Oceanogr., 64(4), 569–584, doi:https://doi.org/10.1007/s10872-008-0048-7.

Jacobs, G. A., R. H. Preller, S. K. Riedlinger, and W. J. Teague (1998), Coastal wave generation in the Bohai Bay and propagation along the Chinese coast, Geophys. Res. Lett., 25, 777–780, doi:https://doi.org/10.1029/97GL03636.

Jang, P.-G., T. S. Lee, J.-H. Kang, and K. Shin (2013), The influence of thermohaline fronts on chlorophyll a concentrations during spring and summer in the southeastern Yellow Sea, Acta Oceanol. Sin., 32(9), 82-90, doi: https://doi.org/10.1007/s13131-013-0355-8.

Jin, J., S. M. Liu, J. L. Ren, C. G. Liu, J. Zhang, G. L. Zhang, and D. J. Huang (2013), Nutrient dynamics and coupling with phytoplankton species composition during the spring blooms in the Yellow Sea, Deep Sea Res. Part II, 97, 16–32, doi:https://doi.org/10.1016/j.dsr2.2013.05.002.

Johnson, E. R. (1990), The low-frequency scattering of Kelvin waves by stepped topography, J. Fluid Mech., 215, 23–44,

doi:https://doi.org/10.1017/S0022112090002531.

Johnson, E. R. (1993), Low-frequency scattering of Kelvin waves by continuous topography, J. Fluid Mech., 248, 173–201, doi:https://doi.org/10.1017/S0022112093000734.-----

Kang, Y. H., S. Kim, J.-B. Lee, I. K. Chung, and S. R. Park (2014), Nitrogen biofiltration capacities and photosynthetic activity of *Pyropia yezoensis* Ueda (Bangiales, Rhodophyta): groundwork to validate its potential in integrated multi-trophic aquaculture (IMTA), J. Appl. Phycol., 26(2), 947-955, doi: https://doi.org/10.1007/s10811-013-0214-1.

Kim, C.-S., Y.-K. Cho, B.-J. Choi, K. T. Jung, and S. H. You (2013a), Improving a prediction system for oil spills in the Yellow Sea: Effect of tides on subtidal flow, Mar. Pollut. Bull., 68(1-2), 85-92, doi: https://doi.org/10.1016/j.marpolbul.2012.12.018.

Kim, C. H., and K. Kim (1983), Characteristics and origin of the cold water mass along the east coast of Korea, J. Oceanol. Soc. Korea, 18(1), 73-83.

Kim, J. K., C. Yarish, E. K. Hwang, M. Park, and Y. Kim (2017), Seaweed aquaculture: cultivation technologies, challenges and its ecosystem services, Algae, 32(1), 1-13, doi: https://doi.org/10.4490/algae.2017.32.3.3.

Kim, S.-K., K.-I. Chang, B. Kim, and Y.-K. Cho (2013b), Contribution of ocean current to the increase in N abundance in the Northwestern Pacific marginal seas, Geophys. Res. Lett., 40(1), 143-148, doi: https://doi.org/10.1029/2012GL054545.

Kwak, M.-T., G.-H. Seo, Y.-K. Cho, B.-G. Kim, S. H. You, and J.-W. Seo (2015), Long-term Comparison of satellite and in-situ sea surface temperatures around the Korean Peninsula, Ocean Sci. J., 50(1), 109–117, doi:https://doi.org/10.1007/s12601-015-0009-1.

Kwan, P. (1963), A preliminary study of the variation of the temperature and the characteristics of the circulation of the cold water mass of the Yellow Sea, Oceanol. et Limnol. Sin., 5(4), 255-284.

Kwon, H. K., G. Kim, J. Hwang, W. A. Lim, J. W. Park, and T.-H. Kim (2018), Significant and conservative long-range transport of dissolved organic nutrients in the Changjiang diluted water, Sci. Rep., 8(1), 12768, doi:https://doi.org/10.1038/s41598-018-31105-1.

Kwon, K.-M., B.-J. Choi, S.-H. Lee, Y.-K. Cho, and C.-J. Jang (2011), Coastal Current Along the Eastern Boundary of the Yellow Sea in Summer: Numerical Simulations, J. Korean Soc.

Oceanogr., 16(4), 155–168, doi:https://doi.org/10.7850/jkso.2011.16.4.155.

Large, W. G., J. C. McWilliams, and S. C. Doney (1994), Oceanic vertical mixing: a review and a model with a nonlocal boundary layer parameterization, Rev. Geophys., 32, 363–403, doi:https://doi.org/10.1029/94RG01872.

Lee, H. J. (2014), A Review of Sediment Dynamical Processes in the West Coast of Korea, Eastern Yellow Sea, Ocean Sci. J., 49(2), 85–95, doi:https://doi.org/10.1007/s12601-014-0010-0.

Li, Z., and D. Huang (2019), Sea surface height and current responses to synoptic winter wind in the Bohai, Yellow, and East China Seas: Two leading coastal trapped waves, J. Geophys. Res. Oceans, 124, doi:https://doi.org/10.1029/2018JC014120.

Li, H.-M., C.-S. Zhang, X.-R. Han, and X.-Y. Shi (2015), Changes in concentrations of oxygen, dissolved nitrogen, phosphate, and silicate in the southern Yellow Sea, 1980–2012: sources and seaward gradients, Estuar. Coast. Shelf Sci., 163, 44–55, doi:https://doi.org/10.1016/j.ecss.2014.12.013.

Lie, H.-J., C.-H. Cho, J.-H. Lee, S. Lee, Y. Tang, and E. Zou (2001), Does the Yellow Sea Warm Current really exist as a

persistent mean flow? J. Geophys. Res., 106(C10), 22199–22210, doi:https://doi.org/10.1029/2000JC000629.

Lie, H.-J., C.-H. Cho, S. Lee (2009), Tongue□shaped frontal structure and warm water intrusion in the southern Yellow Sea in winter, J. Geophys. Res., 114, C01003, doi:https://doi.org/10.1029/2007JC004683.

Lie, H.-J., C.-H. Cho, and S. Lee (2013), Frontal circulation and westward transversal current at the Yellow Sea entrance in winter, J. Geophys. Res., 118(8), 3851–3870, doi:https://doi.org/10.1002/jgrc.20280.

Lim, D.-I., M.-R. Kang, P.-G. Jang, S.-Y. Kim, H.-S. Jung, Y.-S. Kang, and Y.-S. Kang (2008), Water Quality Characteristics Along Midwestern Coastal Area of Korea, Ocean Polar Res., 30(4), 379-399, doi: https://doi.org/10.4217/OPR.2008.30.4.379.

Lim, D.-I., K.-C. Rho, P.-G. Jang, S.-M. Kang, H.-S. Jung, R.-H. Jung, and W.-C. Lee (2007), Temporal-spatial Variations of Water Quality in Gyeonggi Bay, West Coast of Korea, and Their Controlling Factor, Ocean Polar Res., 29(2), 135-153, doi:https://doi.org/10.4217/OPR.2007.29.2.135.

Lim, D.-I., H.-W. Choi, Y.-O. Kim, H.-S. Jung, and Y.-S. Kang (2011), Concentration Level and Grading of Water Quality

Components (COD, DIN, DIP, Chlorophyll-a) in Korean Coastal Waters: A Statistical Approach, Ocean and Polar Research, 33(1), 13-20, doi:https://doi.org/10.4217/OPR.2011.33.1.013.

Lin, X., and J. Yang (2011), An asymmetric upwind flow, Yellow Sea Warm Current: 2. Arrested topographic waves in response to the northwesterly wind, J. Geophys. Res., 116, C04027, doi:https://doi.org/10.1029/2010JC006514.

Lin, X., J. Yang, J. Guo, Z. Zhang, Y. Yin, X. Song, and X. Zhang (2011), An asymmetric upwind flow, Yellow Sea Warm Current: 1. New observations in the western Yellow Sea, J. Geophys. Res., 116, C04026, doi:https://doi.org/10.1029/2010JC006513.

Liu, C., Q. Sun, Q. Xing, Z. Liang, Y. Deng, and L. Zhu (2017), Spatio-temporal variability in sea surface temperatures for the Yellow Sea based on MODIS dataset, Ocean Sci. J., 52, 1-10, doi:https://doi.org/10.1007/s12601-017-0006-7.

Liu, X., K.-P. Chiang, S.-M. Liu, H. Wei, Y. Zhao, and B.-Q. Huang (2015a), Influence of the Yellow Sea Warm Current on phytoplankton community in the central Yellow Sea, Deep Sea Res. Part I, 106, 17-29, doi: https://doi.org/10.1016/j.dsr.2015.09.008.

Liu, X., B. Huang, Q. Huang, L. Wang, X. Ni, Q. Tang, S. Sun, H. Wei, S. Liu, C. Li, and J. Sun (2015b), Seasonal phytoplankton response to physical processes in the southern Yellow Sea, J. Sea Res., 95, 45–55, doi: https://doi.org/10.1016/j.seares.2014.10.017.

Locarnini, R. A., A. V. Mishonov, J. I. Antonov, T. P. Boyer, H. E. Garcia, O. K. Baranova, M. M. Zweng, C. R. Paver, J. R. Reagan, D. R. Johnson, M. Hamilton, D. Seidov, and S. Levitus (2013), World ocean atlas 2013. Volume 1, Temperature, NOAA Atlas NESDIS 73, U.S. Government Printing Office, Washington, D.C. doi:http://doi.org/10.7289/V55X26VD.

Lü, L.–G., G.–B. Yang, G. Wang, Z.–W. Liu, Y. Jiang, C. Yang, and C. Zhang (2015), Comparison of two cases of strong increase in the bottom temperature in the Yellow Sea in winter, Ocean Sci. J., 50(3), 557–566, doi:https://10.1007/s12601–015–0051–z.

Mask, A. C., J. J. O'Brien, R. Preller (1998), Wind□driven effects on the Yellow Sea Warm Current, J. Geophys. Res., 103, 30713–30729, doi:https://doi.org/10.1029/1998JC900007.

Moon, J.–H., N. Hirose, and J.–H. Yoon (2009), Comparison of wind and tidal contributions to seasonal circulation of the Yellow Sea, J. Geophys. Res., 114, C08016,

doi:https://10.1029/2009JC005314.

Morel, A., and J. F. Berthon (1989), Surface pigments, algal biomass profiles, and potential production of the euphotic layer: Relationships reinvestigated in view of remote□ sensing applications, Limnol. Oceanogr., 34(8), 1545–1562, doi: https://doi.org/10.4319/lo.1989.34.8.1545.

Naimie, C. E., C. A. Blain, R. Daniel, and D. R. Lynch (2001), Seasonal mean circulation in the Yellow Sea — a model-generated climatology, Cont. Shelf Res., 21(6–7), 667–695, doi: https://doi.org/10.1016/S0278-4343(00)00102-3.

[dataset] National Geophysical Data Center, ETOPO5 *Data announcement 88-MGG-02, Digital relief of the Surface of the Earth, National Oceanic and Atmospheric Administration,* 1988, accessed 5 February 2018, doi:https://www.ngdc.noaa.gov/mgg/global/etopo5.HTML.

NFRDI (2014), Study on the chlorosis phenomena in cultivated Phyropia. Annual report of NFRDI.

Pang, I.-C. (1991), Coastally trapped waves over a double shelf topography (I): Free waves with exponential topography, Korean J. Fish. Aquat. Sci., 24(6), 428–436.

Park, C. K. (1978), Chemical oceanographic aspect of the cole water mass in offshore of the east coast of Korea. Korean J.

Fish. Aquat. Sci., 11(2), 49-54.

Park, M., S. K. Shin, Y. H. Do, C. Yarish, and J. K. Kim (2018), Application of open water integrated multi-trophic aquaculture to intensive monoculture: A review of the current status and challenges in Korea, Aquaculture, 497, 174-183, doi: https://doi.org/10.1016/j.aquaculture.2018.07.051.

Park, R. S., Y.-K. Cho, B.-J. Choi, C. H. Song (2011), Implications of sea surface temperature deviations in the prediction of wind and precipitable water over the Yellow Sea, J. Geophys. Res., 116, D17106, doi:https://doi.org/ 10.1029/2011JD016191.

Park, S., P. C. Chu, and J.-H. Lee (2011), Interannual-to-interdecadal variability of the Yellow Sea Cold Water Mass in 1967–2008: Characteristics and seasonal forcings. 87(3-4), 177-193, doi:https://doi.org/10.1016/j.jmarsys.2011.03.012,

Park, Y.-H. (1986), A simple theoretical model for the upwind flow in the southern Yellow Sea, J. Oceanol. Soc. Korea., 21, 203–210.

Power, S. B., J. H. Middleton, R. H. J. Grimshaw (1989), Frictionally modified continental shelf waves and the subinertial response to wind and deep-ocean forcing, J. Phys. Oceanogr., 19,

1486–1506, doi:https://doi.org/10.1175/1520-0485(1989)019<1486:FMCSWA>2.0.CO;2.

Qu, L., X. Lin, R. D. Hetland, J. Guo (2018), The asymmetric continental shelf wave in response to the synoptic wind burst in a semienclosed double-shelf basin, J. Geophys. Res. Oceans, 123, doi:https://doi.org/10.1002/2017JC013025.

Shchepetkin, A. F., and J. C. McWilliams (2005), The regional oceanic modeling system (ROMS): A split-explicit, free-surface, topography-following-coordinate oceanic model. Ocean Model. 9, 347–404, doi:https://doi.org/10.1016/j.ocemod.2004.08.002.

Seo, G.-H., Y.-K. Cho, B.-J. Choi, K.-Y. Kim, B. Kim, and Y.-J. Tak (2014), Climate change projection in the Northwest Pacific marginal seas through dynamic downscaling. 119(6), 3497-3516, doi:https://doi.org/10.1002/2013JC009646.

Shim, J., J. R. Hwang, S. Y. Lee, and J. Kwon (2014), Variations in Nutrients & CO2 Uptake Rates of Porphyra yezoensis Ueda and a Simple Evaluation of in situ N & C Demand Rates at Aquaculture Farms in South Korea, Korean J. Environ. Biol.. 32(4), 297-305,doi:https://doi.org/10.11626/KJEB.2014.32.4.297.

Song, G., S. Liu, Z. Zhu, W. Zhai, C. Zhu, and J. Zhang (2016),

Sediment oxygen consumption and benthic organic carbon mineralization on the continental shelves of the East China Sea and the Yellow Sea, Deep Sea Res. Part II, 124, 53–63, doi:https://doi.org/10.1016/j.dsr2.2015.04.012.

Spall, M. A., and J. Pedlosky (2005), Reflection and transmission of equatorial Rossby waves, J. Phys. Oceanogr., 35, 363–373, doi:https://doi.org/10.1175/JPO-2691.1.

Tak, Y.-J., Y.-K. Cho, G.-H. Seo, B.-J. Choi (2016), Evolution of wind□driven flows in the Yellow Sea during winter, J. Geophys. Res. Oceans, 121, 1970–1983, doi:https://doi.org/10.1002/2016JC011622.

Takahashi, S., Y. Isoda, and T. Yanagi (1995), A numerical study on the formation and variation of a clockwise-circulation during winter in the Yellow Sea, J. Oceanogr., 51(1), 83–98, doi:https://doi.org/10.1007/BF02235938.

Tan, S.-C., and G.-Y. Shi (2012), The relationship between satellite-derived primary production and vertical mixing and atmospheric inputs in the Yellow Sea cold water mass, Cont. Shelf Res., 48, 138-145, doi:https://doi.org/10.1016/j.csr.2012.07.015.

Teague, W., and G. Jacobs (2000), Current observations on the development of the Yellow Sea Warm Current, J. Geophys.

Res., 105(C2), 3401–3411, doi:https://doi.org/10.1029/1999JC900301.

Thomson, W. (1880), 1. On Gravitational Oscillations of Rotating Water, Proc. Roy. Soc. Edin., 10, 92–100, doi:https://doi.org/10.1017/S0370164600043467.

Uda, M. (1934), Hydrographical research on the normal monthly conditions in the Japan Sea, the Yellow Sea, and the Okhotsk Sea (in Japanese), J. Imp. Fish. Exp. Stn., 5, 191–236.

Uitz, J., H. Claustre, A. Morel, and S. B. Hooker (2006), Vertical distribution of phytoplankton communities in open ocean: An assessment based on surface chlorophyll, J. Geophys. Res. Oceans, 111, C08005, doi:https://doi.org/10.1029/2005JC003207.

Vörösmarty, C., B. Fekete, and B. Tucker (1996), River discharge database version 1.0 (RivDIS v1.0), Vol. 0–6. A contribution to IHP–V theme 1.

Wang, B.–d., X.–l. Wang, R. Zhan (2003), Nutrient conditions in the Yellow Sea and the East China Sea, Estuar. Coast. Shelf Sci., 58(1), 127–136, doi: https://doi.org/10.1016/S0272–7714(03)00067–2.

Wang, F., C. Liu, and Q. Meng (2012), Effect of the Yellow Sea Warm Current fronts on the westward shift of the Yellow Sea

warm tongue in winter, Cont. Shelf Res., 45, 98–107, doi:https://doi.org/10.1016/j.csr.2012.06.005.

Wang, K., J. Chen, H. Jin, F. Chen, H. Li, S. Gao, and Y. Lu (2011), The four seasons nutrients distribution in Changjiang River Estuary and its adjacent East China Sea, J. Mar. Sci., 29(3), 18-35.

Wang, Q., X. Guo, and H. Takeoka (2008), Seasonal variations of the Yellow River plume in the Bohai Sea: a model study, J. Geophys. Res., 113, C08046, doi:https:/doi.org/10.1029/2007JC004555.

Wei, Q.-S., Z.-G. Yu, B.-D. Wang, M.-Z. Fu, C.-S. Xia, L. Liu, R.-F. Ge, H.-W. Wang, and R. Zhan (2016), Coupling of the spatial–temporal distributions of nutrients and physical conditions in the southern Yellow Sea, J. Mar. Syst., 156, 30-45, doi:https://doi.org/10.1016/j.jmarsys.2015.12.001.

Wilkin, J. L., and D. C. Chapman (1990), Scattering of coastal-trapped waves by irregularities in coastline and topography, J. Phys. Oceanogr., 20, 396–421, doi:https://doi.org/10.1175/1520-0485(1990)020<0396:SOCTWB>2.0.CO;2.

Winant, C. D. (2004), Three-dimensional wind-driven flow in an elongated, rotating basin, J. Phys. Oceanogr., 34(2), 462–476,

doi:http://dx.doi.org/10.1175/1520-0485(2004)034<0462:TWFIAE>2.0.CO;2.

Xie, S.-P., J. Hafner, Y. Tanimoto, W. T. Liu, H. Tokinaga, and H. Xu (2002), Bathymetric effect on the winter sea surface temperature and climate of the Yellow and East China Seas, Geophys. Res. Lett., 29, 2228, doi:https://doi.org/10.1029/2002GL015884.

Xing, C., and D. Huang (2010), Numerical investigation on the mechanism of the westward shifting of the Huanghai Warm Current, Acta Oceanol. Sin., 32, 1–10.

Xu, D., Y. Yuan, and Y. Liu (2003), The baroclinic circulation structure of Yellow Sea Cold Water Mass, Sci. China Ser. D-Earth Sci., 46(2), 117-126, doi:https://doi.org/10.1360/03yd9011.

Xu, L. L., D. X. Wu, X. P. Lin, and C. Ma (2009), The study of the Yellow Sea Warm Current and its seasonal variability, J. Hydrodynam., 21, 159–165, doi:https://doi.org/10.1016/S1001-6058(08) 60133-X.

Xuan, J.-L., F. Zhou, D.-J. Huang, H. Wei, C.-G. Liu, and C.-X. Xing (2011), Physical processes and their role on the spatial and temporal variability of the spring phytoplankton bloom in the central Yellow Sea. Acta Ecol. Sin., 31(1), 61-70,

doi:https://doi.org/10.1016/j.chnaes.2010.11.011.

Yanagi, T., and S. Takahashi (1993), Seasonal variation of circulations in the East China Sea and the Yellow Sea, J. Oceanogr., 49, 503–520, doi:https://doi.org/10.1007/BF02237458.

Yang, H.-W., Y.-K. Cho, G.-H. Seo, S. H. You, and J.-W. Seo (2014), Interannual variation of the southern limit in the Yellow Sea Bottom Cold Water and its causes, 139, 119-127, doi:https://doi.org/10.1016/j.jmarsys.2014.05.007.

Yu, F., Z. Zhang, X. Diao, J. Guo (2010), Observational evidence of the yellow sea warm current, Chin. J. Ocean. Limnol., 28, 667–683, doi:https://doi.org/10.1007/s00343-010-0006-2.

Yuan, D., and Y. Hsueh (2010), Dynamics of the cross-shelf circulation in the Yellow and East China Seas in winter, Deep Sea Res. Part II, 57, 1745–1761, doi:https://doi.org/10.1016/j.dsr2.2010.04.002.

Zhang, J., S. M. Liu, J. L. Ren, Y. Wu, and G. L. Zhang (2007), Nutrient gradients from the eutrophic Changjiang (Yangtze River) Estuary to the oligotrophic Kuroshio waters and re-evaluation of budgets for the East China Sea Shelf, Prog. Oceanogr., 74(4), 449-478, doi:https://doi.org/10.1016/j.pocean.2007.04.019.

Zhou, F., F. Chai, D. Huang, H. Xue, J. Chen, P. Xiu, J. Xuan, J. Li, D. Zeng, X. Ni, and K. Wang (2017), Investigation of hypoxia off the Changjiang Estuary using a coupled model of ROMS-CoSiNE, Prog. Oceanogr., 159, 237-254, doi:https://doi.org/10.1016/j.pocean.2017.10.008.

Zhou, F., J. Xuan, D. Huang, C. Liu, and J. Sun (2013), The timing and the magnitude of spring phytoplankton blooms and their relationship with physical forcing in the central Yellow Sea in 2009. Deep Sea Res. Part II, 97, 4-15, doi:https://doi.org/10.1016/j.dsr2.2013.05.001.

Zhu, J., J. Shi, X. Guo, H. Gao, and X. Yao (2018), Air-sea heat flux control on the Yellow Sea Cold Water Mass intensity and implications for its prediction, Cont. Shelf Res., 152, 14-26, doi:https://doi.org/10.1016/j.csr.2017.10.006.

Zweng, M. M., J. R. Reagan, J. I. Antonov, R. A. Locarnini, A. V. Mishonov, T. P. Boyer, H. E. Garcia, O. K. Baranova, D. R. Johnson, D. Seidov. M. M. Biddle, S. Levitus (2013), World ocean atlas 2013. Volume 2, Salinity, NOAA Atlas NESDIS 74, U.S. Government Printing Office, Washington, D.C, doi:http://doi.org/10.7289/V5251G4D.

Abstract (in Korean)

황해는 한반도와 중국 사이에 존재하는 반폐쇄성 해역이며 해역 중앙에는 수심 90 m 이상의 깊은 골이 존재한다. 겨울철 황해에 나타나는 주요 해류는, 북서계절풍으로 인해 중국 및 한국 연안에는 남향하는 흐름이 존재하며 깊은 골에는 바람의 반대 방향으로 북향하는 황해 난류가 나타난다. 관측을 통해 황해 난류의 경로는 황해 내부 깊은 골의 서쪽으로 치우쳐져 있고 바람이 분 뒤 하루나 이틀 뒤 강해진다고 보고되었으나, 형성과정에 대해선 자세히 보고된 바가 없다. 본 연구의 모델 수행 결과, 겨울철 황해에는 평균적으로 시계방향의 순환이 발생하였으며, 시간지연 상관관계 분석 결과, 황해 난류는 바람이 분 하루 뒤 깊은 골에 출현하였으며 이틀 뒤 골의 서쪽으로 편향되는 것으로 나타났다.

선행연구는 황해 난류의 서쪽 편향 현상이 대륙붕파에 의해 발생 할 수 있다고 주장하고 있다. 지형을 간소화한 모델을 통해 황해 난류의 서쪽 편향 현상과 편향 현상의 주 요인인 대륙붕파의 역할 및 형성 기작에 대해 연구하였다. 본 연구 결과, 황해 난류의 서쪽 편향 현상은 대륙붕파의 전파와 함께 발생하였으며 편향 현상의 전파 속도는 2.99 m/s 로 대륙붕파의 1번 모드 전파 속도와 일치하였다. 대륙붕파는 바람에 의해 경사가 있는 지역에서 발생할 수 있지만, 편향 현상을 주도하는 대륙붕파는 겨울철 북풍으로 인해 발생하는 캘빈 파가 황해의 북쪽 사면에서 산란 되면서 발생하는 것으로 나타났다.

황해 난류는 외부의 수괴를 황해 내부로 유입시키기 때문에 황해

생태계에도 중요한 역할을 한다. 물리-생지화학 접합 모델을 통해 황해 난류로 인한 질산염 유입량을 연구하였으며, 외부 유입원 및 질화 작용을 통한 생물학적인 공급량을 정량화 하였다. 관측 자료를 통해 황해 주변에 질산염 농도가 높은 수괴를 살펴본 결과, 황해 내부의 황해저층냉수와 쿠로시오 해류가 기원인 대한해협 중층수의 질산염 농도가 높았다. 민감도 실험을 통해 양자강, 쿠로시오 해류, 대만 난류, 황해 내부 강들의 효과, 그리고 질화 작용의 기여도를 각각 산정하였다. 황해 질산염의 51%가 양자강 기원이었으며, 쿠로시오 해류 그리고 황해 내부 강들이 전체 질산염의 약 25%씩 차지하고 있었고 대만난류로부터 기인한 질산염은 전체의 5% 정도로 적은 양이 유입되는 것을 알 수 있었다. 질화 작용을 통한 유입은 1% 아래로 낮게 나타났으며, 이는 황해에 존재하는 질산염은 생물학적인 공급보다 해류들로 인해 외부로부터 유입되는 것임을 의미한다. 각 기원의 공간적인 기여도를 살펴본 결과, 양자강 기원 질산염은 황해 중앙부 및 서쪽에서 기여도가 높게 나타났으며, 쿠로시오 해류 기원 질산염은 황해 중앙부에 존재하는 질산염에 부차적인 기여를 하는 것으로 나타났다. 황해 내부 강물에 의한 질산염 유입은 황해 동쪽 연안과 산둥반도 주변 연안에 국한되어 영향을 주었다. 황해 난류로 인해 유입되는 질산염 양은 0.137 Tg N 로 겨울철 황해 내부 평균 질산염 질량의 약 20% 정도가 황해 난류로 인해 유입되는 것으로 나타났다. 황해 난류로 인해 유입되는 질산염 중 양자강, 쿠로시오 해류, 대만난류 기원을 정량화한 결과, 각각 64%, 29%, 그리고 10%를 차지하고 있음을 알 수 있었다.